Deliverable 8.8:
Thermo-mechanical-chemical properties of unirradiated and irradiated samples of spent nuclear fuel rod segments and cladding

Work Package 8 (SFC)

This project has received funding from the European Union's Horizon 2020 research and innovation programme under grant agreement N°847593.

http://www.ejp-eurad.eu/

Document information

Project Acronym	**EURAD**
Project Title	**European Joint Programme on Radioactive Waste Management**
Project Type	**European Joint Programme (EJP)**
EC grant agreement No.	**847593**
Project starting / end date	**1 June 2019 – 30 May 2024**
Work Package No.	**8**
Work Package Title	**Spent Fuel Characterisation and Evolution Until Disposal**
Work Package Acronym	**SFC**
Deliverable No.	**8.8**
Deliverable Title	**Thermo-mechanical-chemical properties of unirradiated and irradiated samples of spent nuclear fuel rod segments and cladding**
Lead Beneficiary	**KIT**
Contractual Delivery Date	**31 May 2024**
Actual Delivery Date	**29 August 2024**
Type	**Report**
Dissemination level	**PU**
Authors	**Uwe Zencker (BAM), Carlos Aguado (CIEMAT), Asko Arkoma (VTT), Johannes Bertsch (PSI), Miguel Cristóbal Beneyto (UPM), Francisco Feria Marquez (CIEMAT), Luis Enrique Herranz (CIEMAT), Ivan Ivanov (TUS), Márton Király (REN CER), Ramil Nasyrow (JRC-KA), Dimitrios Papaioannou (JRC-KA), Jesus Ruiz-Hervias (UPM), Efstathios Vlassopoulos (Nagra)**

To be cited as:

Zencker, U. et al. (2024): Thermo-mechanical-chemical properties of unirradiated and irradiated samples of spent nuclear fuel rod segments and cladding. Final version as of 29/08/2024 of deliverable D8.8 of the HORIZON 2020 project EURAD. EC Grant agreement no: 847593.

Disclaimer

Acknowledgement

This document is a deliverable of the European Joint Programme on Radioactive Waste Management (EURAD). EURAD has received funding from the European Union's Horizon 2020 research and innovation programme under grant agreement No 847593.

Status of deliverable		
	By	Date
Delivered (Lead Beneficiary)	Uwe Zencker (BAM)	29/07/2024
Verified (WP Leader)	SKB	20/08/2024
Approved (PMO)	Paul Carbol (JRC)	21/08/2024
Submitted to EC (Coordinator)	Andra	30/08/2024

Executive Summary

The report addresses the experimental characterisation, thermo-mechanical modelling and performance of unirradiated and irradiated samples of spent nuclear fuel rod segments and cladding. Hydrogen is relocated in nuclear fuel claddings by diffusion along temperature, stress, and concentration gradients, and towards a liner if existent. The precipitation of hydrides during cool-down at the beginning of the storage is influenced by mechanical stress. A strong accumulation of hydrides and a disadvantageous hydride alignment in relation to the stress state can affect the mechanical properties and compromise the fuel cladding integrity. Neutron radiography is used to determine spatially resolved hydrogen and hydride distributions in claddings. A liner in duplex claddings attracts hydrogen, which will then no longer be available to form detrimental hydrides in the bulk part of the cladding. Individual three-point bending and gravitational impact tests on filled pressurised spent nuclear fuel rod segments were conducted in hot-cell facilities. The material behaviour under three-point bending in the presence of hydrides and at different temperatures was systematically investigated in quasi-static laboratory tests on unirradiated rod segments with and without surrogate pellets until rupture. Ring compression tests were carried out on irradiated and unirradiated samples at different temperatures and both with and without radial hydrides. With radial hydrides, brittle failure is possible even at low deformation and simultaneously low temperature. Crack initiation will occur on the radial hydride with the highest fracture mechanics load, which depends on the hydride size in the regions with the highest hoop stresses. Due to the high hydrogen content used in creep tests conducted, precipitation hardening of the hydrides in the zirconium alloy significantly reduces the creep rate, as it strengthens the material and inhibits the dislocation sliding. The use of finite element analyses on mechanical tests to determine the cladding properties using a numerical optimisation method based on a large number of automatically generated sensitivity calculations is demonstrated. The brittle fracture of cladding samples with radial hydrides in the ring compression test can be described with a cohesive zone model if the cohesive parameters are selected appropriately and the hydride morphology is specified. Progress was made in the verification, validation and enhancement of spent fuel performance codes by the compilation of a representative validation database (related to rod internal pressure, fission gas release, rod void volume, and in-clad hydrogen distribution), the enhancement of CIEMAT's FRAPCON-xt code for rod internal pressure prediction at high burnup, the enhancement of CIEMAT's in-clad hydrogen performance subroutine HYDCLAD with more phenomenological modelling, the extension of INL's BISON code with a cladding creep law for dry storage, and a benchmark with FRAPCON-xt and BISON simulating in-reactor and dry storage scenarios.

Keywords

Spent Nuclear Fuel; Cladding; Experimental Characterisation; Modelling; Fuel Performance Code

Table of Content

List of Figures

List of Tables

Glossary

BAM	Bundesanstalt für Materialforschung und -prüfung
BU	Burnup
BWR	Boiling water reactor
CIEMAT	Centro de Investigaciones Energéticas, Medioambientales y Tecnológicas
CZM	Cohesive zone model
DHC	Delayed hydride cracking
ECD	Equivalent circle diameter
EDS	Energy dispersive X-ray spectroscopy
EMPA	Swiss Federal Laboratories for Materials Science and Technology
EOL	End of life
FEA	Finite element analysis
FEM	Finite element model
FGR	Fission gas release
HUN-REN CER	Hungarian Centre for Energy Research
INL	Idaho National Laboratory
JRC-KA	European Joint Research Centre Karlsruhe
JRC-PETTEN	European Joint Research Centre Petten
KKG	Gösgen Nuclear Power Plant
MOOSE	Multi-physics Object-Oriented Simulation Environment
Nagra	Nationale Genossenschaft für die Lagerung radioaktiver Abfälle
PGAA	Prompt-gamma activation analysis
PIE	Post-irradiation examination
PNNL	Pacific Northwest National Laboratory
PSI	Paul Scherrer Institute
PT	Hydride precipitation treatment
PWR	Pressurised water reactor
RCT	Ring compression test
RHT	Radial hydride treatment
RIA	Reactivity-initiated accident
RIP	Rod internal pressure
SEM	Scanning electron microscopy
SNF	Spent nuclear fuel
TPB	Three-point bending
VTT	Technical Research Centre of Finland Ltd
UPM	Universidad Polytécnica de Madrid, E.T.S.I. Caminos

1. Introduction

The Work Package 8 of the EURAD project addressed the characterisation of spent nuclear fuel (SNF). An important objective was to establish validated procedures to reliably determine the nuclide content in SNF, including realistic uncertainties, by developing characterisation techniques and uncertainty quantification. Another essential objective was to analyse the performance of SNF during prolonged storage, transport and emplacement in a deep geological repository by enhancing the capabilities for safety analyses of relevant operations. The results of the spent fuel characterisation will contribute to the understanding and description of the thermal, mechanical and radiochemical behaviour and ageing effects under normal and handling conditions as well as under postulated accident conditions between discharge from the reactor and final disposal. For this purpose, relevant or typical load or boundary cases were analysed. The work carried out thus contributes to the operational safety for SNF handling at storage facilities and transport after storage. The results shall also contribute to education, training and building of competence in this subject.

Task 3 of Work Package 8 focused on the behaviour and evolution of spent nuclear fuel and cladding properties after discharge. The methods applied and results obtained in Subtask 3.1 for thermo-mechanical behaviour of fuel and claddings are to be reported in this deliverable. The activities can be grouped into three topics: experimental characterisation, modelling, and documentation.

For the experimental characterisation of the thermo-mechanical properties of SNF rods and in particular of their cladding tubes, the bending behaviour and pressure behaviour under static and dynamic load at different temperatures as well as the creep behaviour are of interest. These load cases result from the analysis of the storage, handling or postulated accident conditions. A distinction is made as to whether the cladding tube contains pellets or is empty. The material properties can be determined on empty cladding tubes without any other interfering influences. The material behaviour of the cladding tubes depends, among other factors, on the hydrogen present (from reactor operation or through intentional loading) and the precipitated hydrides. With regard to hydrides, their alignment to the direction of prevailing stresses is of decisive importance, as the material behaviour can change qualitatively from ductile to brittle due to the stress state. In order to clarify the material behaviour, accompanying investigations on the material microstructure (by scanning electron microscopy), on the hydride distributions and cracks (by optical microscopy), and on the distribution of dissolved hydrogen (by neutron radiography) are therefore essential. However, filled cladding tubes are the most relevant in practice. With knowledge of the previously determined material states, the component properties of a cladding tube with pellets can then be clarified, including the question of how much fuel is released during a cladding tube rupture.

The numerical modelling of the material behaviour is essential for the study of failure modes and the derivation of thermo-mechanical properties of fuel rods and in particular of their cladding tubes. Knowledge of the stress state in a structure, in combination with the properties of the material such as the hydride morphology, enables more detailed insights into the cause of a potential cladding tube failure. This applies to individual load scenarios, such as in the three-point bending test or ring compression test, as well as to complex loads on an entire fuel assembly, possibly under the conditions of dry storage in a cask or during transport to a final repository after storage. The entire life cycle of a fuel rod is modelled by spent fuel performance codes that take into account the variety of material effects and load scenarios. Findings from the modelling of relatively simple scenarios and experimental characterisation can help to extend and validate the model approaches used. Knowledge of the burnup history is important for modelling the fuel rod behaviour. This data must therefore be documented accordingly.

2. Failure Behaviour of Fuel Rods

The most important thermo-mechanical failure mechanisms of fuel rod claddings are creep, hydrogen-related mechanisms and effects (e.g., hydride embrittlement, delayed hydride cracking), stress corrosion cracking and diffusion-controlled cavity growth [1]. The investigations carried out in this work package focus on hydrogen-based failure mechanisms and creep. Both effects are briefly introduced in the following sections.

2.1 Hydrogen Content

Zirconium alloys generally exhibit a very good corrosion resistance at high temperatures. Nevertheless, there is a slow and uniform corrosion of the cladding tube material on the outside of zirconium-based fuel rod cladding tubes due to the reaction with the water in the reactor pressure vessel. A layer of mostly monoclinic zirconium dioxide (the corrosion layer) is formed according to the reaction [2]:

$$Zr + 2\,H_2O \rightarrow ZrO_2 + 2\,H_2 \quad (1)$$

Because this oxide layer does not limit further corrosion, it can reach a thickness of up to 100 µm by the time the fuel rod is discharged from the reactor pressure vessel. For a typical pressurised water reactor fuel assembly with 17 x 17 fuel rods, this would correspond to around one sixth of the wall thickness of the cladding [3].

A small proportion of the hydrogen produced during corrosion penetrates into the cladding. Although there are other sources of hydrogen (e.g., from water chemistry), only the ingress of hydrogen from corrosion into the cladding tube material was observed [3]. The amount of hydrogen absorbed in relation to the total hydrogen produced is in the range of 10 % for conventional zirconium-based cladding materials for boiling water or pressurised water reactors, which corresponds to less than about 500 wppm (weight parts per million) and depends primarily on the physical parameters of the reactor operation and the composition of the alloy [1]. Hydrogen absorption during reactor operation is not constant, but increases as corrosion progresses [4].

As with most materials, the solubility of hydrogen in zirconium alloys in the unirradiated state increases with increasing temperature [5]. The irradiation itself does not appear to have a significant influence on this temperature dependence. The solubility of hydrogen in zirconium-based alloys is significantly less than 1 wppm at room temperature. At 400 °C the solubility is in the range of 170 to 300 wppm. Fuel rod claddings typically have hydrogen concentrations of 15 to 20 wppm at the onset of operation. As a result of corrosion during operation, values of 300 wppm and more (depending on burn-up) can be achieved [1]. As soon as the hydrogen solubility limit is exceeded, zirconium hydride precipitates in the form of platelets in the microstructure [6].

The hydrogen is very mobile in the fuel rod cladding and is sensitive to concentration, stress and temperature gradients, which leads to changes in the atomic hydrogen distribution and to local concentration maxima of the hydride precipitations in the cladding tube. The redistribution processes cause it to drift into areas with high hydrostatic tensile stress. If a crack-like defect is present, the hydrogen preferentially accumulates in the area of stress concentration around the crack tip [7]. If there is a temperature gradient, the hydrogen diffuses towards the lower temperature. This can lead to a locally high concentration of hydrogen on the outside of the cladding tube in the form of hydride rims [8] or hydride blisters [9]. Hydride rims are layers of uniform depth that can reach a thickness of 50 to 60 µm and a large extent in the cladding tube. Hydride blisters, on the other hand, have an elliptical shape, tend to be found on the outer cladding tube surface and are usually up to half the thickness of the cladding tube. The hydrogen concentration is lower in hydride rims than in blisters. Individual hydrides can still be distinguished inside a hydride rim using high resolution scanning electron microscopy, whereas this is not possible in blisters [10].

2.2 Zirconium Hydrides

As soon as the hydrogen solubility in the zirconium alloy is reached, hydride precipitations can occur within the zirconium matrix, which are often referred to as hydride platelets. Their thickness-to-length ratio is usually between 0.02 and 0.1 [1]. The hydride structure can be analysed using metallographic micrographs. The sample must be pre-treated by chemical etching to make the hydride particles visible. It should be noted here that microscopic examination of the micrograph sample at low magnification actually shows clusters of smaller hydride particles that form structures on the mesoscale (µm-nm-scale). It is these mesoscale hydride clusters that influence the mechanical properties of the cladding, as they generally increase strength and reduce ductility, but also lead to hydride embrittlement and delayed hydride cracking.

The stable phase in the phase diagram of zirconium alloys at low temperatures is the face-centred cubic (fcc) delta phase, although other phases, such as the gamma phase, are occasionally observed, especially at the beginning of the precipitation process [11]. The precipitation of hydrides is influenced by many factors, such as the presence of grain boundaries, internal stresses and the alloying elements. The precipitation of microscopically small hydride plates initially leads to a distortion of the microstructure. The internal stresses caused by these distortions favour the precipitation of further hydride particles in the immediate vicinity. Their combination then leads to the mesoscale hydride platelets, which consist of a large number of much smaller microscopic hydrides arranged like a stack of cards [3].

Hydrides typically precipitate along certain crystallographic planes. The texture of zirconium alloys has a strong influence on the orientation of the precipitated hydrides. Commercial cladding tubes are manufactured with a specific texture (i.e., a preferred orientation of the grains), which leads to hydrides being predominantly orientated in the circumferential direction [12] (see Figure 1(a)). Hydride platelets, aligned perpendicular to the direction of stress, cause an increase in strength and a reduction in ductility of the material, while hydride platelets aligned parallel to the direction of stress have hardly any effect.

a) 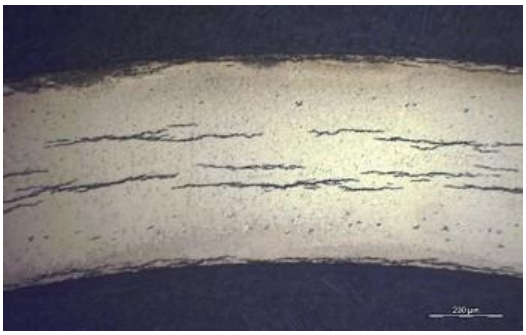 *b)* 

Figure 1 – Hydride structure after precipitation (a) and reorientation (b)

Under certain thermo-mechanical conditions, the hydrides in a fuel rod cladding tube can reorient (see Figure 1(b)). Vacuum drying of the cask interior after loading with fuel assemblies leads to a significant increase in the temperature of the fuel rods. The maximum temperature recommended by the US Nuclear Regulatory Commission (NRC) is 400 °C [13]. For interim storage in Germany, this maximum temperature is limited to 370 °C by the competent authority BASE. As the solubility of hydrogen in zirconium at this temperature is around 200 wppm, existing hydrides can at least partially dissolve again [3]. The internal pressure of the fuel rods also rises with the temperature, starting from around 4 MPa when unloading from the reactor pressure vessel and without external counter pressure as in reactor operation. After vacuum drying, the temperature slowly decreases again under storage conditions, which also reduces the internal pressure of the fuel rods. During this cooling phase, the dissolved hydrogen can re-precipitate in the form of realigned hydride platelets whose normal vectors run parallel to the

direction of stress. In case of hoop stress, caused by the internal fuel rod pressure, the hydride platelets are newly precipitated perpendicular to the circumferential direction and are referred to as radial hydrides. The effect of hydride orientation was first described in the 1960s for the zirconium alloy Zircaloy-2 [14, 15] and then intensively investigated, particularly on cladding tubes made of Zircaloy-4 [16, 17, 18], but also of ZIRLO® and other zirconium alloys [19, 20, 21]. The tensile stress required for complete hydride reorientation was determined by Desquines et al. [22]. A multiaxial stress state reduces the critical stress required to reorient the hydrides [23].

The presence of hydrides promotes the formation of cracks under unfavourable mechanical stress. In particular, existing radial hydrides can lead to embrittlement of the cladding tube under hoop stress. The embrittlement caused by radial hydrides influences the ductility, tensile strength and fracture mechanical properties of the material. The effects on the material properties depend on the size, location, quantity and distribution of the radial hydrides [17, 20, 21].

The solubility limit for the dissolution of hydrides differs from that for the precipitation of hydrides. It is assumed that during cooling, due to the energy released for hydride precipitation, this only starts at a lower temperature than that required for hydride dissolution during heating [24].

Diffusion of hydrogen atoms in the vicinity of a crack tip can also lead to delayed hydride crack formation. This damage process requires a longer period of time, the presence of a crack-like defect, the formation of a hydride zone at the crack tip and the growth of the crack until the potential fracture of the brittle hydride zone. The reason for the diffusion of the hydrogen atoms is the high tensile stress in the vicinity of the crack tip. As soon as the hydrogen concentration exceeds the solubility limit, hydrides begin to form and grow. If the hydride zone reaches a critical size under a sufficient tensile stress, this zone can break and eventually lead to the failure of the cladding tube. The mechanism of delayed hydride crack formation is only triggered if the stress intensity at the crack tip is above a threshold value of about 1.5 MPa√m [25]. It is currently assumed that the stress intensities under the conditions of dry interim storage will probably be lower than this critical stress intensity [1].

2.3 Hydride Embrittlement

The precipitation of hydrides has a significant influence on the embrittlement and possible failure of cladding tubes made of zirconium alloys. Uniformly distributed circumferential hydrides under reactor operating conditions only influence the ductility of the material. After unloading from the reactor pressure vessel and in particular in connection with the initial phase of the subsequent dry interim storage in casks, hydride reorientation can occur with the result of radial hydride precipitation, so that at lower temperatures the applied loads and the orientation of the hydrides determine the mechanical behaviour. Radial hydrides can lead to the initiation of long cracks and failure of the cladding tube under tensile hoop stress. The material then behaves brittle and the initiation and propagation of cracks depends on the fracture mechanical properties of the matrix material and the quantity and configuration of the embedded hydrides. If, in contrast, the radial hydrides are missing, ductile damage to the material with the formation, growth and coalescence of micro-voids can occur at existing circumferential hydrides [26].

Experimental investigations on zirconium alloys with hydride precipitations show that the hydride distribution has a significant influence on the global deformation behaviour of the cladding tube. Existing hydride rims or hydride blisters can change the failure behaviour from ductile to brittle by initiating cracks. As the thickness of a hydride rim or blister increases, the elongation at fracture decreases. As the load increases, the hydrides initially crack and ultimately cause the non-cracked matrix material to fail due to localised plastic deformation and ductile crack growth [27]. The susceptibility to brittle fracture is particularly pronounced with thick hydride rims or if the ligament (i.e., the area in front of a crack tip) has a low fracture toughness (e.g., in presence of radial hydrides) [28].

The presence of radial hydrides supports both crack initiation and crack growth, provided the temperature is low enough for cracks to form. The radial hydrides cause a steep transition from ductile to brittle failure with decreasing temperature [18]. This behaviour is illustrated by the curve of the fracture energy as a function of temperature (see Figure 2). In case of ductile failure, the fracture energy is high

(or in the upper shelf), whereas in case of brittle failure it is low (or in the lower shelf). For comparable hydrogen concentrations, the ductile to brittle transition temperature (DBTT) is significantly higher in the presence of radial hydrides compared to the presence of only circumferential hydrides. Above the transition temperature DBTT, the radial hydrides behave ductile and there is no formation of cracks and therefore no brittle failure.

If only circumferential hydrides are present, there is also an influence of the temperature on the material behaviour. The damage to the material at low temperatures then consists of the development of elongated micro-voids, which grow and coalesce due to stretching. This means that the cladding material is ductile even at low temperatures, unless the hydride content is very high, as in the case of a hydride rim [3].

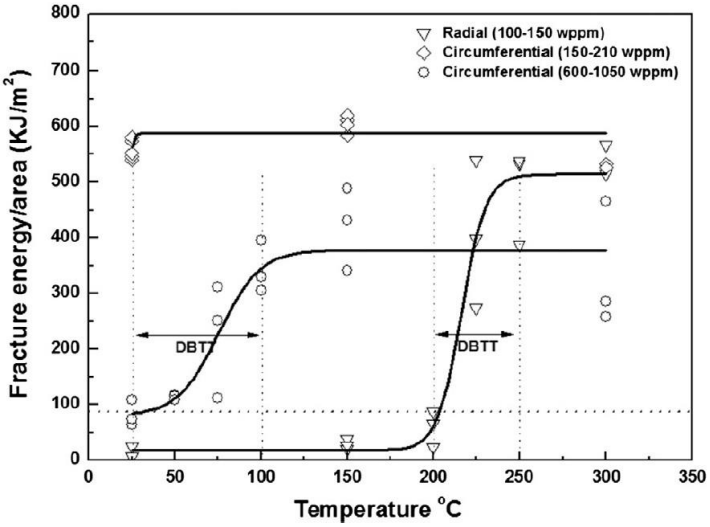

Figure 2 – Fracture energy as a function of temperature for radial and circumferential hydrides in a zirconium alloy (Zircaloy-4)

(Taken from Kim et al. [18])

The identification and analysis of the fracture mechanisms of a matrix-hydride composite material is difficult, as the heterogeneous microstructure of the zirconium alloys has a considerable influence on the failure behaviour and this heterogeneity severely limits the application of phenomenological or macroscopic fracture mechanics approaches. These physical heterogeneities, which span different spatial scales from the nano to the micro range, include local and internal stresses and strains between the matrix and the hydride inclusions, interfacial properties, grain boundary defects, grain morphologies and orientations, and dislocation density changes at the matrix-hydride interfaces [3]. In this context, Ziaei et al. [29] developed a nonlinear fracture mechanics methodology with a coupled dislocation density-crystal plasticity formulation that can describe hydride crack formation and hydride relationships based on morphological and crystallographic properties, defects and various interfaces related to intermediate crystallographic phases, grain boundaries and hydride populations. The fracture mechanics investigations in this work package are focussed on the brittle failure of a cladding tube with existing radial hydrides. Due to this limitation to a single but essential effect, a simpler approach with a phenomenological description of the deformation behaviour of the matrix material and a non-linear fracture mechanics description of hydride crack formation and crack propagation based on the macroscopic hydride morphology appears promising.

2.4 Creep

An effect that can influence the fuel rod integrity during dry interim storage is the creep of the cladding material. Thermal creep is the slow, irreversible deformation of the cladding at usually elevated temperatures and under long-lasting mechanical stresses that are still below the yield strength of the material. The creep behaviour of fuel rod cladding tubes depends on material parameters (e.g., alloy composition), the manufacturing process (e.g., cold forming, recrystallization annealing), the hydride content and the neutron flux during reactor operation. With irradiated materials, the radiation effects predominate. The two most important factors influencing the creep behaviour of irradiated cladding tubes are the hoop stress and the temperature. The hoop stress results from the internal fuel rod pressure, which in turn depends on the fission gas release during reactor operation. The temperature results from the decay heat of the fuel assemblies. At low temperatures and stresses, the deformation (circumferential expansion) of the cladding tube is negligible, but at high temperatures and stresses the deformation can be significant. A substantial creep effect is only to be expected with cladding tubes made of a zirconium alloy at temperatures above 350 °C [1]. With increasing storage time, both the internal pressure and the temperature decrease, so that the creep rate tends towards zero. The significantly higher temperatures resulting from the vacuum drying of the cask interior after loading with spent fuel assemblies can also influence the creep behaviour, especially in the initial phase of dry interim storage [30]. In creep tests on zirconium-based cladding tubes with a burn-up of up to 64 GWd/t_{HM}, no failure was observed at temperatures between 250 and 400 °C for up to 2 % creep strain [31]. For this reason, a conservative maximum creep strain of 1 % is used in Germany as the limit value for such fuel rod cladding tubes.

Depending on the load and temperature, several processes in the microstructure of the material play a role in creep: Dislocation slip, shape change by diffusion, dislocation climbing (renewal), and shape change by the ordered movement of point defects. The creep process can be divided into three stages (see Figure 3):

- Initially, the rate of deformation decreases with increasing elongation and over time. This stage is referred to as primary creep (I). The dislocation density in the material increases and the size of the dislocation cells decreases.
- The strain rate then reaches a minimum value and can be nearly constant. This is referred to as secondary creep (II). This stage can be considered a steady state. When specifying a minimum creep rate, this stage is usually meant. The stress dependence of this rate depends on the creep mechanism. The hardening and renewal processes in the material are in balance.
- In the stage of tertiary creep (III), the creep rate increases exponentially as a function of elongation. In this case, recrystallization dominates in the material, the coarsening of the second-phase particles begins, and the formation of voids and cracks begins. This continues until the sample finally breaks.

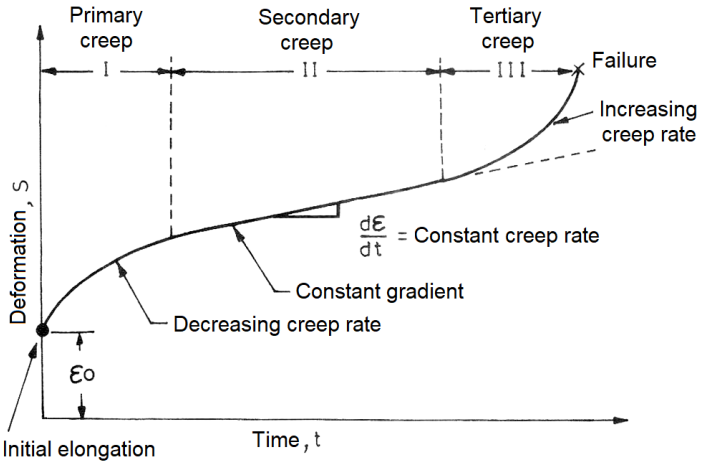

Figure 3 – The three stages of isothermal creep

3. Experimental Characterisation

3.1 Overview

The mechanical deformation behaviour of the cladding material is characterised by the quasi-static stress-strain (or flow) curve for low strain rates. The manufacturing process and thermo-mechanical pre-treatment of the cladding tube affect its material behaviour as well as its use during reactor operation. On the one hand, it is therefore not possible to determine the deformation parameters on standard samples prepared from the base material with the accuracy required for the work package. On the other hand, it is not possible to prepare samples for standardised tensile or pressure tests with the required geometric dimensions from a finished fuel rod cladding tube. Adapted experimental investigation methods are therefore required to measure the elastic-plastic deformation behaviour of a fuel rod cladding tube.

The elastic material parameters can be determined very precisely by crystallographic vibration analyses [32]. Table 1 (data taken from Weck et al. [32]) contains the isotropic elastic properties of common zirconium alloys relevant to this work package, which generally contain more than 95 % zirconium and differ mainly in their tin and niobium content: Zircaloy-4 or Zry-4 (incl. 1.2 to 1.7 % Sn), ZIRLO® (incl. 0.7 to 1.0 % Sn and about 1.0 % Nb), and M5® (incl. 0.8 to 1.2 % Nb).

Table 1 – Isotropic elastic material properties of common zirconium alloys

Material parameter	Zry-4	ZIRLO®	M5®
Bulk modulus K (GPa)	98.2	98.8	98.3
Shear modulus G (GPa)	39.4	33.9	32.6
Poisson's ratio ν	0.32	0.35	0.35
Young's modulus E (GPa)	104.2	91.3	88.1

As with standardised tensile or compression tests, it is not possible to prepare samples with the required geometric dimensions from the fuel rod cladding tube for standard fracture mechanics tests. If the sample geometry deviates from the standard, a special evaluation of the test data is required to compensate for the influence of the sample size. In fracture mechanics tests in particular, however, the failure mechanism can change depending on the sample size, so that this approach is only possible to a limited extent. The direct experimental investigation of samples from the cladding tube with a subsequent inverse, often numerical analysis of the test appears to be optimal for determining the wanted material properties. Some of the methods used for the experimental investigation of cladding tubes are presented below.

3.2 Three-Point Bending and Impact Tests

3.2.1 Experimental Setup

Three-point bending (TPB) and gravitational impact tests on filled pressurised spent nuclear fuel (SNF) rod segments were conducted in the hot-cell facilities at European Joint Research Centre Karlsruhe (JRC-KA) using two in-house developed devices described in detail in the literature [33, 34, 35, 36, 37]. Load-deflection curves were generated in the three-point bending tests, whereas a high-speed camera recorded the rod rupture during impact tests.

The force (or energy) required for a fuel rod to fail was prescribed by the experimental boundary conditions. As the accident scenarios to be tested are very numerous, it was decided to analyse the mechanical integrity of the SNF under two reference conditions by applying quasi-static or dynamic

loads. The acquired data were correlated to properties and processes that potentially affect the SNF mechanical stability. Metallographic examinations in the direct vicinity of the failure location to investigate the hydride morphology, population and orientation were carried out, whilst the local hydrogen content was measured by means of the hot gas extraction method. After the impact test, the released fuel particles were collected and examined by scanning electron microscopy (SEM) for morphology and size distribution analysis purposes.

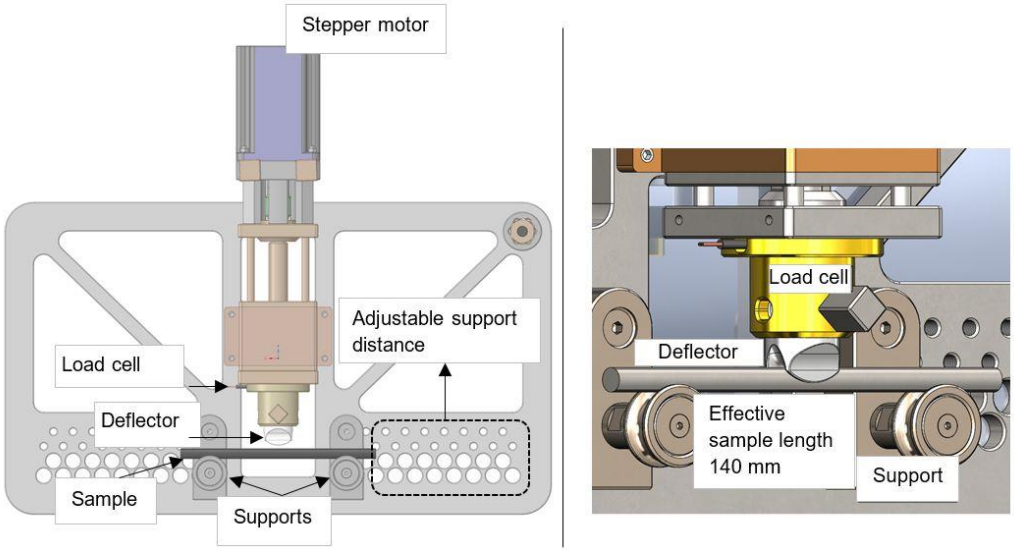

Figure 4 – Schematic overview of the bending device (left) and detail of the sample positioning and deflector (right) at JRC-KA

The three-point bending device is schematically shown in Figure 4. The apparatus consists of a force transmitter fixed on a loading column, which is driven by a stepper motor perpendicular to the sample axis at constant preselected (slow) speed between 4 and 17 µm/s. The force transmitter, the “deflector”, has a concave round contact surface (partly seen in Figure 4(right)), adjusted to the cladding shape, such that no other side or edge load is applied on the fuel rod segment during the test.

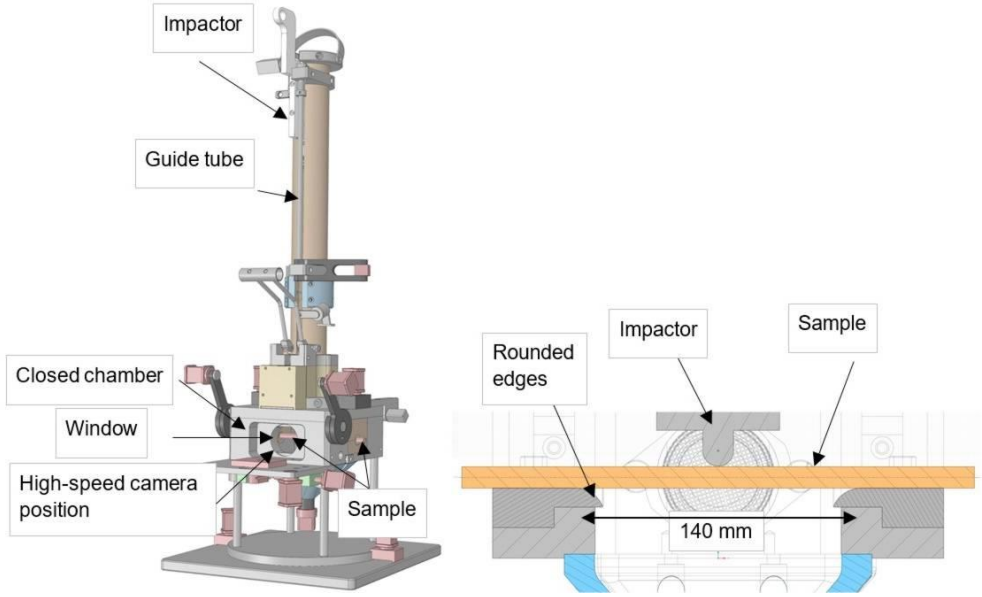

Figure 5 – Schematic overview of the impact device (left) and detail of the sample positioning and impactor (right) at JRC-KA

The flexible modular design of the device allows the use of different loading transmitters and, thanks to removable supports, different sample lengths. The geometrical configuration of the device follows the prerequisites of a standard bending test as specified in ISO 7438 standard [38]. The device is equipped with sensors for simultaneous acquisition of the applied load, the sample's deflection, and internal pressure of the segment.

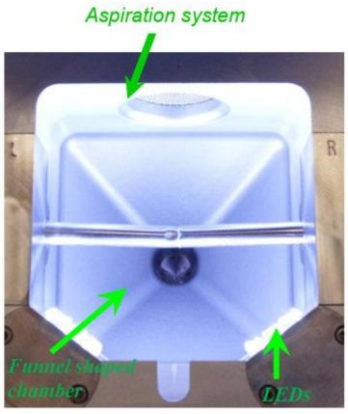

Figure 6 – Inside view of the closed test chamber of the impact device after a dummy cold test (cladding tube filled with aluminium pellets)

The apparatus for impact tests is based on the same principles as the older one used to perform the tests reported by Papaioannou et al. [39] and schematically shown in Figure 5. The impact occurs in a closed chamber, where the released material (basically fuel, but also pieces of the cladding and the outer cladding oxide layer) is completely captured. The coarse fragments are collected at the bottom thanks to the funnel shape of the lower interior of the chamber shown in Figure 6, whereas the fine aerosol particles settle on the internal walls, or are captured on the particulate filter of an integrated aspiration system (shown in Figure 6). The impact of the sample is recorded by a high-speed digital camera (2000 frames/s) placed on the window of the chamber, which is sufficiently illuminated by a series of LEDs placed on the inside wall. The sample is impacted by the “impactor”, a body (hammer) falling through a vertical guiding column.

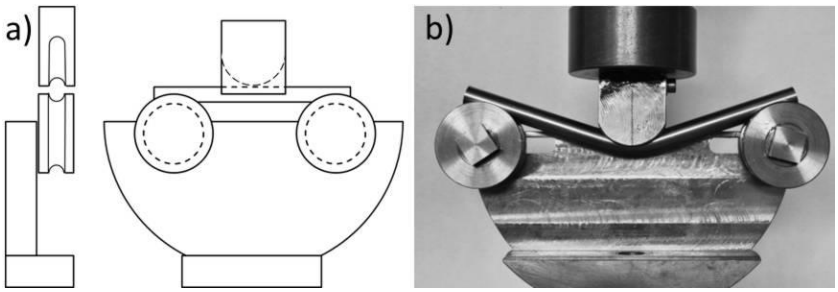

Figure 7 – Three-point bending test setup at UPM: drawing (a) and picture at the end of a test (b)

As far as possible, the designs of the bending and impact devices have been kept mutually consistent. In both experimental setups, the samples are bent or impacted by rounded compactors, as shown in Figure 4(right) and Figure 5(right). The effective length of the samples is the same, namely 140 mm. The main difference is related to the velocity of the impactor and bending deflector in the two setups, enabling direct comparison of the results in both configurations. Indeed, the velocity of the falling hammer at the moment of impact is 3.5 m/s (i.e., at least $2 \cdot 10^6$ times faster than in the three-point bending test).

At the Universidad Polytécnica de Madrid, E.T.S.I. Caminos (UPM), Madrid, Spain, a new three-point bending device for unirradiated samples was built with a design inspired by the test setup at JRC-KA for tests inside the hot cell. The supports are rollers with a concave-round contact surface to accommodate the cladding diameter, such that no other side or edge loads are applied to the sample during the test. The TPB sample is placed on two supports, while the load is applied from above by a roller with the same concave-round contact surface in the centre between the supports, as shown in Figure 7. The load applied by the upper roller and its displacement are measured during the test. The device was attached to a universal testing machine equipped with a 5-kN load cell.

For the high temperature test, the setup was placed in an electric furnace. The system was monitored with thermocouples. A calibration was performed to determine the relationship between the sample temperature and the control signal for the furnace temperature. During the tests at room temperature, pictures were taken every second.

3.2.2 Sample Material

One three-point bending and one impact test were performed within this work package at JRC-KA. The samples originate from a pressurised water reactor (PWR) SNF rod with heterogeneous mixed oxide $(U,Pu)O_2$ (MOX) fuel and duplex cladding that was irradiated up to 60.6 GWd/t_{HM}. They have been taken from the middle rod axis (that is, from the high burnup zone). In previous post irradiation examinations (PIE) of the SNF rod, measurements at neighbouring locations of the samples examined revealed a total hydrogen content of less than 250 wppm in the cladding. An overview of a cross-sectional sample in the central axial length of the rod and details of the hydrides in the duplex cladding are shown in the micrographs of Figure 8.

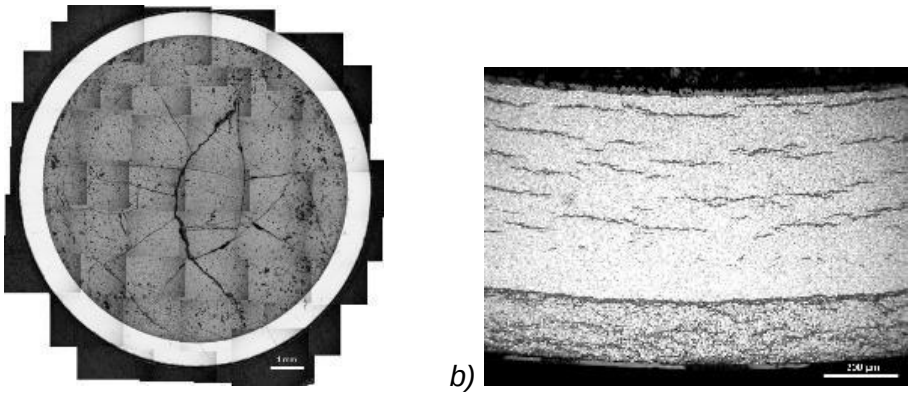

a) *b)*

Figure 8 – Light microscopic images of the cross section of the rod in the vicinity of the TPB and impact sample (a) and hydrides in the etched duplex cladding (b)

At UPM, three-point bending tests were performed on unirradiated ZIRLO® cladding samples with a diameter of 9.52 mm and a wall thickness of 0.57 mm. The material is cold-work stress-relieved and was supplied by ENUSA Industrias Avanzadas, S.A., in Spain.

3.2.3 Sample Preparation

At JRC-KA, the cut segments were pressurised at 40 bar and hermetically sealed with proper tube fittings as shown in the photograph of a typical sample for mechanical testing in Figure 9. Using exact tube fittings to preserve the required tightness, the roughly 26-cm-long segments cut from SNF rods were connected to a helium gas flask that was pressurised to the desired pressure and disconnected after closing the attached gas valve. A pressure transducer, which was attached to the other end of the segment, provided continuous pressure control and instant detection of a crack or rupture, which was essential in the bending tests.

Figure 9 – Gas-tight sample assembly connected to a pressure gauge and fitted with a pressure transducer, ready for mechanical testing

Depending on the planned tests at UPM, tube samples were cut in two different lengths: 50-mm-long samples for hydride reorientation and the ring compression tests (RCT) and 160 mm for the three-point bending (TPB) tests. Hydrogen was introduced by cathodic charging only through the external surface of the sample. The central part was exposed to hydrogen entry, while the remaining surface was masked with varnish. The inner part of the sample was sealed using rubber plugs. The target concentration in the cladding was 100 wppm hydrogen. A summary of the sample dimensions is shown inTable 2, where the length of the unmasked area is indicated.

Table 2 – Dimension of samples for hydrogen charging

Sample type	Total length (mm)	Unmasked length (mm)
Ring compression test	50	20
Hydride reorientation treatment	50	20
Three-point bending test	160	40

The cathodic charging was performed by introducing the sample (acting as the cathode) in a 0.1M KOH solution with a platinum electrode (acting as the anode) placed around the cladding sample. The current density (fixed at 0.25 A/cm^2, considering only the unmasked surface of the sample) was applied for three hours. A drawing of the experimental setup is shown in Figure 10. After charging, zirconium hydrides were precipitated by thermal treatment, which involved heating up to 450 °C and holding this temperature for 7 hours, followed by controlled cooling at 1 °C/min down to 200 °C.

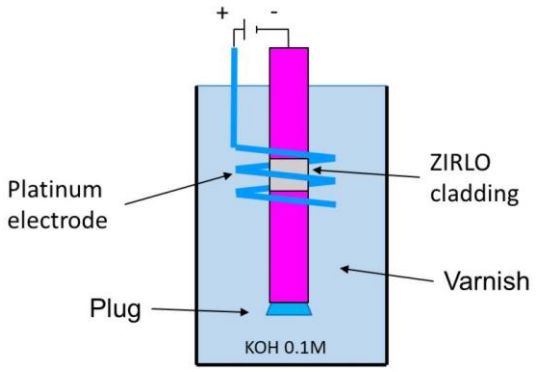

Figure 10 – Schematic representation of the experimental setup for cathodic charging

The hydrogen content was measured by inert gas fusion with a LECO OHN 836 analyser. The charged area was cut into 2-mm-high rings for this purpose. The average hydrogen content in the central 10 mm of the samples used for RCT (length of 50 mm) was 80 ± 7 wppm, while the average hydrogen content in the central 30 mm of the samples used for TPB (length of 160 mm) was 105 ± 3 wppm (Sample 1) and 104 ± 2 wppm (Sample 2). The values obtained for the two TPB samples are shown in Figure 11 depending on the distance to the sample centre. After charging, zirconium hydrides were precipitated by thermal treatment.

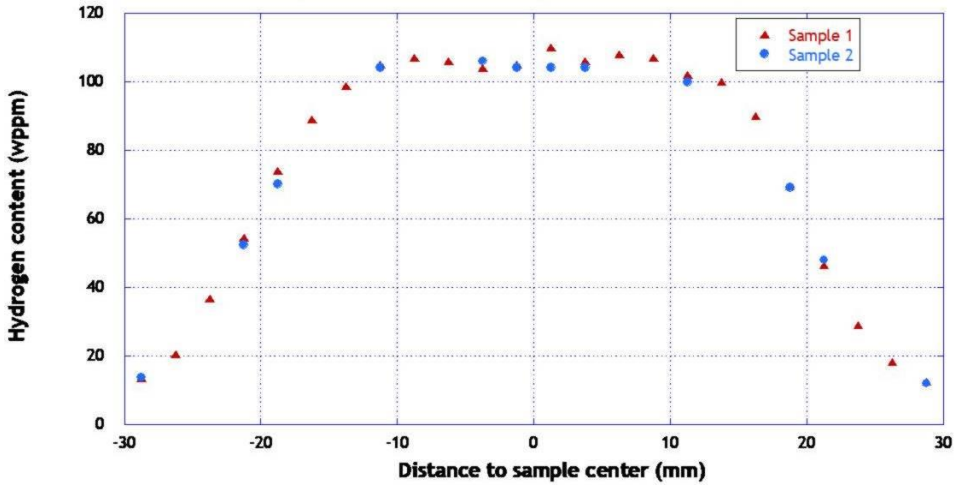

Figure 11 – Hydrogen content in three-point bending (TPB) samples depending on the distance to the sample centre

The results on the hydrogen content are confirmed by the hydride morphology observed in different cross-sections of Sample 2, as shown in Figure 12. The hydrides are the dark lines over the white background, which corresponds to the zirconium matrix. The hydride morphology is very similar in Figure 12(a) and Figure 12(b); both are located in the central 30 mm of the sample, where the hydrogen concentration is fairly homogeneous (around 100 wppm). Long hydrides (up to 500 µm) have precipitated in the circumferential-radial plane and are mainly located at the mid-thickness of the cladding (and close to the inner and outer surfaces). However, in the cross-section located at 22.5 mm from the centre (see Figure 12(c)), the hydrides are quite small (around 20 µm) and are randomly oriented. The hydrogen content in this section (masked zone to avoid hydrogen entry) is approximately 20 wppm.

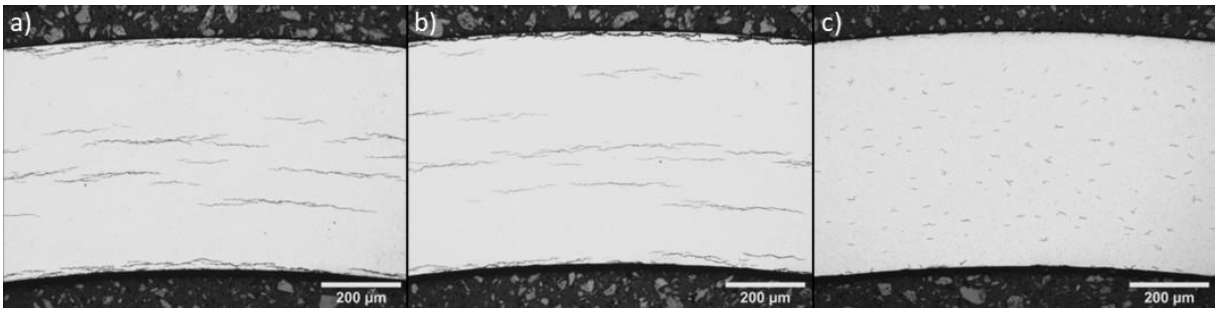

Figure 12 – Hydride morphology observed at several cross-sections of the TPB sample 2 located at 5 mm (a), 12.5 mm (b), and 22.5 mm (c) from the sample centre

Hydrogen measurements and metallographic analyses demonstrate that the cathodic charging process is well controlled and reproducible. The hydrogen content is approximately 100 wppm in the central 30 mm of the sample. The hydride precipitation treatment produces long circumferential hydrides mainly located at the mid-thickness of the sample. As it will be explained below, the diameter of the upper roller (TPB test) is approximately 28 mm. Consequently, both the hydrogen concentration and the hydride morphology in the sample section below the roller are quite homogeneous.

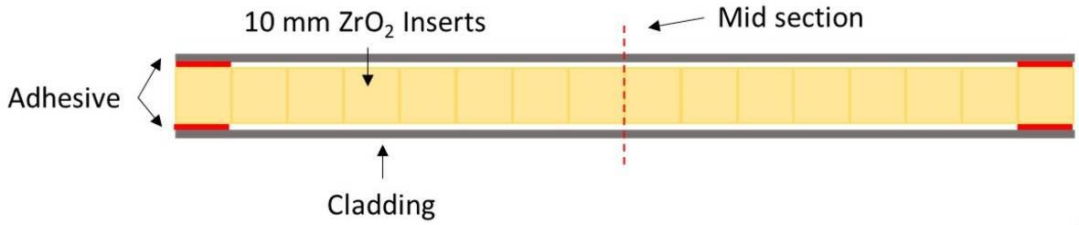

Figure 13 – Sketch of the surrogate rod with ZrO_2 ceramic inserts

In addition to hollow cladding tubes, surrogate rods with ZrO_2 ceramic inserts were also tested. ZrO_2 was chosen (instead of Al_2O_3, which is also reported in the literature) because of its Young's modulus, which is closer to the one of UO_2 pellets. The ZrO_2 pellets were cylinders with a diameter of 8.30 mm (resulting in an initial gap of 25 µm) and height of 10 mm, which were glued to each other and to the cladding (see Figure 13). Tests were performed at 20, 135 and 300 °C on as-received and pre-hydrided rod samples (using the charging procedure described above), both hollow and with surrogate pellets. The surrogate rod samples were carefully prepared such that the interface between two ceramic inserts was always located at the centre of the sample. It was assumed that this represents the worst-case scenario for the bending tests.

3.2.4 Measurement Campaigns

In the three-point bending tests at JRC-KA, which were carried out with 16.7 µm/s deflector translation, the load, displacement, and pressure were monitored. The corresponding profiles are shown in Figure 14.

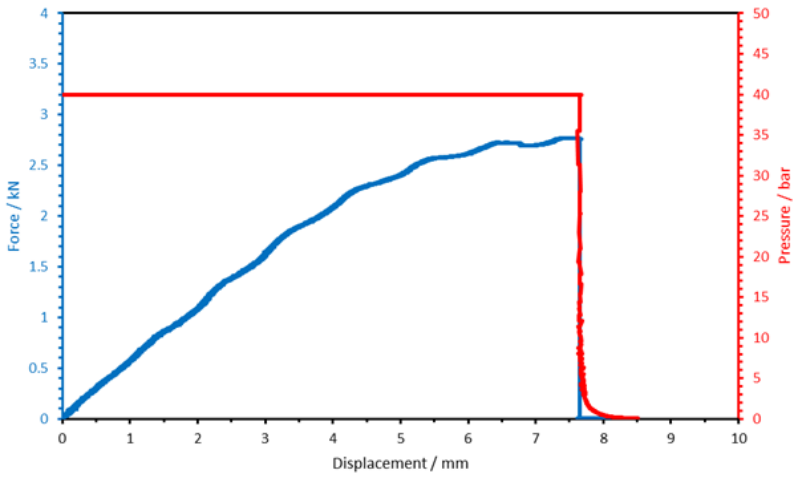

Figure 14 – Force (blue curve) and internal pressure (red curve) as function of the displacement during the three-point bending test

The rupture of the segment was detected simultaneously by load and internal pressure measurements. The failure caused a rapid drop of the applied force and pressure. The complete depressurisation of the segment after the initial drop took 40 to 45 seconds, which provides insight into the permeability of the fuel used with closed pellet-cladding gap. The total displacement of the deflector from immediately before contact until rupture was 7.6 mm, whereas the maximum load reached was 2.76 kN. This corresponds to an energy of 13.7 J absorbed from the sample until rupture. A mass release of 1.73 g was measured by weighing the sample and the broken segments before and after the test.

The impact test has been documented by the video recorded with the high-speed camera. The video has been used to calculate the transmitted energy from the hammer to the sample, which caused the rupture, by an image analysis system. As described in detail by Vlassopoulos [37] using the video recording, the transmitted energy from the hammer to the sample can be calculated based on the velocity change of the hammer between the moments of first contact and final rupture. The calculated energy that was transmitted until crack initiation in the sample was therefore 13.5 J in this impact test.

Representative photographs during the impact are presented in Figure 15. On first contact of the hammer, the outer oxide layer shatters; this is followed by cracking, depressurisation and major fuel release. To determine the amount of mass released, similar to the bending test, the fuel rodlet and the broken segments are weighed before and after the test. A total mass of 2.24 g was released during the impact test.

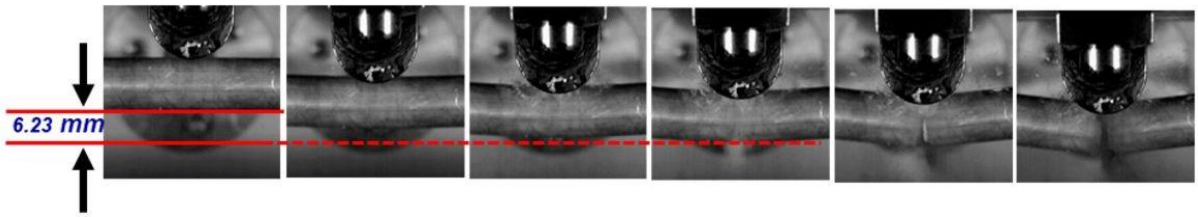

Figure 15 – Photograph sequence during impact of the MOX sample

Since the impact takes place in a closed chamber connected to an aspiration system through a particulate filter, the released fuel particles remain inside the test setup. Upon fracture, the heavy fragments fall in a vessel at the bottom of the chamber. The fine particles deposit on the walls and surfaces in the test chamber or are collected on the micro-filters of the aspiration system. The heavy fragments collected on the bottom of the test chamber after the test were sieved and weighed to sort them according to their size indicated by the equivalent circle diameter (ECD). The result of the characterisation of the heavy fuel particles is listed in Table 3.

Table 3 – Sizes and masses of the fragments collected on the bottom of the chamber after impact test

ECD fragment size (µm)	Fragment mass (g)
0 to 90	0.12
90 to 250	0.29
250 to 630	0.50
630 to 1000	0.43
>1000	0.70
Total	2.04

The "missing" 0.2 g or 0.9 % of the total mass released consisted of aerosol and fine particulates deposited on the inner walls of the test chamber or collected on the filters coupled with the aspiration pump, which evacuated the test chamber during and after the impact. The collected fine particles were submitted to scanning electron microscopy (SEM-EDS) and characterised in terms of size distribution. As a complement to the micro-filters, swipes of the test chamber walls were made at different locations to collect fine particles deposited on the walls. Both filters and swipes were examined. The size distribution analysis is summarised in Figure 16.

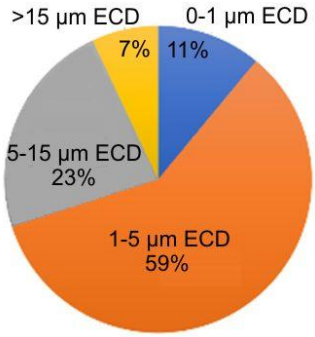

Figure 16 – Size distribution analysis based on the number of aerosol (ECD < 15 µm) particulates collected at the aspiration filter and side walls of the test chamber after impact test

Table 4 shows a summary of the three-point bending tests at UPM.

Table 4 – Test matrix for the three-point bending tests at UPM

Test temperature (°C)	Sample type	As-received	Pre-hydrided
20	hollow	1 test	1 test
	with inserts	1 test	2 tests
135	hollow	1 test	1 test
	with inserts	1 test	2 tests
300	hollow	1 test	1 test
	with inserts	1 test	2 tests

3.2.5 Main Results

The main conclusion of the three-point bending and impact tests on the MOX SNF rod segment at JRC-KA is that the released mass during rupture is limited to only 1.73 g and 2.24 g, respectively and much less than the mass of a single fuel pellet. The quantity released is comparable to the release from UO_2 SNF rods with similar burnups, as shown in Figure 17, where the fuel mass release in several tests performed at JRC-KA is plotted as function of fuel burnup [40, 41]. The rods studied cover an extended burnup range from 18 to 100 GWd/t_{HM}, preserve three different types of outer duplex claddings with hydrogen pickup between 50 to 300 wppm and without radial hydrides, and outer corrosion layer thicknesses from 4 to 23 µm.

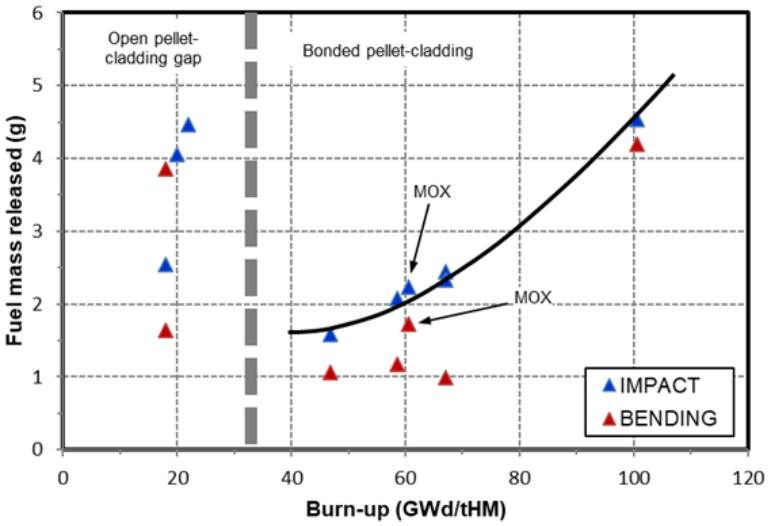

Figure 17 – Fuel mass released during bending and impact tests at JRC-KA depending on the fuel burnup

The blue data points in Figure 17 represent the released mass after impact and rupture of a SNF rod as function of burnup. The data are sorted in two major groups depending on the open or closed pellet-cladding gap respectively, separated by the grey dashed line in the plot. At average burnups up to approximately 33 GWd/t_{HM} the fuel pellets are not strongly bonded with the cladding tube. The fuel pellets are broken in relatively large (4 to 5 mm) fragments; at rupture some of them may escape from the cladding tube. This is the reason for the big scatter of the data points in the region “open pellet-cladding gap”. The released masses, however, never exceeded 5 g. The fact that the cladding retains some of its initial ductility in this low burnup range and is plastically deformed by the external load in the vicinity of the rupture facilitates the fuel fragments remaining in the cladding tube. As soon as the fuel pellets contact and bond with the cladding, a clear trend is observed in the right part of Figure 17. With increasing burnup, higher mass releases were observed when the SNF rods broke. Nevertheless, even at extremely high burnups, the masses released were less than 5 g. The cladding becomes less ductile at high burnups, but due to the pellet-cladding bonding, the fuel is well kept inside the cladding tube and the release is therefore limited. The lowest masses released at an impact are expected at burnups around 35 to 40 GWd/t_{HM}. For comparison reasons the measured masses released at rupture after the three-point bending tests are also plotted in Figure 17 (red data points). It was found, that these masses are generally lower than those of the impact tests. This is due to the fact that the bending tests are very slow and not dynamic and the energy transferred to the sample is somewhat lower: 13.5 J in the bending test against 13.7 J in the impact test of the MOX fuel rod.

The fuel dominates the overall SNF behaviour beyond the effects of the different cladding types. The individual properties of the cladding itself have no clear influence on the fuel quantities released. Despite the low number of tests, a trend of the SNF rod behaviour in three-point bending tests can be predicted in the next two plots. As function of burnup, the maximum measured loads for rupture are presented in Figure 18, whereas the corresponding displacements are plotted in Figure 19 [40, 41].

The partly retained cladding ductility at low burnups is reflected in the lower rupture loads around 2 kN. Between 20 and 50 GWd/t_{HM}, approximately 25 % higher loads are required due to irradiation hardening. A load of 2.5 to 3 kN is needed to rupture fuel rodlets with even higher burnups up to 100 GWd/t_{HM}. In Figure 19, the ductility and the open fuel-cladding gap at lower burnups are the reasons for the higher displacements in bending. At burnups above 40 GWd/t_{HM} and with closed gap, the measured displacement at rupture appears to be fairly constant, between 6.5 to 11.5 mm, for all tests performed [40, 41].

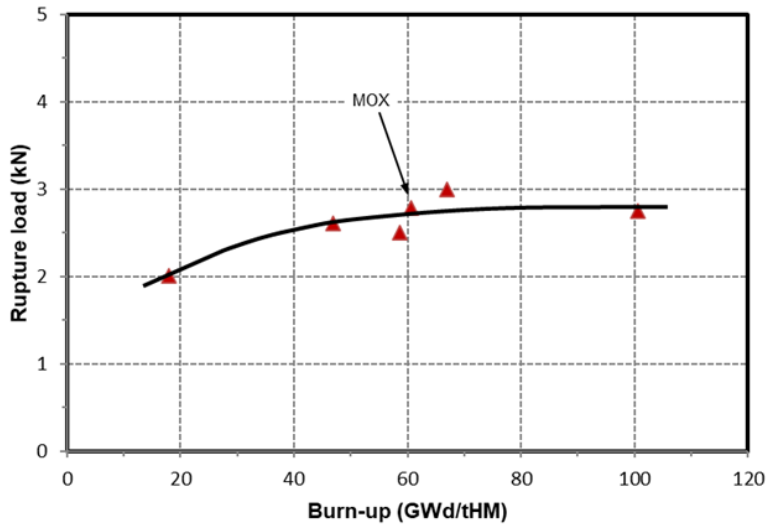

Figure 18 – Comparison of the maximum rupture load as a function of fuel burnup measured in the three-point bending test on a MOX rod and UO_2 rods, obtained at JRC-KA

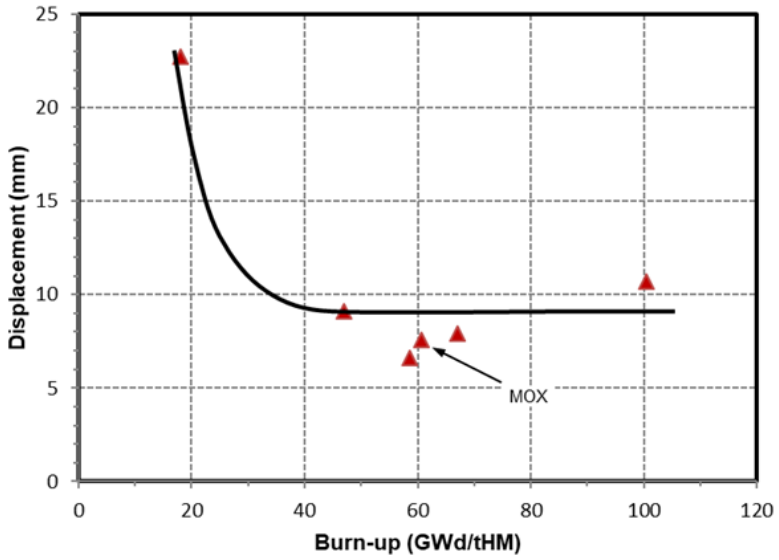

Figure 19 – Comparison of the maximum displacement at rupture as a function of fuel burnup measured in the three-point bending test on a MOX rod and UO_2 rods, obtained at JRC-KA

The load-displacement diagrams corresponding to three-point bending tests on as-received and pre-hydrided samples (without ceramic inserts) at UPM are shown in Figure 20 for the three temperatures 20, 135, and 300 °C. The as-received and pre-hydrided samples exhibit a very similar behaviour at each testing temperature. The load increases with the displacement at the contact point until the maximum load is reached. After that, the load decreases slowly without any remarkable drop. The sample deforms plastically (as illustrated in Figure 7(b) without any visible cracking. The final load drop is due to the unloading at the end of the test. The maximum load decreases with temperature, with values ranging from 1.1 kN at 20 °C to 0.8 kN at 300 °C. The displacement corresponding to the maximum load is similar for all temperatures and no significant differences are found between as-received and pre-hydrided samples. These results indicate that circumferential hydrides do not affect significantly the

mechanical behaviour of cladding in three-point bending tests. This is because the direction of the maximum stress (axial in this case) is parallel to the plane where the hydrides precipitate (radial-axial). Consequently, circumferential hydrides will not have an influence in TPB tests on unirradiated pre-hydrided cladding.

The code used to identify the TPB samples is as follows: TPB_XX_Y_ZZZ_VV, where:

- TPB means three-point bending,
- XX is the sample state ("AR": as received, or "PH": pre-hydrided),
- Y is the sample type ("H": hollow, or "P": with surrogate pellets),
- ZZZ is the test temperature ("020": 20 °T, "135": 135 °C, or "300": 300 °C),
- VV is the running test number.

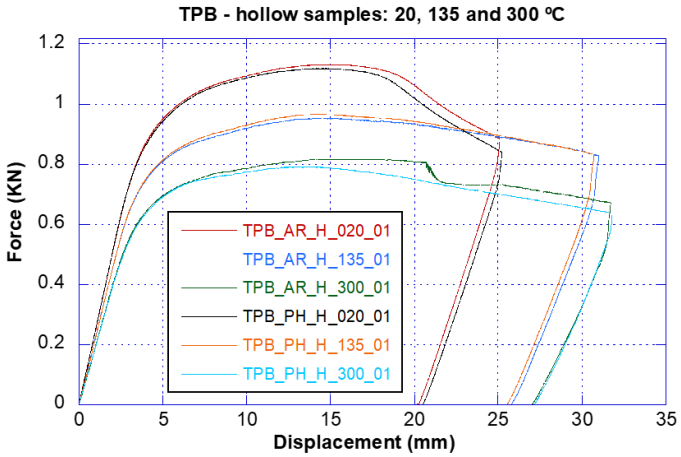

Figure 20 – Load-displacement curves from three-point bending tests for as-received and pre-hydrided samples without ceramic inserts at 20 °C, 135 °C and 300 °C

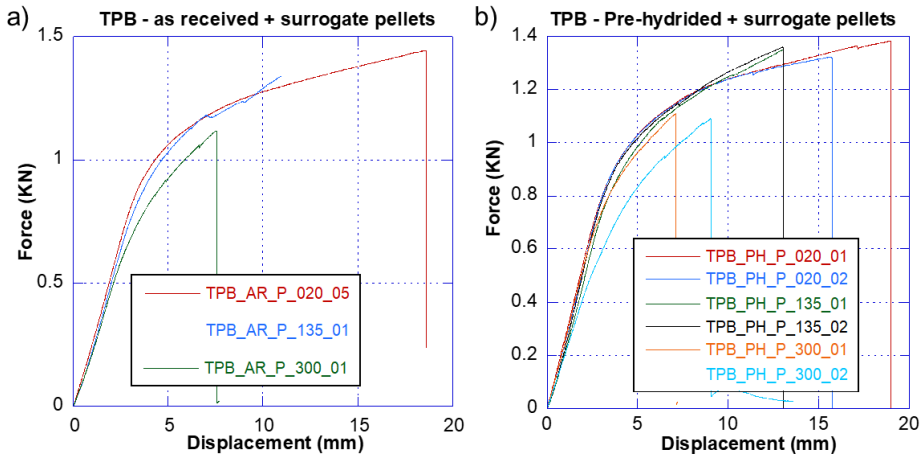

Figure 21 – Load-displacement curves from three-point bending tests for as-received (a) and pre-hydrided (b) samples with ceramic inserts at 20 °C, 135 °C and 300 °C

The load-displacement diagrams for samples with surrogate pellets (as-received and pre-hydrided) are depicted in Figure 21. The behaviour is different from the one observed for the empty samples. The load increases with displacement (of the load application point) until a given value, when the sample fails suddenly and the load decreases to zero. This load drop is associated with the initiation and propagation

of a crack in the central cross-section of the cladding, which coincides with the separation between two ceramic inserts. The crack starts at the lower part of the cladding, opposite to the load application point, and propagates upwards through the cladding wall. The plots are quite similar at the different temperatures, although the load and displacement at failure decrease with temperature. As this happens both for the as-received and pre-hydrided samples, it can be concluded that the mechanical response is dominated by the presence of the ceramic inserts.

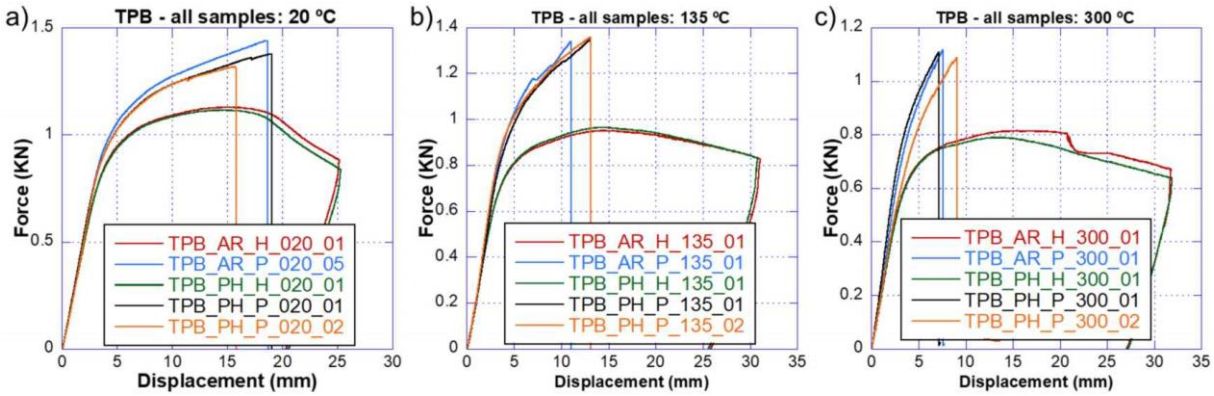

Figure 22 – Load-displacement curves from three-point bending tests for all samples at 20 °C (a), 135 °C (b) and 300 °C (c)

The experimental results are grouped by temperature in Figure 22 to better understand this behaviour. For any given temperature, all the hollow samples behave in a similar way independently of the presence of hydrides. This also happens in the samples with ceramic insert. By comparing all the samples tested at the same temperature, it can be seen that the maximum load in the hollow samples is approximately 75 % of the load of the samples with ceramic inserts. Furthermore, it can be seen that for the samples tested at 20 °C the displacement at maximum load for the samples with pellets is higher than for the hollow samples, while both values are similar for the samples tested at 135 °C. Conversely for the samples tested at 300 °C, the displacement at maximum load of the hollow samples is higher than for the samples with pellets.

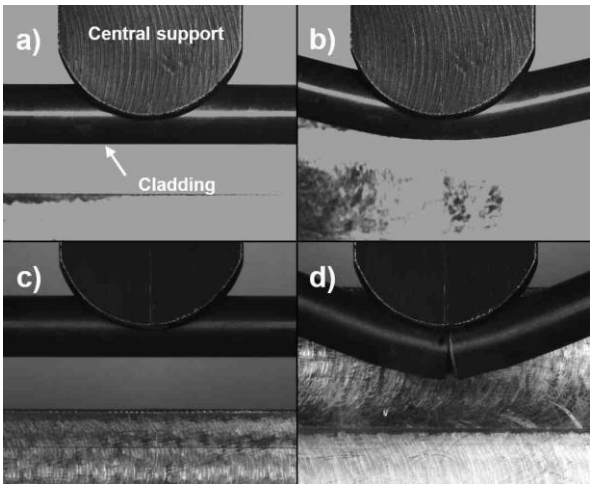

Figure 23 – TPB tests on sample TPB_PH_H_020_01 at test start (a) and maximum load (b) as well as on sample TPB_PH_P_20_01 at test start (c) and maximum load (d)

Figure 23 shows four images taken during TPB at the beginning of the test and at maximum load. For the hollow sample (see Figure 23(a) and Figure 23(b)) at maximum load, the sample is deformed but no cracks are visible. For the sample with ceramic inserts (see Figure 23(c) and Figure 23(d)), a crack appears at the central cross-section of the sample. This crack starts at the bottom of the sample and propagates upwards, as previously explained.

3.3 Ring Compression Test

3.3.1 Experimental Setup

At JRC-KA, two different devices were used to perform ring compression tests (RCT) of irradiated cladding samples as part of this work package. The first RCT on a sample from the upper plenum of a PWR SNF rod with average burnup (BU) of 67 GWd/t_{HM} was carried out with the modified three-point bending device used to perform the bending tests in Section 3.2. By exchanging some parts of the bending device, the equipment was capable to carry out a RCT. As shown schematically in Figure 24, a horizontal table is attached to the lower side of the metal frame of the machine, on which the cladding sample is placed and held in position by means of side holders until it comes into contact with and is loaded by the flat cylindrical deflector. However, during this first RCT, the device, which had already been used over a long period of time and for many tests in the highly radioactive environment of a hot cell, showed slight malfunctions. That's why the brand new equipment in Figure 25 was built in the workshop of JRC-KA. The device is based on the same technical principle as the older one, but attempts have been made to incorporate more robust components. It was installed in a hot cell after “cold” tests had previously been carried out with unirradiated samples and the results had been compared with those of other laboratories (UPM, JRC-PETTEN). The applied load and the corresponding displacement were continuously recorded in all RCTs conducted as part of this work package. The load is applied at a low constant speed of 4.9 µm/s, and the tests were also recorded with a video camera.

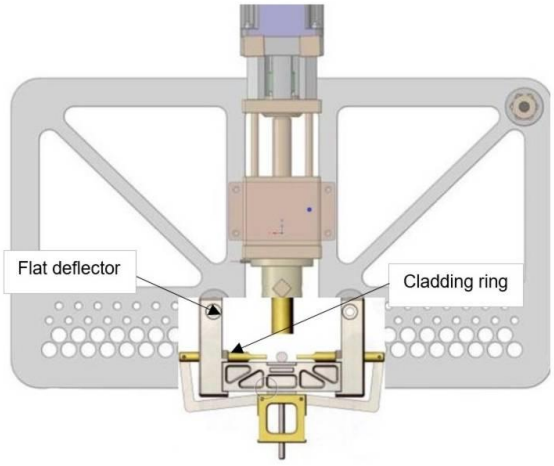

Figure 24 – Overview of the modified bending device to perform ring compression tests on irradiated cladding materials at JRC-KA

In the ring compression test at UPM, the sample was placed between two parallel plates, where one was moved towards the other. The tests were carried out using a universal testing machine equipped with a 5-kN load cell. The load applied by the upper plate and its displacement were recorded during the test.

For the high temperature test, the setup was placed in an electric furnace. The system was monitored with thermocouples. A calibration was performed to determine the sample temperature as explained in Section 3.2.1. During the tests at room temperature, pictures were taken every second.

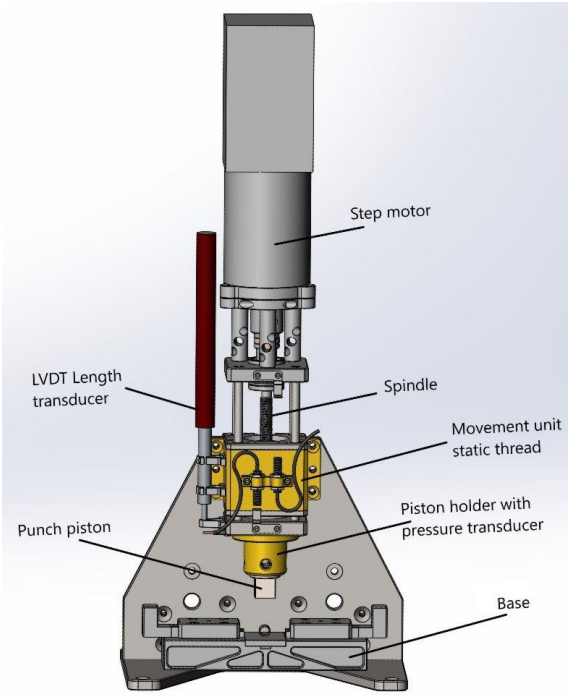

Figure 25 – Overview of the new device constructed at JRC-KA to perform ring compression tests (and bending tests) on irradiated cladding materials

3.3.2 Sample Material

At JRC-KA, the samples used in the ring compression tests were approximately 10-mm-long and cut from three different PWR SNF rods: the rod T16 with average burnup (BU) of 67 GWd/t_{HM}, the rod A11 with low BU of 18.3 GWd/t_{HM}, and the rod 13D02 with ultra-high BU of 100.5 GWd/t_{HM}. The three claddings are duplex claddings and the rings were obtained either from the upper plenum of the fuel rods or fuel stack locations with open pellet-cladding gap, hence no mechanical or chemical defueling of the cladding rings was necessary. Their locations are schematically indicated by the red squares in Figure 26. The samples are labelled by the fuel rod name followed by the number written in the black squares in Figure 26 (e.g., T16-9-3, A11-6-7, or 13D02-8-2-5).

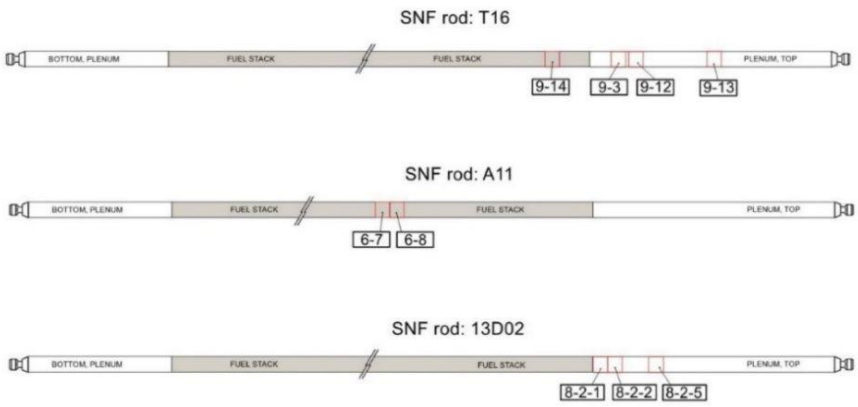

Figure 26 – Position and labelling of the 10-mm-long RCT samples (red squares) in the fuel rods T16, A11 and 13D02

Metallographic analyses of the claddings and hydrogen content measurements with the hot extraction method were performed during the post irradiation examinations of the three SNF fuel rods at locations of the upper fuel stack. Micrographs of the three duplex claddings studied are shown in Figure 27; the outer layer of the duplex claddings are indicated by arrows. The corresponding hydrogen contents measured are 300 wppm for the rod T16, 53 wppm for A11, and 95 wppm for 13D02. Based on previous results, the plenum cladding in the direct vicinity of the fuel stack contains hydrides, but less than those measured at the upper fuel stack position, depending also on its axial distance. Detailed information on the duplex cladding of the rod T16 can be found in Arborelius et al. [42] and on page 106 of Vlassopoulos [37] (and in further relevant references of this PhD thesis) for the claddings of the rods A11 and 13D02.

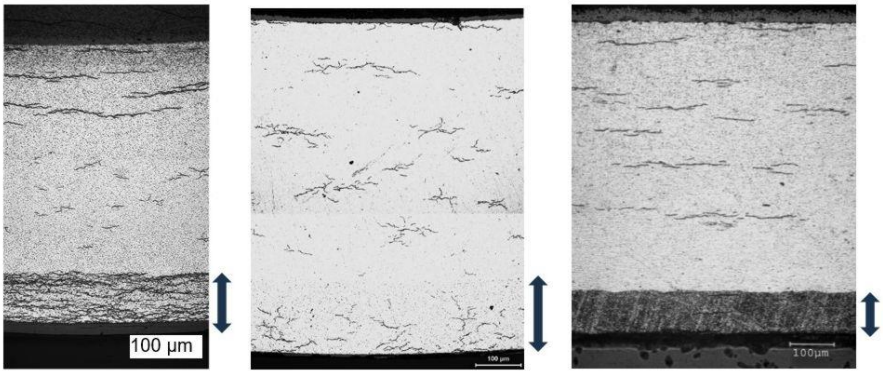

Figure 27 – Micrographs of the three duplex claddings showing hydrides at an upper fuel stack location of SNF rod T16 (a), at a location of SNF rod A11 very close to the RCT samples (b), and at an upper fuel stack location of SNF rod 13D02 (c)

At UPM, ring compression tests were performed on unirradiated ZIRLO® cladding samples with a diameter of 9.52 mm and a wall thickness of 0.57 mm. The material is cold-work stress-relieved and was supplied by ENUSA Industrias Avanzadas, S.A., in Spain.

3.3.3 Sample Preparation

The sample preparation was relatively simple at JRC-KA, as in all cases the cladding rings could just be cut and no particular mechanical or chemical defueling was required. In the case of the two A11 samples, the fuel of the cut rings could be easily removed, as at BU of 18.3 GWd/t_{HM} the fuel is not bonded with the cladding. The low local burnup permitted the simple removal of the non-bonded fuel also in case of the sample T16-9-3. The other samples studied are originating from the upper plenum and were not in contact with the fuel pellets and could be submitted to RCT without any particular treatment. The only difficulty experienced during the sample preparation was the non-precise cutting of exact 10-mm-long rings inside the hot cell using the tele-manipulators.

Tube samples with a length of 50 mm were prepared for the RCT at UPM. Hydrogen was introduced by cathodic charging only through the external surface as explained in Section 3.2.3. The target concentration was 100 wppm. After charging, zirconium hydrides were precipitated by a thermal hydride precipitation treatment (PT) that was also explained in Section 3.2.3.

The hydrogen content was measured by inert gas fusion with a LECO OHN 836 analyser. The values obtained are shown in Figure 28 depending on the distance to the sample centre. It can be seen that the hydrogen content is quite homogeneous (around 80 wppm) in the central 10 mm of the samples.

A radial hydride treatment (RHT) to reorient circumferential to radial hydrides was performed by applying internal pressure and temperature. The samples were sealed using stainless steel fittings and connected

to an argon bottle using stainless steel tubing. After attaching a thermocouple, the samples were placed in an electric furnace. A sketch and a picture of the experimental setup are shown in Figure 29. The procedure consisted of different steps. First, the sample was heated up to 400 °C; this temperature was maintained for 80 minutes without internal pressure. Then, argon was slowly introduced into the tube sample until the internal pressure reached 19 MPa. Pressure and temperature were maintained for 30 minutes. Afterwards, the sample was cooled down at 5 °C/h until 200 °C. Then, the furnace was turned off and the system was allowed to cool down to room temperature. The internal pressure was kept constant during cooling. The internal pressure value was calculated to produce an average hoop stress equal to 140 MPa.

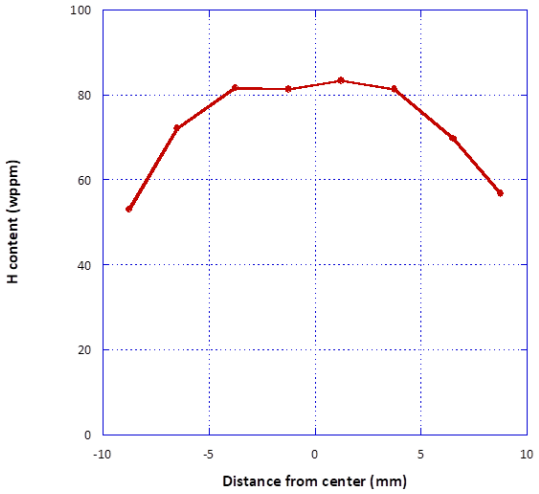

Figure 28 – Hydrogen content in RCT samples depending on the distance to the sample centre

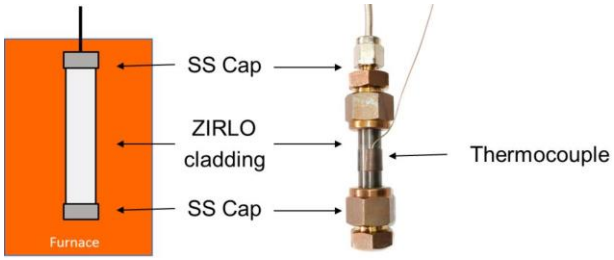

Figure 29 – Sketch (left) and picture (right) of a sample prepared for hydride reorientation treatment

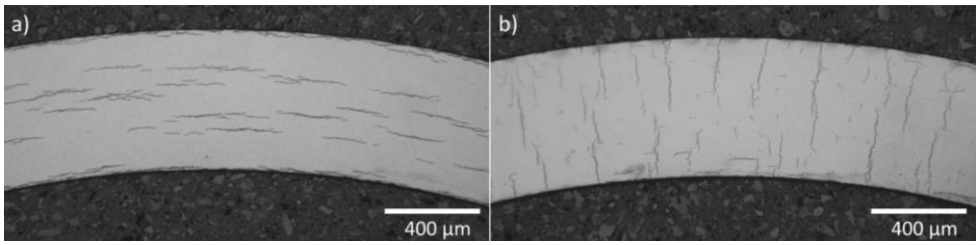

Figure 30 – Hydride morphology of cladding samples before (a) and after (b) the hydride reorientation treatment

Figure 30 shows the hydride morphology before (a) and after (b) the hydride reorientation treatment. Before the treatment, hydrides are in circumferential direction in the sample. After the treatment, most

of the hydrides are aligned in the radial direction; they extend almost from the inside to the outside of the cladding wall.

The RCT samples with a length of 10 mm were cut from the 50-mm tube samples after the hydride precipitation treatment and the radial hydride treatment. In addition to hollow cladding tubes, surrogate rods with ZrO_2 ceramic inserts were also tested. The ZrO_2 pellets were cylinders with a diameter of 8.30 mm (resulting in an initial gap of 25 µm) and height of 10 mm, which were introduced into the cladding tube.

3.3.4 Measurement Campaigns

The obtained data from the first RCT on the sample T16-9-3 at JRC-KA, which was conducted with the previous device used to perform the bending test in Section 3.2, are plotted in Figure 31 together with the curve of a cold test on a fresh, unirradiated Zircaloy-4 cladding ring of the same dimensions for comparison. The attached photographs illustrate the sample deformation at characteristic instants during the test and were placed with the middle of the photograph at the corresponding displacements.

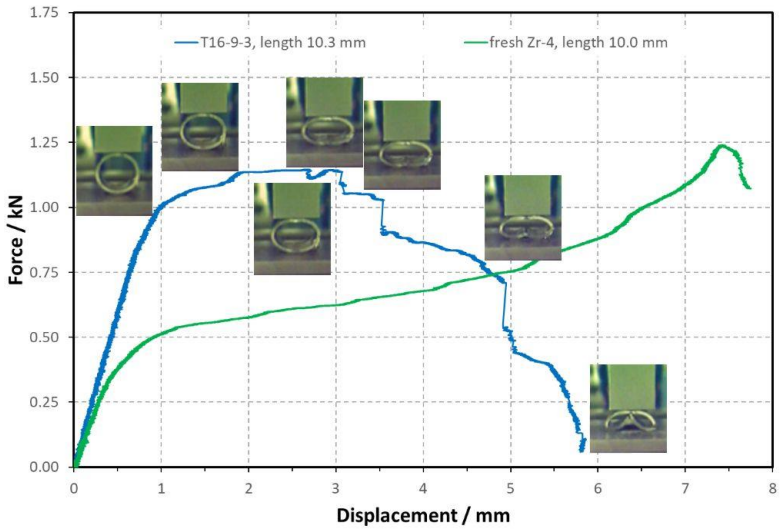

Figure 31 – Load-displacement curves in the RCT (previous device) on duplex cladding sample T-16-9-3 and a fresh (unirradiated) Zircaloy-4 cladding sample for comparison

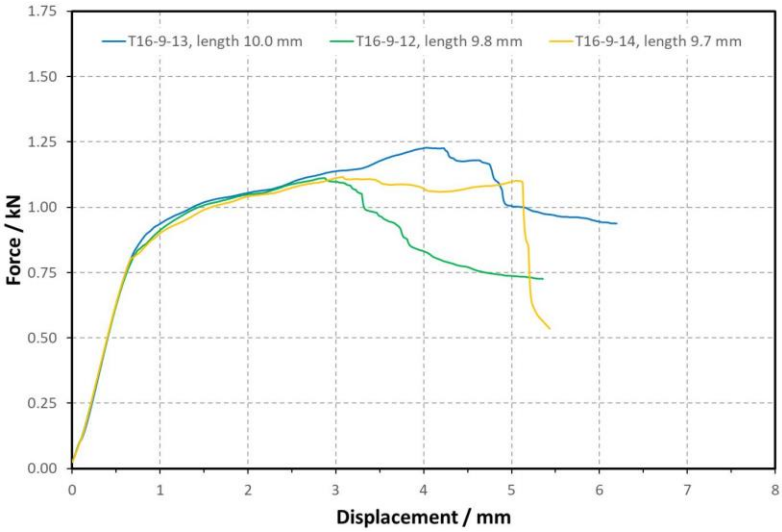

Figure 32 – Load-displacement curves in the RCT (new device) on the duplex cladding samples T-16-9-13, T-16-9-12 and T-16-9-14 from the SNF rod T16

All the next RCT were performed with the new equipment. Another three RCT on samples from the rod T16 are presented in Figure 32. The cladding ring for sample T16-9-14 was in contact with the fuel. The other two samples were taken from the rod's upper plenum. The results on samples from the rods A11 and 13D02 are shown in Figure 33 and Figure 34. The samples from the rod A11 were in contact with the fuel. All samples from the rod 13D02 were taken from the rod's upper plenum. It is to underline that any evaluation of the results should consider the particular sample length, which in most cases is deviating from the aimed 10 mm. For instance, the shorter sample in Figure 33 shows a lower load level and shorter displacement at failure.

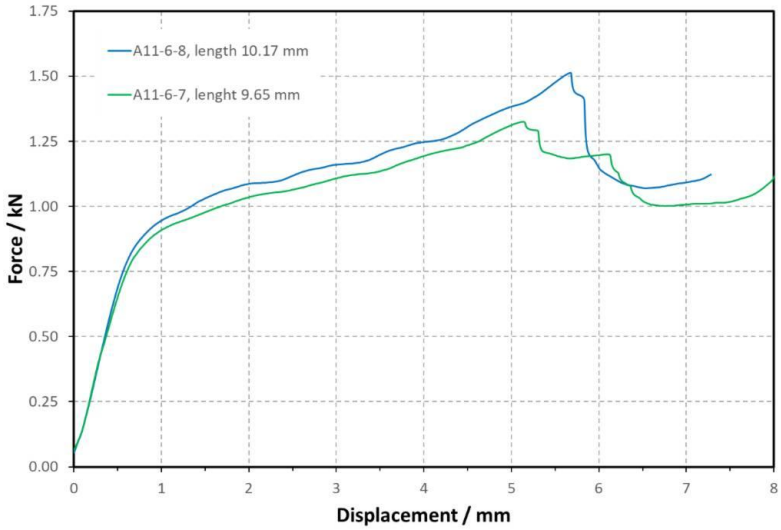

Figure 33 – Load-displacement curves in the RCT (new device) on the duplex cladding samples A11-6-7 and A11-6-8 from the SNF rod A11

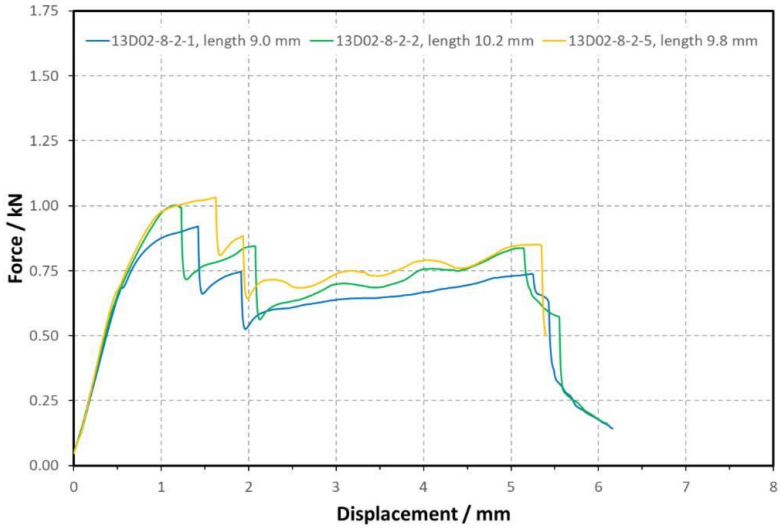

Figure 34 – Load-displacement curves in the RCT (new device) on the duplex cladding samples 13D02-8-2-1, 13D02-8-2-2 and 13D02-8-2-5 from the SNF rod 13D02

At UPM, ring compression tests were performed on samples with circumferential (after PT) and radial (after RHT) hydrides, both hollow and with surrogate pellets, at temperatures of 20, 135 and 300 °C. The test matrix is shown in Table 5.

Table 5 – Test matrix for the ring compression tests at UPM

Test temperature (°C)	Sample type	PT (circumferential hydrides)	RHT (radial hydrides)
20	hollow	3 tests	3 tests
	with inserts	2 tests	1 test
135	hollow	3 tests	3 tests
	with inserts	none	none
300	hollow	3 tests	3 tests
	with inserts	none	none

3.3.5 Main Results

At JRC-KA, despite the differences in metal composition and structure (duplex/liner vs. homogeneous Zircaloy-4) of the two cladding materials presented in Figure 31, significant effects due to irradiation can be observed by comparing their curves. Although the highest load applied is quite similar (about 1.14 and 1.25 kN, respectively), the overall displacement of the irradiated sample till its complete rupture in four pieces is much shorter. The cracking took place progressively; four well-distinguishable load drops can be seen at displacements of about 2.6, 3.1, 3.5, and 4.9 mm. In both cases, the elastic limit is reached at a displacement of about 1 mm, but with double load for the irradiated sample (1 vs. 0.5 kN). In Figure 32, the sample T16-9-13 shows a higher maximum load (of about 1.23 kN) and displacement at the beginning of failure, as it is originating from the most distant axial position in the plenum and should contain less hydrides than all the other T16 samples. The samples T16-9-12 and T16-9-14, which were in contact with the fuel, show the same maximum load of 1.11 kN (very close to the value of 1.14 kN from the sample T16-9-3 measured with the old device in Figure 31). The resistance of the sample T16-9-14, which was in contact with the fuel, is remarkable because of the final cracking at a displacement of more than 5 mm.

The two different sample lengths are clearly reflected in the curves of Figure 33. The shorter sample requires lower load and shorter displacement until final deformation. The samples with the low burnup of 18.3 GWd/t_{HM} retain their ductility; their curves are progressing smoothly, similar to the non–irradiated Zircaloy-4 curve in Figure 31, but with the main difference of the higher maximum loads (between 1.31 and 1.53 kN) and shorter maximum displacements. In comparison to the other results presented, this duplex cladding with the lowest burnup and hydrogen content shows the highest stability of all the irradiated samples.

Finally, the successive load drops in the curves in Figure 34 differ greatly from the other results. All 13D02 samples cracked first at displacements between 1.22 and 1.63 mm after reaching their maximum loads slightly above 1 kN (or 0.92 kN for the much shorter sample 13D02-8-2-1, respectively), cracked again at a displacement of about 2 mm and collapsed after a displacement of 5 mm. The relatively low hydrogen content of (actually less than) 95 wppm in this duplex cladding at the rod's upper plenum, from where the samples were cut, cannot explain this behaviour. The very high burnup of 100.5 GWd/t_{HM} of this SNF rod and the extended radiation damages might be more likely the reason for this.

Figure 35 shows typical load-displacement curves of RCT for the PT samples (with circumferential hydrides) and RHT samples (with radial hydrides) without ceramic inserts at 20, 135 and 300 °C, measured at UPM. In the PT samples, the load increases monotonically with the displacement. The maximum load decreases with temperature, from about 1 kN at 20 °C to less than 0.8 kN at 300 °C, while the displacement value, at which the maximum load is reached, increases from 5 mm to about 7 mm. On the other hand, RHT samples tested at 20 and 135 °C show sudden load drops in the linear

region of the curves at the beginning of the test. Load drops occur at displacements around 0.3 mm and loads between 0.2 and 0.25 kN, followed by small load increases and new load drops. These load drops are associated with cracks in the radial direction. Samples with radial hydrides tested at 300 °C exhibit the same behaviour as the samples with circumferential hydrides tested at the same temperature.

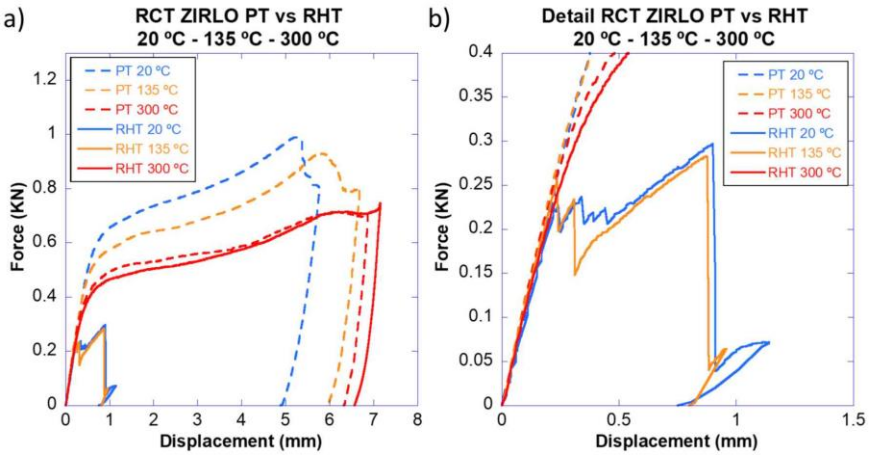

Figure 35 – Representative load-displacement curves from RCT for PT and RHT samples without ceramic inserts at 20, 135 and 300 °C: general view (a) and detail of the initial region (b)

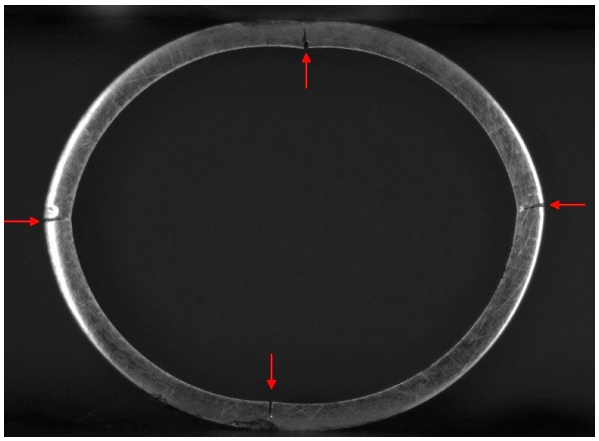

Figure 36 – Sample after RHT during RCT at 20 °C with radial cracks at the inner surface (6 and 12 o'clock position) and at the outer surface (3 and 9 o'clock position)

Figure 36 shows a picture of a sample with radial hydrides during the RCT at 20 °C. The cracks that appeared during the test are marked with red arrows. These cracks propagate in radial direction from the inner side of the cladding at the 6 and 12 o'clock positions and from the outer side of the cladding at the 3 and 9 o'clock positions. The cracks appear on radial hydrides at these locations because those are the areas where the highest hoop stresses occur. Some of these cracks are, however, not found exactly at the 3, 6, 9, or 12 o'clock position because of the stress state and hydride morphology. As there are only a few radial hydrides in the samples subjected to RHT (see Figure 30(b)), a suitable hydride could be missing near the inner cladding surface at the 6 and 12 o'clock position or near the outer surface at the 3 and 9 o'clock position. Thus, crack initiation will occur on the radial hydride with the highest fracture mechanics load, which depends on the hydride size in the regions with the highest hoop stresses.

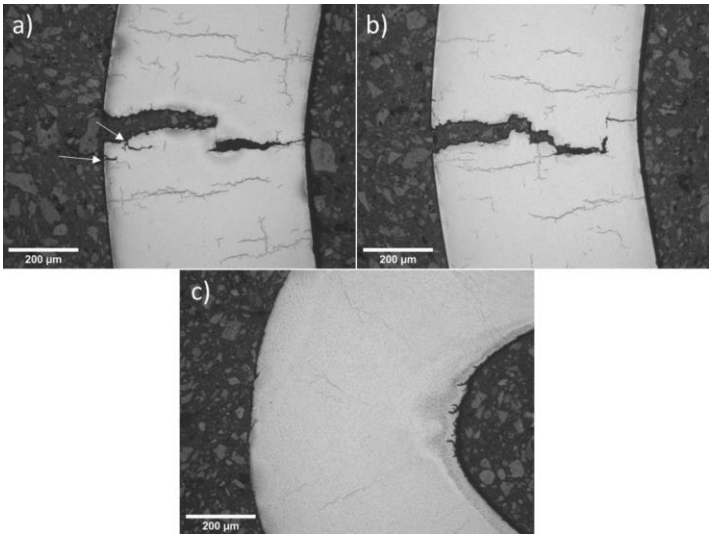

Figure 37 – Micrographs of RHT samples at 9 o'clock position after RCT at 20 °C (a), 135 °C (b) and 300 °C (c)

After the tests, some samples were prepared by metallographic techniques and investigated using optical microscopy. Figure 37 shows micrographs at the 9 o'clock position of three samples with radial hydrides after RCT at (a) 20 °C, (b) 135 °C, and (c) 300 °C. In the samples tested at 20 and 135 °C (see Figure 37(a) and Figure 37(b)), the cracks start from radial hydrides on the outer surface of the cladding until they reach a circumferential hydride. Then, they propagate in circumferential direction until they reach another radial hydride, to propagate again in the direction towards the inner surface. In Figure 37(a), secondary cracks are marked by arrows. In case of the sample tested at 300 °C (see Figure 37(c)), there are no cracks and the hydrides are barely visible. It seems that they may have dissolved. This would explain why the load-displacement curves at 300 °C for samples subjected to RHT (i.e., with radial hydrides) are very similar to the ones of PT samples (with only circumferential hydrides), as shown in Figure 35.

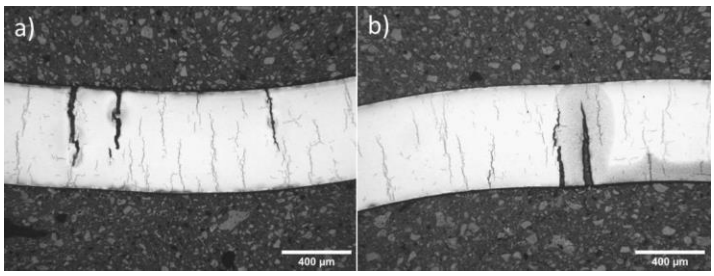

Figure 38 – Micrographs of RHT samples at 6 o'clock or 12 o'clock position after RCT at 20 °C (a) and 135 °C (b) showing multiple cracks

In other cases, multiple cracks are found in the same region, as shown in Figure 38, which corresponds to the 6 and 12 o'clock position of the samples tested at 20 and 135 °C. As in Figure 37, the cracks follow radial hydrides, but in this case they start at the inner cladding surface and grow towards the outer surface.

Some RCT were performed on samples using ceramic inserts as surrogate pellet at 20 °C. Figure 39 shows some representative load-displacement curves for PT and RHT samples with and without

ceramic inserts, the latter being limited to a maximum load of 5 kN. For samples with ceramic inserts, the load increases linearly with the displacement, whereby the slope is very steep. No load drops were observed in the RHT samples. In this case, the behaviour is completely dominated by the ceramic insert. Post examination of the samples showed no cracks in the cladding, even in the samples with radial hydrides.

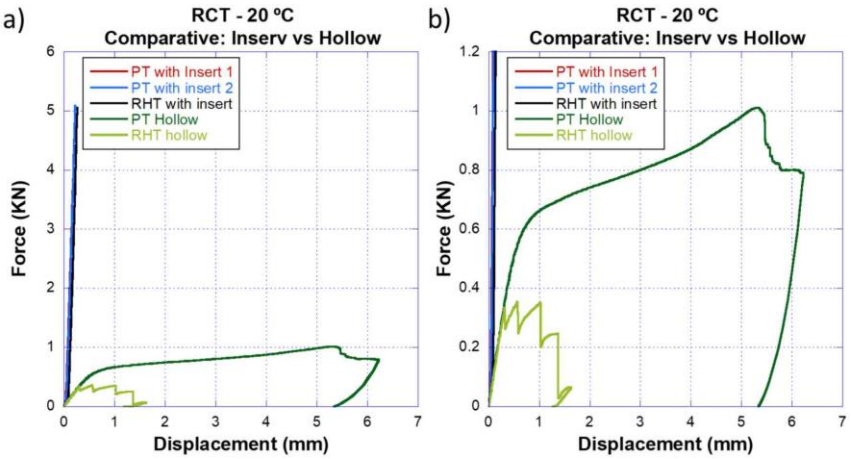

Figure 39 – Representative load-displacement curves from RCT for PT and RHT samples with and without ceramic inserts at 20 °C: general view (a) and detail with modified load scale (b)

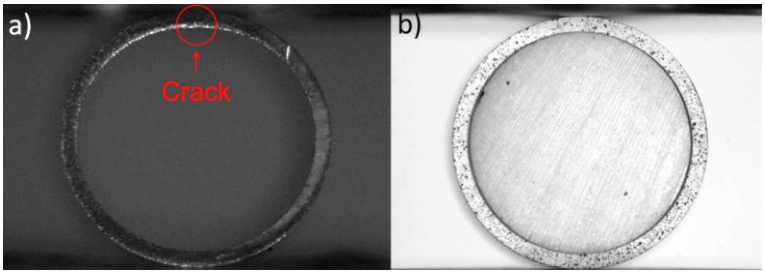

Figure 40 – Pictures of RHT samples during RCT at 20 °C: hollow (a) and with ceramic insert (b)

For comparison, Figure 40 shows two images of RHT samples (with radial hydrides) during RCT at 20 °C. Figure 40(a) corresponds to the moment when the first crack appears in the hollow sample (12 o'clock position, inner surface) for a load of 0.33 kN and a displacement of 0.32 mm. In Figure 40(b) (cladding sample with ceramic insert), the applied load is the same, while the displacement is only 0.1 mm, and no cracks are found in the cladding. This confirms the stiffening caused by the ceramic insert, which prevents cladding cracking by constraining its deformation.

3.4 Thermo-Mechanical Creep Test

3.4.1 Experimental Setup

In Hungary, the maximum permissible cladding temperature of the spent VVER-440 fuel during drying and dry storage is 400 °C [43]. At this temperature, the cladding may undergo thermal creep due to the internal pressure of the initial helium, the released fission gases and the helium resulting from alpha decay. The cladding tubes, which have undergone some corrosion during reactor operation, may contain dissolved hydrogen and precipitated hydrides. Therefore, it is important to quantify the effect of the hydrogen content on the creep properties.

During the creep tests at the Hungarian Centre for Energy Research (HUN-REN CER), pressurised cladding samples were placed in a tube furnace in inert atmosphere for extended periods of time. The inelastic deformation was observed at regular intervals by measuring the outer diameter of the samples. Some samples were pre-treated with hydrogen at high temperature to observe the effect of hydrides on the secondary creep rate.

Figure 41 – Three-zone tube furnace used at HUN-REN CER

A three-zone tube furnace was used for the creep tests that has a maximum operating temperature of 1200 °C (see Figure 41). The three zones make it possible to keep the 25-cm-long interior of the furnace at a constant temperature. The temperature profile of the tube furnace was measured with thermocouples placed at eight points. Various approaches were tested to describe the data collected on measured temperature, axial position of thermocouple and elapsed time with a formula. The best results were obtained by fitting a Gaussian curve, which returned a nearly parabolic profile near the edges of the furnace, while the central region of the furnace was deemed isothermal. The data from the 400 °C measurement showed that a difference of ±2 °C between the centre and the edges of the sample could occur with a 100-mm-long creep sample, which was considered acceptable. As the inner diameter of the furnace was 40 mm, only four samples could be tested simultaneously. The inside of the tube furnace could be evacuated and was filled with argon at the beginning of each test period.

A simple pressurisation system was built to keep the creep samples at a constant pressure (see Figure 42). Using a 20 MPa gas cylinder with 99.9999 % pure argon, a smaller buffer tank with a volume of 10 dm^3 was filled to a pressure of 11 MPa. A reducer with a 0.5 mm hole was used for the transfer between the two bottles. The pressure of the buffer tank was continuously recorded during the measurement using a pressure transmitter; the pressure could also be read from a Bourdon tube manometer during the test. Flexible capillaries with an internal diameter of 0.2 mm were welded to steel tubes and connected to the pressurisation system for each sample. The samples were attached to the steel tubes using quick connectors with Swagelok-type fittings and swivel-nuts. The four samples entered the furnace through sealed joints welded to the blind flange on the right side of the furnace. The central thermocouple of the furnace was introduced between the samples from the left side. While the samples could only be moved together with the blind flange, the length of the steel tubes that are pushed into the furnace could be adjusted using the extensions welded to the flange.

The diameter of the samples was measured using a laser scanner micrometer that continuously moved along the samples with the help of a stepper motor and a linear module. The laser micrometer was set to measure the diameter several times per second; the data was recorded using a data logger. This

required a precise linear movement system. For industrial use, for example, to move the tools of CNC machines, two types of modules are used: trapezoidal drive and belt drive. Among the linear modules available on the market, these two types can be expected to have a similar cost, but the trapezoidal movement enables more precise operation by up to an order of magnitude. Hence, the trapezoidal thread module was selected to increase the accuracy. The module chosen was an Igus SLW-1660 type linear module with a 1-metre stroke, driven by a trapezoidal thread with a thread pitch of 4 mm, and triple bracing that can be operated with an accuracy of 5 µm. The precision thread is driven by a NEMA 23 type stepper motor.

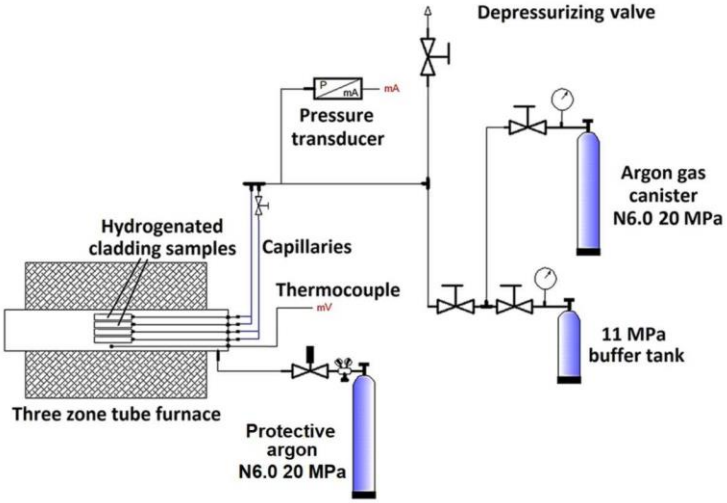

Figure 42 – Drawing of the pressurisation system built for creep tests

The motor control code was created using National Instruments LabView 2014. The motor was driven by the signals generated by the computer code through a Measurement Computing USB-2408 type A/D converter and data acquisition unit and through TB67S109 type microcontrollers. The motor was set to 400 steps per revolution using microsteps, so that each motor step corresponded to a displacement of 0.01 mm, which enabled an easy recording of 100 data points per 1 mm change in sample diameter. Using the interface of the control code built with LabView, the step time of the motor, the number of steps and the number of repetitions (in case of multiple measurements) can be set. By specifying the axial step length and the number of steps, the total length of all the samples is obtained in one scan. The number of measurements that the device performs can be set and the laser measuring head can move in both directions. The arrangement includes two additional stepper motors, one of them can rotate the samples, while the other moves a reference edge (a plate covering the lower half of the sample) that can be used to measure the bending of the samples. These two extra motors were not used in the present measurements.

The setup of the profilometer is shown in Figure 43. The measuring head of the laser micrometer was mounted on the linear module. The laser micrometer consists of two parts, the Mitutoyo LSM-503 type measuring head and an LSM-6200 type data processing unit to which it is connected. According to the settings used, the device performs 512 measurements in about 0.2 s with an error of ±0.1 µm according to the micrometer specification and then sends the average of this data through the USB port. The data is transferred directly to an Excel spreadsheet via USB. The motor control was performed by a personal computer and the data collection by a separate laptop.

Due to the design of the measuring head, the samples must be kept in the middle of the parallel laser beams, which is why they were attached to a sample holder parallel to the linear module and perpendicular to the laser. This sample holder was designed around the welded plugs on the samples.

The end plugs sit tightly in the sample holder to prevent the samples from rotating and to ensure that they are always measured in the same azimuthal position. After removal of the samples from the furnace, the hydraulic connectors were disassembled on the side of the steel tubes and the samples were removed from the pressurisation system together with the connectors.

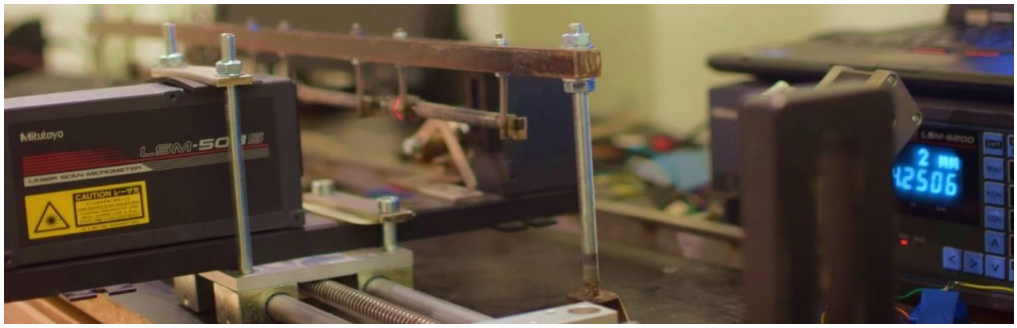

Figure 43 – Laser profilometry setup with measuring head of the laser micrometer mounted on the linear module (left), micrometer control unit and data acquisition laptop (right), and the cladding sample on the sample holder (middle)

During the measurement, the motor was stopped after the motor steps were completed; a trigger signal generated by the motor control code was sent to request data from the laser micrometer unit. This also meant that the sample remained stationary during the measurement with the laser micrometer. After it performed the diameter measurement and the averaging, it transmitted the data to the laptop via USB. Using an Excel VBA macro on the laptop, the exact time of the arrival of the data was recorded; this was necessary to track any potentially missing data, signalled by a discrepancy in time. One motor step, the measurement and one data transmission takes about 0.3 seconds, but the laptop could reliably record data only about every 0.6 seconds. With this in mind, the measurement cycle time was set to 670 ms. In other words, after starting the motor and transferring the data, the computer code that controls the measurement waited around half a second to ensure that the data arrived. The diameters of the samples were measured twice by moving the measuring head all the way to the left and then back to the right. It took about 22 hours to measure the four tested samples in both directions, and thus about one and a half days were needed for one measurement (depressurisation, cooling of the furnace, disassembly, laser micrometer measurement, reassembly, heating up and pressurisation).

3.4.2 Sample Material

The cladding samples tested were the Russian Zr1%Nb alloy E110 and its successor the E110opt based on sponge base material [44]. The measurement of thermo-mechanical creep caused by internal pressure was carried out using welded samples produced from 100-mm-long industrial cladding tubes. The outer diameter of the tubes was 9.1 mm with a wall thickness around 0.67 mm. A zirconium plug was welded to one end of the tubes and a zirconium connector was welded to the other end to enable connection with hydraulic quick connectors. As a result of the welding, the ends of the samples were blackened and oxidised in a section of about 10 mm, and a rainbow-coloured transition could initially be observed at the edges of the intact cladding sections (see Figure 44 and Figure 45). This variably coloured zirconium oxide appears when the layer thickness is less than 1 µm. Small markings with a depth of 0.05 mm were placed on the surface of the samples every 10 mm to facilitate positioning of the samples and also served as reference points.

3.4.3 Sample Preparation

For the hydrogenation of E110 and E110opt cladding samples, a three-zone tube furnace with a calibrated volume gas inlet system and a vacuum system was assembled according to Figure 46. Before

starting the measurement, the samples were degreased with an organic solvent (acetone) and then air-dried. The weight of the samples before and after hydrogenation was measured on a Sartorius SE2 electronic ultra-microbalance.

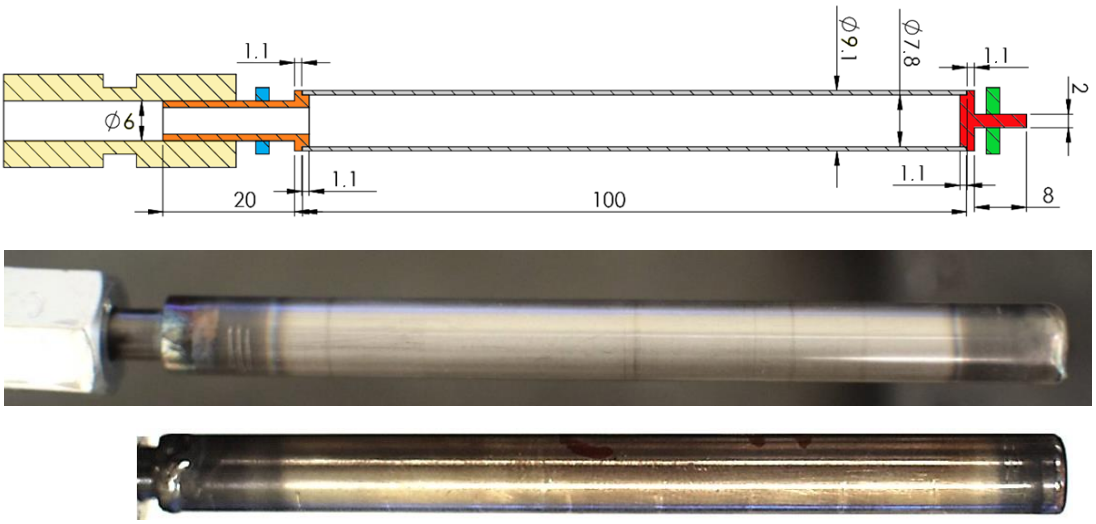

Figure 44 – Drawing of the parts of the tested samples (top), picture of a welded as-received sample (middle), and picture of a hydrogenated sample (bottom)

Figure 45 – Samples connected to the pressurisation system entering the tube furnace

One sample at a time was placed on the quartz glass sample holder with a soft iron core. The sample together with the sample holder was first placed in the end of the quartz tube outside the furnace area and the apparatus was sealed. After evacuation, the system was filled with high-purity (99.9999 %) hydrogen to the calculated initial pressure, and then the system pressure was topped up to atmospheric pressure with high-purity (99.9999 %) argon. The quartz glass sample holder with a soft iron core was pushed together with the sample into the preheated 600 °C furnace with the help of a strong magnet on the outside. Then, at the end of the hydrogenation, the sample was pulled back into the cold part of the quartz tube. The pressure corresponding to the total volume (hydrogen plus argon) was continuously measured. The process of hydrogen absorption was indicated by a decrease in pressure. The time and the approximate quantity of hydrogen required to charge the cladding samples with 1000 wppm hydrogen was established based on previously conducted tests. After 3 hours, the pressure did not decrease any further and the hydrogen content of the samples reached equilibrium with the hydrogen in the gas space.

Filling with hydrogen was carried out at a high temperature, during which the cladding samples were also subjected to heat treatment. To assess the effect of this heat treatment on the creep and to separate it from the effect of the hydrogen, one E110 and one E110opt sample was heat treated in high-purity argon at 600 °C for the same period of time, and their creep was examined under the same conditions as the hydrogenated samples.

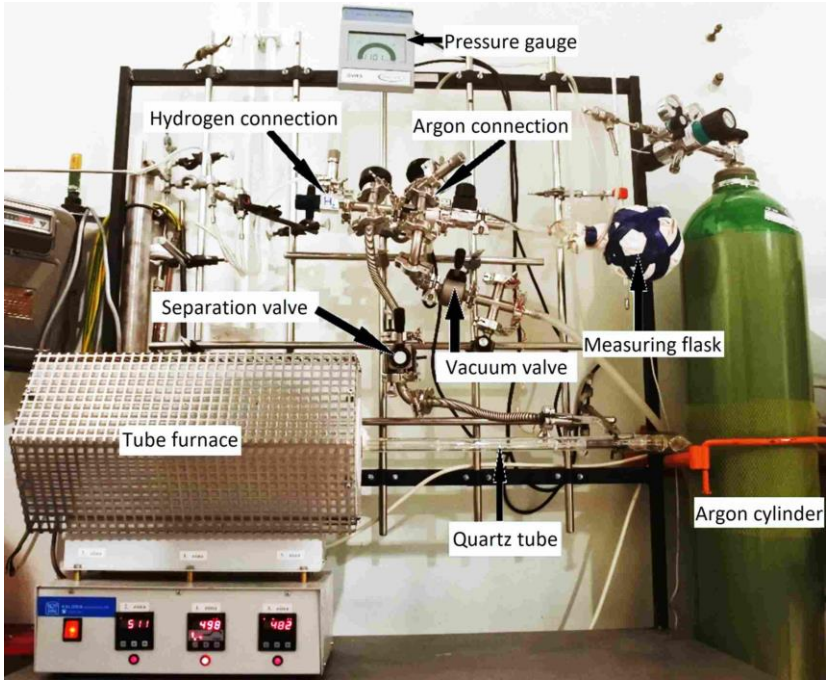

Figure 46 – Setup used to charge the cladding samples with hydrogen

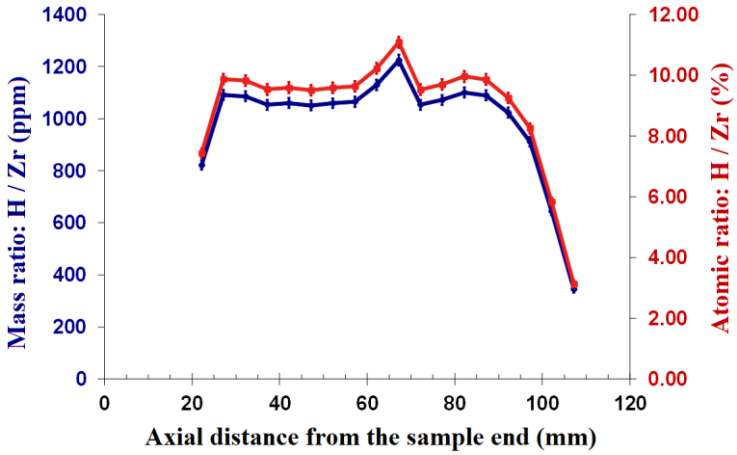

Figure 47 – Distribution of the hydrogen content of the E110opt sample depending on the distance from the welded connector

The surface of the welded zirconium samples changed slightly as a result of the hydrogenation and the heat treatments. The oxide created during welding diffused into the metal. This is indicated by the disappearance of the rainbow-coloured transition layer and the slight brownish discolouration of the surface of the samples, as it can be seen in Figure 44.

To determine the distribution of hydrogen, the composition of the samples was checked using prompt-gamma activation mapping. Prompt-gamma activation analysis (PGAA) is a non-destructive nuclear analytical method that can be used to determine the average elemental and isotopic composition of the irradiated sample volume. During the measurement, the sample is irradiated with slow neutrons and the composition of the sample is deduced based on the analysis of the resulting gamma radiation. The high penetration of neutrons and gamma radiation also enables the examination of extensive samples. The advantage of the prompt-gamma activation analysis is that, among the light elements, the hydrogen important for the present study can be measured with good sensitivity in the given matrix, since the ratio of the H and Zr neutron capture cross-section (H: 0.3326 barn; Zr: 0.185 barn) is favourable. During the measurements, the change in the atomic ratio of hydrogen to zirconium was measured along the longitudinal axis of the two hydrogenated cladding samples.

The measurements were carried out at the NIPS-NORMA measuring site operated by HUN-REN CER, which is located at the end of neutron guide no. 1 connected to the cold neutron source of the Budapest Research Reactor. A scintillation screen converts the neutrons passing through the object into visible light (projection image), which is digitised with a camera using a very sensitive CCD chip. The achieved spatial resolution is approximately 500 µm. The size of the image field is approximately 40×40 mm^2; an image of larger objects can be created from a series of partially overlapping images. Gamma photons were detected with an n-type coaxial HPGe spectrometer equipped with lead protection. To narrow the neutron beam, a horizontally placed collimator made of Li polymer with 2×20 mm^2 openings was used. A total of 18 gamma spectra were recorded along the examined length of 85 mm with a step interval of 5 mm. The measurement time of each spectrum was 5 hours.

The prompt-gamma activation analysis method provides the most accurate results when determining the relative amount of elements, as many factors that play a role in the calculation of absolute quantities are eliminated. In the calculations, the area of the most intense peak of the elements was used: the 2223 keV peak for H, and the 935 keV peak for Zr. The counting rate calculated from the peak areas was corrected with the spectral background of the system and the change of the neutron flux over time. The energy of the gamma lines produced during irradiation is high enough to consider the gamma shading factor as constant.

As can be seen in Figure 47, the hydrogen was not evenly distributed in the samples, which could be expected. During the high-temperature welding, a thin oxide layer formed on the surface of the zirconium sample, which reduced the diffusion rate of hydrogen by several orders of magnitude, preventing the absorption of hydrogen. This is beneficial from a measurement point of view, as the welded joints were the parts to be exposed to high mechanical stress, but hydrogen can embrittle the welds, which can lead to cracks and leaks. However, only the middle part of the samples, which is interesting from a measurement point of view, absorbed hydrogen, namely an average of 1100 wppm for both samples. During testing at a temperature of 400 °C, the probability of the hydrogen absorbed in the samples diffusing out of the alloy is low, but the spatial distribution of the hydrogen may change.

3.4.4 Measurement Campaigns

Two sets of tests were conducted with four samples each. The test matrix is shown in Table 6. In the first series, only as-received samples were tested, two E110 and two E110opt. Two samples were exposed to an internal pressure of 11 MPa at a constant temperature of 400 °C in inert gas atmosphere. The chosen internal pressure results in a hoop stress of 65 MPa in the cladding, which is 66 % of the yield strength at 400 °C ($\sigma_{y\ 400°C}$ = 98 MPa) [45]. The maximum allowable internal pressure in the rods during dry storage is 10 MPa; the chosen measurement conditions exceed this limit by 10 %. The expected actual internal pressure during interim storage (without vacuum drying) is around a third of this value.

Table 6 – Test matrix of the creep tests

Sample no.	Material	Pre-treatment	Treatment temperature (°C)	Pressurisation (MPa)	Test temperature (°C)
1	E110	none	n/a	0.1	400
2	E110	none	n/a	11	400
3	E110opt	none	n/a	0.1	400
4	E110opt	none	n/a	11	400
5	E110	hydrogenated	600	11	400
6	E110	heat-treated	600	11	400
7	E110opt	hydrogenated	600	11	400
8	E110opt	heat-treated	600	11	400

As the furnace was not completely air-tight, some air or water could enter it during the test, so some oxidation of the samples was expected. The change in the outer diameter due to the formation of the surface oxide layer could be measured because the other two cladding samples remained under atmospheric pressure when they were placed in the furnace under the same conditions. The difference in the average diameter change between the pressurised and the atmospheric samples was proportional to the deformation due to the creep.

In the second series, the two hydrogenated samples and the two heat-treated samples were both pressurised to 11 MPa and tested at 400 °C. To detect the effect of hydrogen, instead of the 400 wppm allowed in normal operation, an absorbed amount of hydrogen of 1000 wppm was decided. This value is higher than the expected hydrogen content absorbed by the cladding during normal operation, however, it has been possible to deduce from this measurement whether the hydrogen has a significant influence on creep. Since the solubility limit for hydrogen is about 200 wppm at 400 °C [46], most of the hydrides form precipitates at the test temperature.

3.4.5 Main Results

The creep test was conducted in two series: the as-received samples were measured over 53.2 effective days, while the pre-treated samples were measured over 97.5 effective days. The effective measurement time was the time the samples spent at temperatures above 360 °C and pressure above 10 MPa. This was determined based on the logged data. The oxidation of the outer surface of the samples was also taken into account. The corrected diameter increase was plotted against the time, and the secondary (steady-state) creep rates were calculated for each sample.

Figure 48 – Picture of the four measured samples with the hydraulic connectors attached at the end of the first test series

Oxidation was not uniform in the samples of the first series (see Figure 48). The part of the samples closer to the hydraulic connector was more heavily oxidised, while on the other side only black, continuous oxide was visible until the end of the test. This less oxidised section provided an opportunity to compare the measurements. Based on the measurement of as-received samples under atmospheric internal pressure, the oxide layer on the E110 samples reached a thickness of 10 µm by the end of the test, while on the E110opt samples it was about 1 µm and this did not increase further after the first few effective days. The effect of creep could be clearly separated from this increase in diameter.

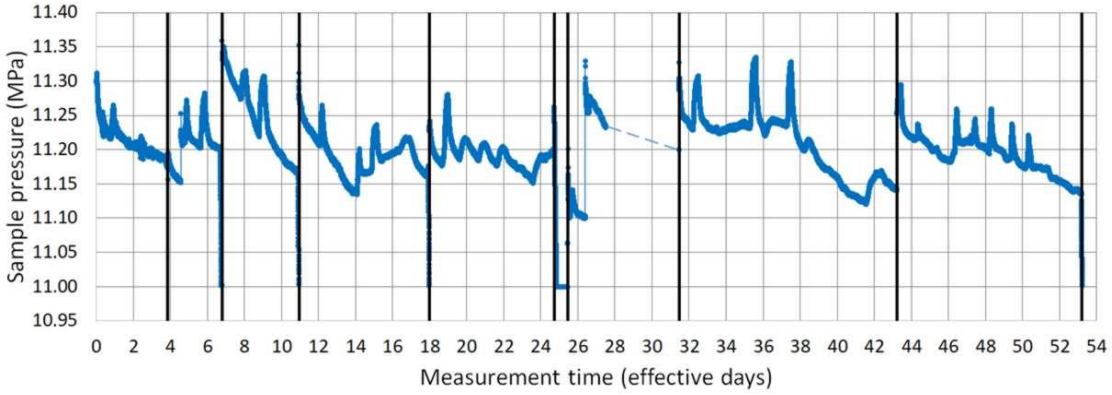

Figure 49 – Pressure history of the first series of measurements

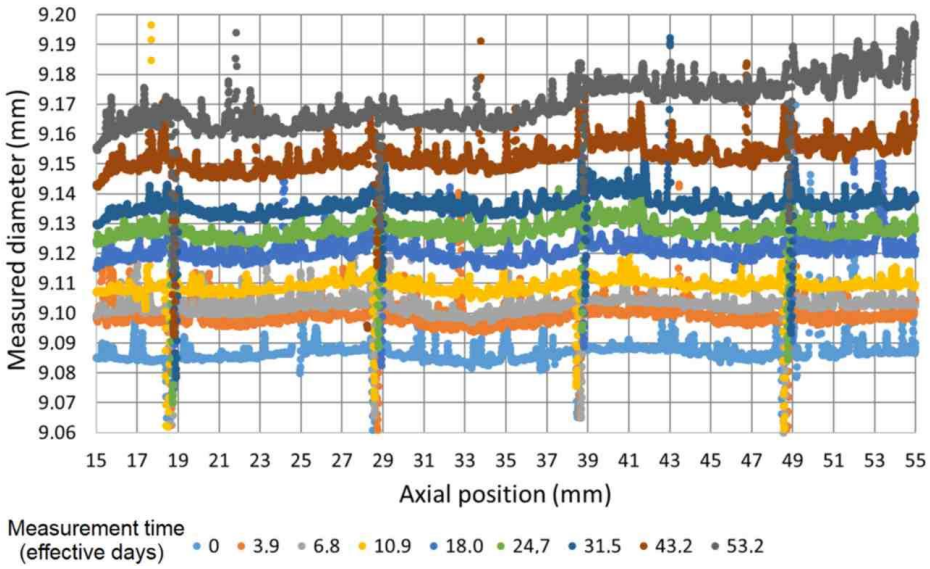

Figure 50 – Measured outer diameter of the as-received E110opt sample no. 4 during the test

The pressure history of the first series of measurements is shown in Figure 49. Black lines indicate the times of disassembly and profilometry. The average pressure in the samples was 11.2 MPa and was maintained with an accuracy of about ±0.1 MPa during the 53.2 effective days in which the diameter change of the samples was measured 8 times. After 25.4 effective days, the test was briefly interrupted without the furnace being stopped to eliminate a leak. There was a longer power outage after 27.5 days (possibly a few hours), with the pressure measurement failing when the battery of the uninterruptible power supply and then that of the laptop was discharged. The test was continued without logging the pressure when the furnace turned on again after the power supply was restored. The pressure did not significantly decrease during these unrecorded days.

Table 7 – Corrected average diameter increase of the as-received cladding samples in the first test series

Time (effective days)	Corrected average diameter increase (µm)	
	E110	E110opt
3.9	21.4	13.1
6.8	24.2	16.0
10.9	27.8	22.6
18.0	33.3	34.1
24.7	37.6	41.4
31.5	44.8	49.9
43.2	54.8	65.7
53.2	66.1	80.1

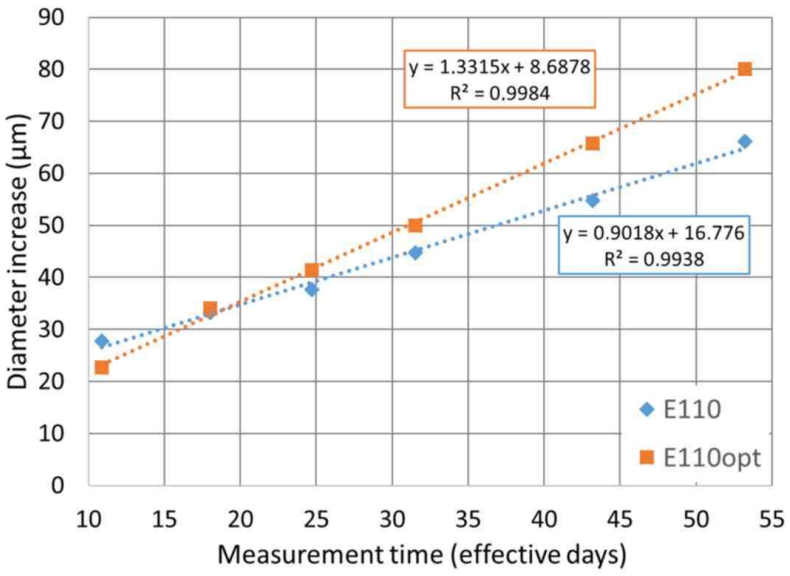

Figure 51 – Corrected average diameter increase of the samples during the first series of creep tests

The evolution of the diameter of the pressurised E110opt sample no. 4 can be seen in Figure 50. The sudden decreases in diameter represent the positions of the surface markings. The diameter change of the samples with high internal pressure was reduced by the diameter change of the samples with atmospheric internal pressure, which came only from surface oxidation. The corrected average diameter increase of the as-received cladding samples in the first test series (relative to the original diameter) is given in Table 7. The start of the secondary creep phase was determined at 10.9 effective measurement days. By plotting the corrected diameter increase, the slope of the fitted line results in the secondary creep rate (see Figure 51). The two types of cladding had different creep rates. In case of E110 (sample no. 2), the corrected diameter change was 0.9 µm/day, and for E110opt (sample no. 4) it was 1.33 µm/day.

In the second experimental series, the creep was measured over 97.5 effective days, whereby the diameter change of the samples was measured 11 times. The oxidation of the samples was stopped by repeatedly evacuating the inside of the furnace and filling it with a slight overpressure of argon. The thin, less than 1 µm thick oxide layer that was created during the pre-treatments also helped to slow down oxidation, as this oxide layer covering the metal surface prevents (or at least slows down) further oxidation. Figure 52 shows the surface of the samples, which is covered by a compact, black oxide layer at the end of the measurement. The number of the sample can be recognised on the left-hand side on the swivel nuts with which the samples were fastened to the hydraulic connectors.

Figure 52 – Picture of the four measured samples at the end of the second test series

The internal pressure of 11 MPa specified in the test matrix was maintained with an accuracy of a few percent during the measurement (see Figure 53, black lines indicate the times of disassembly and profilometry); the average value was 11.15 MPa. During the test, a fluctuation in the set pressure of 0.1 MPa was detected, which was due to the heating of the test hall. An increase in the hall temperature by 3 °C (due to the heating of the neighbouring offices) led to a pressure increase of 1 %, which was ultimately neglected.

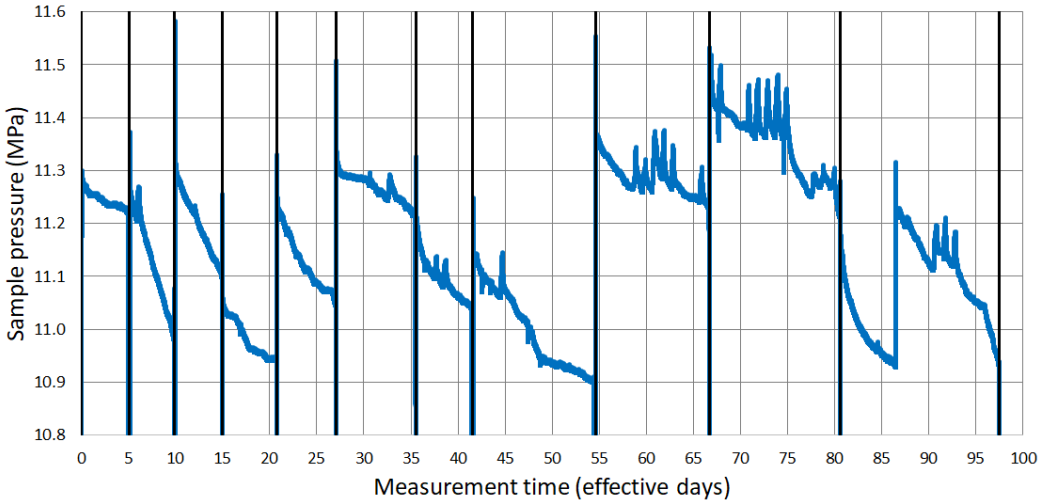

Figure 53 – Pressure history of the second series of measurements

Figure 54 shows the diameter change of the hydrogenated E110opt sample no. 7 in the course of the test. The sudden decreases in diameter represent the positions of the surface markings and the welds at the ends. In the first 10 to 15 days during the fast primary creep stage, the equilibrium shape of the sample developed and a thin, compact black oxide layer was formed. Thereafter, the diameter of the

samples changed almost linearly depending on the effective days. The start of the secondary creep phase was determined at 14.9 effective measurement days. The corrected average diameter increase of the pre-treated cladding samples in the second test series (relative to the original diameter) is given in Table 8. The linear regression gives the secondary creep rates, which were almost the same for the two hydrogenated samples, while the heat-treated samples showed some differences (see Figure 55).

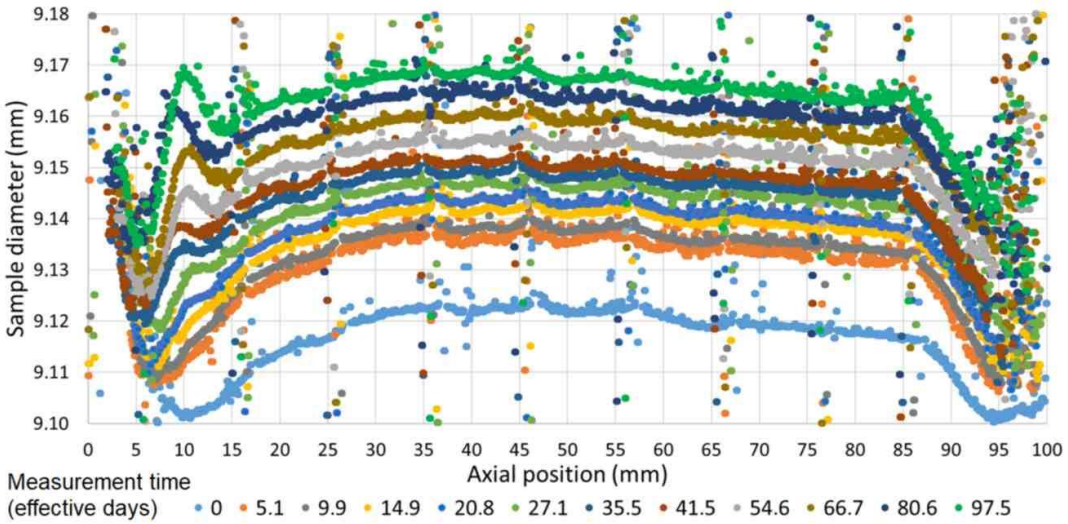

Figure 54 – Measured outer diameter of the hydrogenated E110opt sample no. 4 during the test

Table 8 – Corrected average diameter increase of the pre-treated cladding samples in the second test series

Time (effective days)	Corrected average diameter increase (µm)			
	E110 hydrogenated	E110 heat-treated	E110opt hydrogenated	E110opt heat-treated
5.1	14.8	14.2	14.4	8.9
9.9	15.5	13.1	15.6	11.4
14.9	17.9	17.2	18.3	15.8
20.8	20.4	20.1	20.9	20.7
27.1	23.1	25.8	24.2	25.6
35.5	25.5	30.0	26.2	30.1
41.5	27.5	33.4	28.2	34.6
54.6	31.7	44.3	32.0	44.3
66.7	35.6	53.5	37.1	54.5
80.6	39.9	60.9	41.4	65.1
97.5	43.7	69.8	45.3	76.8

The final results in terms of the calculated secondary (steady-state) creep rates are shown in Table 9. The two tested as-received samples had different secondary creep rates. Although the manufacturing process appears to be the same, the changes in the base material and chemical composition [44] may have resulted in a slightly different grain size and microstructure, which affects the creep rate.

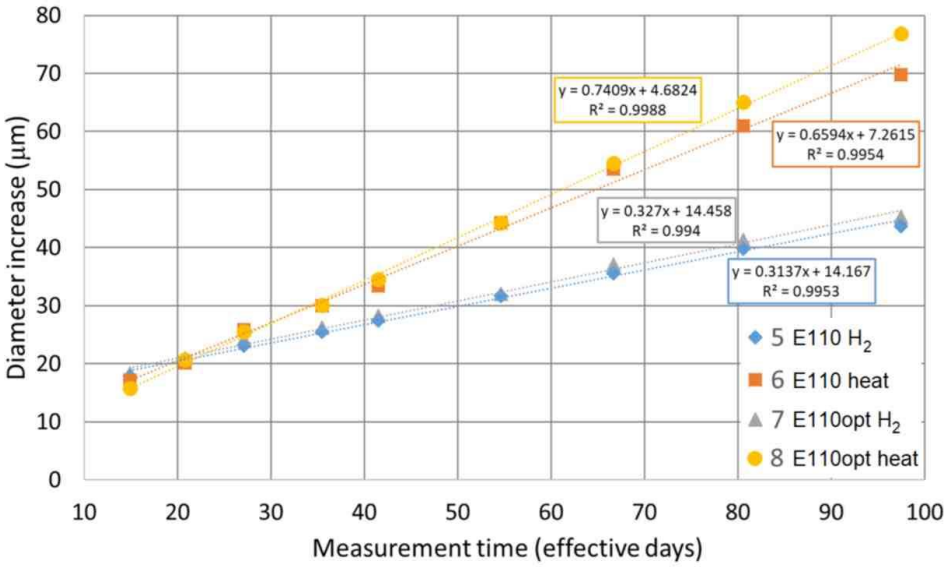

Figure 55 – Corrected average diameter increase of the samples during the second series of creep tests

Table 9 – Calculated secondary (steady-state) creep rates

Material	Treatment	Pre-treatment temperature (°C)	Secondary creep rate (% outer diameter change/day)	Secondary creep rate (µm outer diameter change/day)
E110	none	n/a	0.00991	0.902
E110	heat-treated	600	0.00725	0.659
E110	hydrogenated	600	0.00345	0.314
E110opt	none	n/a	0.01463	1.331
E110opt	heat-treated	600	0.00814	0.741
E110opt	hydrogenated	600	0.00359	0.327

Based on the results, due to the high hydrogen content used in this test, precipitation hardening of the zirconium hydrides in the alloy significantly reduces the creep rate, as it strengthens the material and inhibits the dislocation sliding. This is in line with previous tests conducted using different cladding materials [46]. The heat treatment under inert gas also had a significant effect, as it may have partially recrystallized the stress-relieved annealed cladding samples, which also has an effect on the creep rates.

3.5 Neutron Radiography

3.5.1 Experimental Setup

Neutron radiography is a non-destructive method, which can be used to visualise hydrogen in zirconium based cladding rods. Neutrons, emerging from a neutron source, can be transmitted through relatively thick sample material. While the scattering cross section of zirconium for neutrons is very low, it is relatively high for hydrogen. In this respect, hydrogen and its compounds can be well detected in the claddings. Figure 56 shows a comparison of the attenuation coefficients for X-rays and thermal neutrons by chemical elements [47]. The attenuation of zirconium and hydrogen in the case of neutrons is practically just the other way around compared to that for X-rays. In this respect, neutrons are specifically suitable to radiograph metals.

Attenuation coefficients for thermal neutrons [cm^{-1}]

1a	2a	3b	4b	5b	6b	7b	8			1b	2b	3a	4a	5a	6a	7a	0
H																	He
3.44																	0.02
Li	Be											B	C	N	O	F	Ne
3.30	0.79											101.60	0.56	0.43	0.17	0.20	0.10
Na	Mg											Al	Si	P	S	Cl	Ar
0.09	0.15											0.10	0.11	0.12	0.06	1.33	0.03
K	Ca	Sc	Ti	V	Cr	Mn	Fe	Co	Ni	Cu	Zn	Ga	Ge	As	Se	Br	Kr
0.06	0.08	2.00	0.60	0.72	0.54	1.21	1.19	3.92	2.05	1.07	0.35	0.49	0.47	0.67	0.73	0.24	0.61
Rb	Sr	Y	Zr	Nb	Mo	Tc	Ru	Rh	Pd	Ag	Cd	In	Sn	Sb	Te	I	Xe
0.08	0.14	0.27	0.29	0.40	0.52	1.76	0.58	10.88	0.78	4.04	115.11	7.58	0.21	0.30	0.25	0.23	0.43
Cs	Ba	La	Hf	Ta	W	Re	Os	Ir	Pt	Au	Hg	Tl	Pb	Bi	Po	At	Rn
0.29	0.07	0.52	4.99	1.49	1.47	6.85	2.24	30.46	1.46	6.23	16.21	0.47	0.38	0.27			
Fr	Ra	Ac	Rf	Ha													
	0.34																

	Ce	Pr	Nd	Pm	Sm	Eu	Gd	Tb	Dy	Ho	Er	Tm	Yb	Lu
*Lanthanides	0.14	0.41	1.87	5.72	171.47	94.58	1479.04	0.93	32.42	2.25	5.48	3.53	1.40	2.75
	Th	Pa	U	Np	Pu	Am	Cm	Bk	Cf	Es	Fm	Md	No	Lr
**Actinides	0.59	8.46	0.82	9.80	50.20	2.86								

Attenuation coefficients for X-ray [cm^{-1}] (150kV)

1a	2a	3b	4b	5b	6b	7b	8			1b	2b	3a	4a	5a	6a	7a	0
H																	He
0.02																	0.02
Li	Be											B	C	N	O	F	Ne
0.06	0.22											0.28	0.27	0.11	0.16	0.14	0.17
Na	Mg											Al	Si	P	S	Cl	Ar
0.13	0.24											0.38	0.33	0.25	0.30	0.23	0.20
K	Ca	Sc	Ti	V	Cr	Mn	Fe	Co	Ni	Cu	Zn	Ga	Ge	As	Se	Br	Kr
0.14	0.26	0.48	0.73	1.04	1.29	1.32	1.57	1.78	1.96	1.97	1.64	1.42	1.33	1.50	1.23	0.90	0.73
Rb	Sr	Y	Zr	Nb	Mo	Tc	Ru	Rh	Pd	Ag	Cd	In	Sn	Sb	Te	I	Xe
0.47	0.86	1.61	2.47	3.43	4.29	5.06	5.71	6.08	6.13	5.67	4.84	4.31	3.98	4.28	4.06	3.45	2.53
Cs	Ba	La	Hf	Ta	W	Re	Os	Ir	Pt	Au	Hg	Tl	Pb	Bi	Po	At	Rn
1.42	2.73	5.04	19.70	25.47	30.49	34.47	37.92	39.01	38.61	35.94	25.88	23.23	22.81	20.28	20.22		9.77
Fr	Ra	Ac	Rf	Ha													
	11.80	24.47															

	Ce	Pr	Nd	Pm	Sm	Eu	Gd	Tb	Dy	Ho	Er	Tm	Yb	Lu
*Lanthanides	5.79	6.23	6.46	7.33	7.68	5.66	8.69	9.46	10.17	10.91	11.70	12.49	9.32	14.07
	Th	Pa	U	Np	Pu	Am	Cm	Bk	Vf	Es	Fm	Md	No	Lr
**Actinides	28.95	39.65	49.08											

Figure 56 – Comparison of the linear attenuation coefficients for thermal neutrons (top) to 150 kV X-ray (bottom)

The investigations were carried out at the Paul Scherrer Institute (PSI) in Switzerland. The PSI neutron source is a spallation source. The neutrons are slowed down by a moderator to thermal energies, which can vary depending on the exact conditions of respective beam lines to which the neutrons are guided. The tests are done in transmission mode. Depending on the amount of hydrogen in a sample, a respective hydrogen distribution is projected two-dimensionally on a detector and evaluated. With the created neutron image and respective calibration, hydrogen concentrations from about ten wppm up to a few thousand wppm can be differentiated. When using the neutron microscope, the concentration distribution can be spatially resolved with an accuracy of less than 10 µm.

In practice, the samples are put in the neutron beam in front of the detector. In case of radioactive, irradiated claddings, the defueled samples are encapsulated in an aluminium box for the transfer to the beamline, for handling and for guaranteeing that no contamination occurs (see Figure 57).

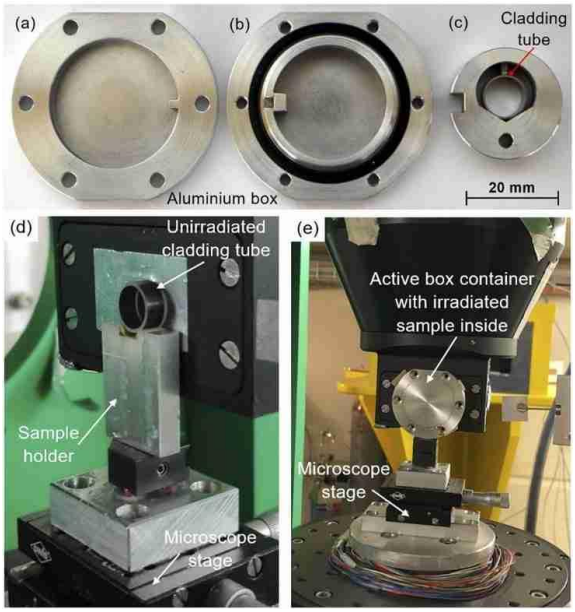

Figure 57 – Aluminium box for radioactive cladding samples for neutron imaging: box backside (a), front side (b), and inside sample holder (c); Neutron microscope stage with an inactive sample in front of the detector (d) and with the box for irradiated samples (e)

(Taken from Trtik et al. [48])

To obtain meaningful neutron radiographs, a process of image corrections is followed. Lateral inhomogeneities of the beam and detector sensitivity need to be levelled out, so that they are not erroneously attributed to possible sample properties. Further, back-scattering effects of the detector itself need to be taken into consideration.

3.5.2 Sample Material

Basically, zirconium based cladding material is used. The samples are cut perpendicularly to the axial direction, and ring-shaped sections of length of 4 to 5 mm are created. The axial direction of the rings will later be oriented parallel to the neutron beam. The axial length is an optimisation between neutron attenuation of the cladding material and the hydrogen content. In fact, for a shorter sample, the metal would less attenuate the neutrons, but, with typical hydrogen concentrations of interest, the attenuation by the hydrogen becomes insufficient. A too large sample would lead to a too strong attenuation.

In case of cladding stemming from irradiated fuel rods, the cladding is defueled. This is necessary to allow thermo-mechanical testing with the existing test setup in PSI's hot-lab, and to reduce the activity and the risk of contamination with fission products. Nonetheless, the samples remain highly radioactive. They need to be handled in a way that no contamination can occur. To this end, these samples are encapsulated in a small sealed aluminium box.

The investigated samples – if irradiated – stem from fuel rods, which were in operation in a Swiss boiling water reactor (BWR) or pressurised water reactor (PWR). Unirradiated samples are of the same material type. Unirradiated cladding can be hydrogen loaded in-house with a Sieverts type apparatus.

Of specific interest are claddings that have a so-called liner. This liner has a thickness of several ten micrometres, consists of a purer zirconium alloy compared to the substrate, and is produced by co-

extrusion. The liner was introduced either as outer cladding layer for PWRs to improve the corrosion resistance, or as inner layer for the use in BWRs to mitigate pellet-cladding interaction. Interestingly, hydrogen strongly diffuses towards the liner, which can very well be seen by neutron radiography.

Sample material that undergoes a thermo-mechanical treatment shows a changed hydride morphology: first, hydrides dissolve, then the hydrogen diffuses along temperature or stress gradients or towards the liner, and re-precipitation occurs depending on a possibly existent stress field. The inhomogeneous hydrogen/hydrides concentration can very well be shown and analysed with neutron imaging.

The irradiated materials that have been used for testing are:

- Zircaloy-4 rod, cladding without liner, five cycles, average rod burnup of 58.8 GWd/t_{HM}, approximate H concentration 290 wppm
- Zircaloy-4 rod, cladding with outer liner, five cycles, average rod burnup of 72 GWd/t_{HM}, approximate H concentration 400 wppm
- Zircaloy-2 rods, claddings with inner liner, seven cycles, average burnup of the rods about 60 to 65 GWd/t_{HM}, H concentration about 120 to 150 wppm, or 250 to 300 wppm

3.5.3 Sample Preparation

The irradiated cladding sections were handled in PSI's hot laboratory. They were defueled and cleaned before cutting. Sections of a length of 4 to 5 mm were cut. The samples were radiographed in their as-received condition or after a thermo-mechanical treatment. The radioactive samples were encapsulated in the respective small boxes, which were transported to the beam line for imaging.

Unirradiated claddings were hydrogen loaded to concentrations comparable to those of the irradiated claddings. The loading was performed in a Sieverts type apparatus, which is a gaseous loading. Typical lengths of cladding pieces that can be hydrogenated are around 10 cm. Then, sections were cut to obtain rings with an axial length of 4 to 5 mm. Similar to irradiated cladding samples, thermo-mechanical testing was possible to be performed before neutron imaging. The general handling of unirradiated samples does not necessitate any specific precautions compared to the irradiated samples.

The integral hydrogen concentration was determined by destructive hot gas extraction, for both, the irradiated and unirradiated cladding. Either smaller samples, adjacent to those foreseen for neutron imaging, were used, or the neutron imaging sample itself could be used after imaging.

3.5.4 Measurement Campaigns

Several measurement campaigns have been performed in the past years. The campaigns are assigned based on a proposal system. Especially the measurement of radioactive samples needs a good coordination between the research group, the PSI hot laboratory, the colleagues from the spallation neutron source and the radiation protection officers.

In case of thermo-mechanical testing, the timely coordination of periods of testing in the hot-lab, making samples ready for neutron radiography, transfer and measurements is crucial.

3.5.5 Main Results

The goal of the tests has been to identify radially and circumferentially inhomogeneous hydrogen/hydrides concentration distributions in cladding that has undergone thermo-mechanical testing. The accumulation of hydrogen can increase the risk of local integrity failure. The hydrogen/hydrides distribution has been visualised and subsequently quantified by neutron radiography. Mechanical testing and the influence of the hydrides distribution and morphology have not been part of the work.

The results part is split into the topics: I) hydrogen diffusion to the liner, II) hydrogen diffusion to the liner under stress, III) delayed hydride cracking in presence of an inner liner, IV) inner oxide, V) influence of ring compression creep on hydrogen distribution, and VI) concluding remarks.

I) Hydrogen diffusion to the liner

In standard post-irradiation light optical microscopy examinations of spent fuel rods, it turned out that the liner of claddings attracts hydrogen. While the motivation to apply an inner or outer liner originally had a different purpose, the accumulation of hydrides can be considered as positive, as most of the cladding will be hydrides free and thus less prone for embrittlement. PSI had performed already earlier respective tests that showed the increasing accumulation of hydrides in an outer liner when the cooling rate was decreased [49, 50]. In the following, the hydrogen diffusion into an inner liner could be shown as well (see Figure 58).

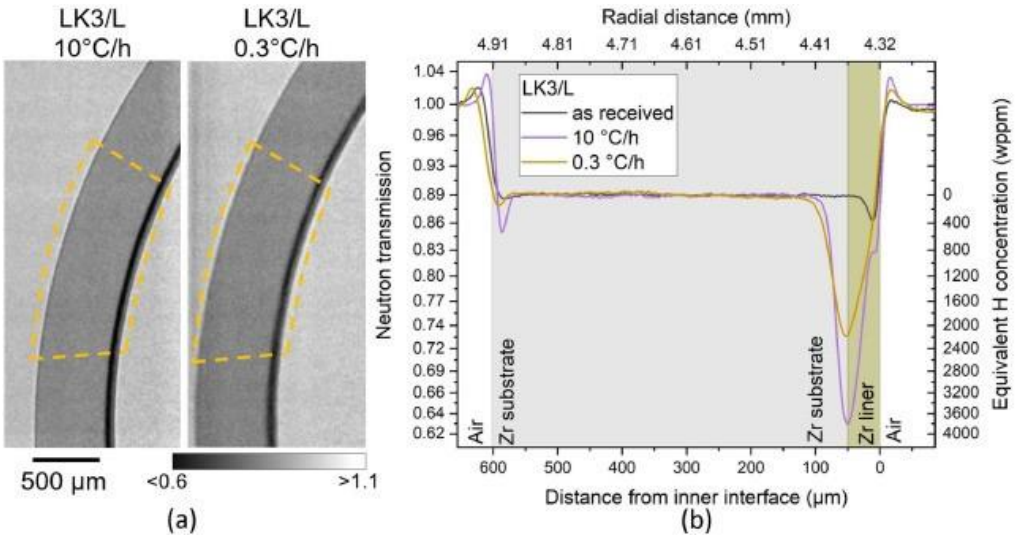

Figure 58 – Neutron radiographies of an unirradiated Zircaloy-2 cladding with inner liner (LK3/L) cooled at 10 °C/h and 0.3 °C/h at nominal hydrogen concentration of 200 wppm (a), and radial neutron transmission profiles and corresponding hydrogen distribution (b)

(Taken from Duarte et al. [51])

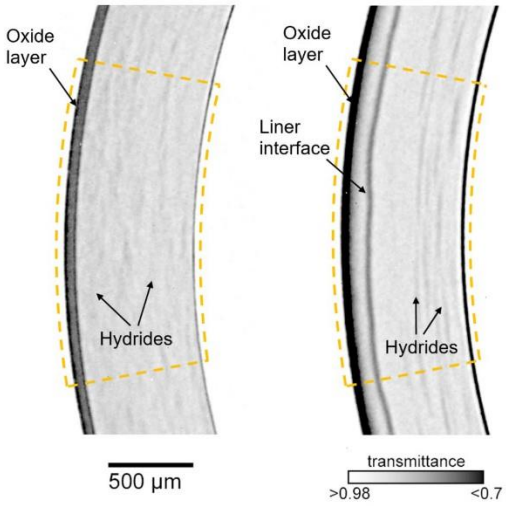

Cladding	Zry-4	Zry-4 DX-D4
Liner	none	outer
H_{total} (wppm)	362	441
BU (GWd/t_{HM})	60	70

Figure 59 – Neutron imaging of irradiated claddings with corresponding burnup (BU) and hydrogen concentration for Zry-4 type samples

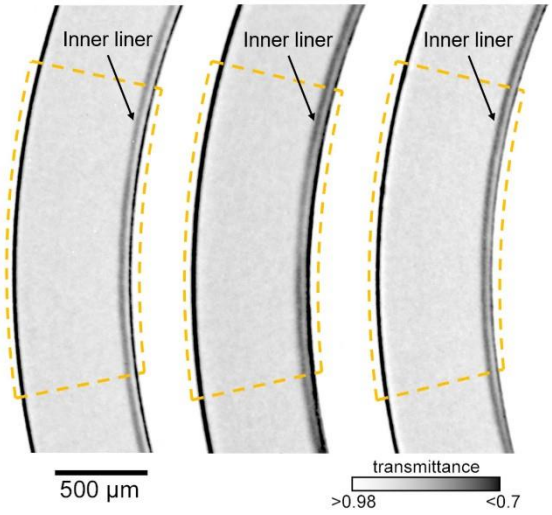

Cladding	Zry-2 *)	Zry-2 **)	Zry-2 *)
Liner	inner	inner	inner
H_{total} (wppm)	251	297	241
BU (GWd/t_{HM})	66	61	63.6

*) and **) samples with thermo-mechanical treatment, 1 cycle and 3 cycles, respectively, according to [52]

Figure 60 – Neutron imaging of irradiated claddings with corresponding burnup (BU) and hydrogen concentration for Zry-2 type samples

As can be seen from Figure 58, the hydrogen concentration in the inner liner is very high, i.e., there is a low neutron transmission. A determination of the local concentration is practically not possible with standard methods like metallography. The strength of the neutron radiography is that it enables quantification. It becomes clear that with sufficiently slow cooling practically all the hydrogen precipitates in the liner, close to the liner-substrate interface. Given the very slow cooling under dry storage conditions, the same effect can be expected, i.e., the hydrogen will be in the liner.

Comparable investigations have been performed on irradiated cladding, whereas thermo-mechanical treatments have not yet been performed on all the listed samples (see Figure 59 and Figure 60). Thus, the Zry-4 cladding sections were neutron imaged as-received, i.e., after the slow cooling during storage at the power plant before being transported to PSI, and then stored at PSI's hot-lab under ambient temperature.

II) Hydrogen diffusion to the liner under the influence of stress

Hydrogen diffuses along a stress gradient [53, 54]. Hydrogen precipitation under stress can lead to reoriented hydrides. The question arises to what extent a slow cooling in conjunction with a stress has influence on the distribution of the hydrides. For this purpose, reorientation tests of hydrides [55] in outer liner cladding have been analysed with neutron radiography and metallography.

Figure 61(a) shows neutron radiographs of claddings with approximately 200 wppm hydrogen with outer liner: (on the left) neutron radiographs of the cladding tubes with pure thermal cycle without stress, (in the middle) with thermo-mechanical cycle with tensile stress at the inner area of the cladding (θ = 90° with respect to loading direction), and (on the right) at the outer area of the cladding (θ = 0°). The concentration is based on averaged transmission values integrated over the same radius. The cooling speed was 0.5 °C/min. When no stress is applied, hydrogen strongly accumulates at the liner substrate interface. At the inner half of the cladding, circumferential hydride packets remain. It is assumed that with lower cooling rate the complete hydrogen would have diffused to the liner. In addition, two stress states are shown in Figure 61(b): one with compressive stress at the outer side (liner under compression) and tensile stress at the inner side of the cladding, and another one with tensile stress at the outer side (liner under tension) and compressive stress at the inner side. The angle θ gives the direction with respect to the loading, whereas the loading of the material is induced by two half cylinders, which are inserted into the sample ring, and which are torn apart.

Tensile stress promotes hydrogen diffusion along the stress gradient. When the liner is under tension, it takes more hydrogen especially in the inner part of the liner. If the liner is under compression, hydrides mostly form at the liner-substrate interface. The neutron radiographs also indicate that radial hydrides can be formed at the inner part of the cladding when being under tension. When, instead, the liner is under tension only very slight indications of short radial hydrides are visible.

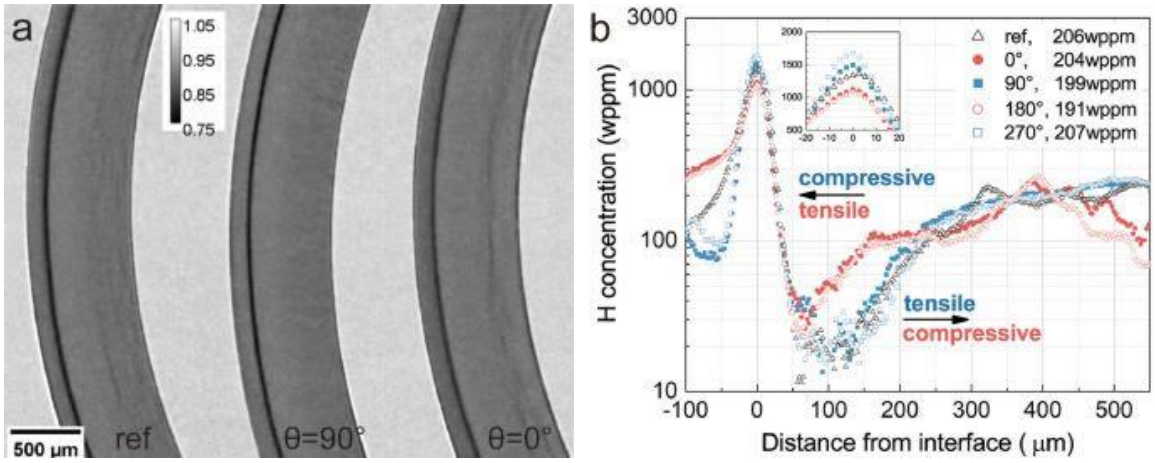

Figure 61 – Neutron imaging and quantification of hydrogen distribution in duplex cladding (outer liner), with a hydrogen concentration of 200 wppm (a) and the extracted radial profiles of hydrogen concentration depending on the distance from the liner (b)

(Taken from Gong et al. [56])

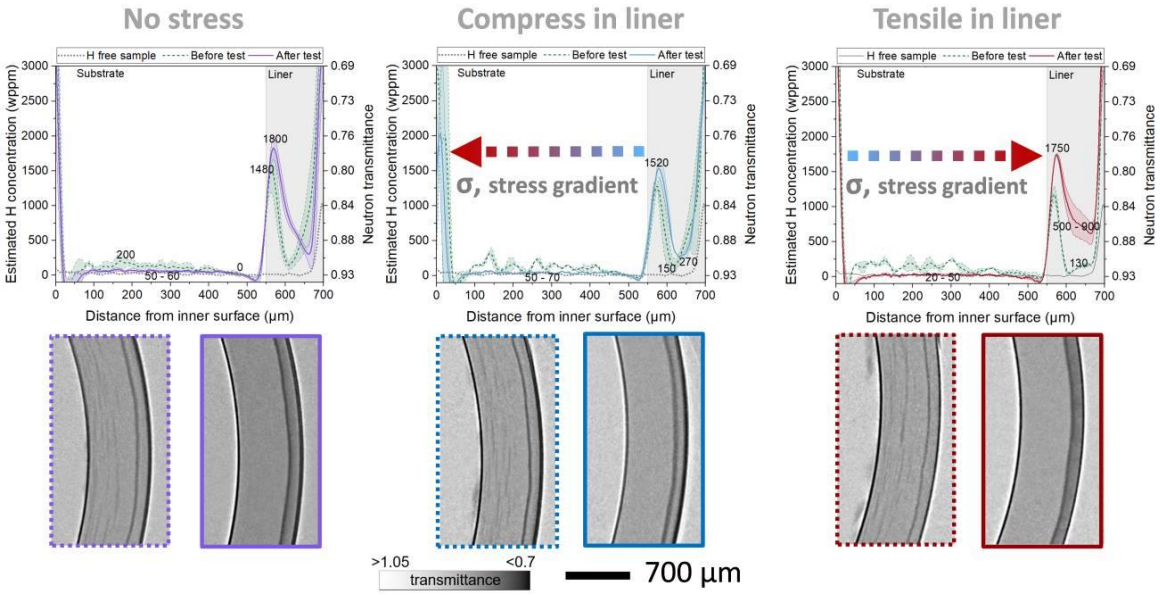

Figure 62 – Neutron radiographies and radially integrated hydrogen concentration curves for duplex Zry-4 cladding with a burnup of about 72 GWd/t_{HM} and H_{total} of 380 to 400 wppm

(Taken from Yetik et al. [57])

Comparable tests have been performed on irradiate cladding, whereas the cooling speed was 10 times slower (3 °C/h) than for the unirradiated case (0.5 °C/min). The hydrogen thus had much more time to diffuse into the liner. The substrate is practically fully depleted. Therefore, in the substrate after thermo-

mechanical testing, neither radial nor circumferential hydrides can be observed. The liner under tension shows a somewhat broader hydrogen distribution also in the middle of the liner, see images and quantification curves in Figure 62.

III) Delayed hydride cracking in presence of an inner liner

Delayed hydride cracking (DHC) is an iterative process where hydrogen diffuses in a stress field of a crack tip and precipitates in front of the crack. When the formed hydride is long enough, it brakes, and the crack propagates. The hydrogen diffusion towards the crack tip continues.

If an inner liner is present, it can be assumed that the hydrogen diffusion is influenced by both, the liner and the crack induced stress field. As it can be seen from Figure 63, there is less hydrogen available for diffusion towards the crack tip, being captured by the liner. At very high temperatures, the hydrogen leaves the liner. It can be stated that the presence of the liner slows down DHC. As intermediate dry storage can span over a very long period, DHC can, however, still develop and lead to cracking [58].

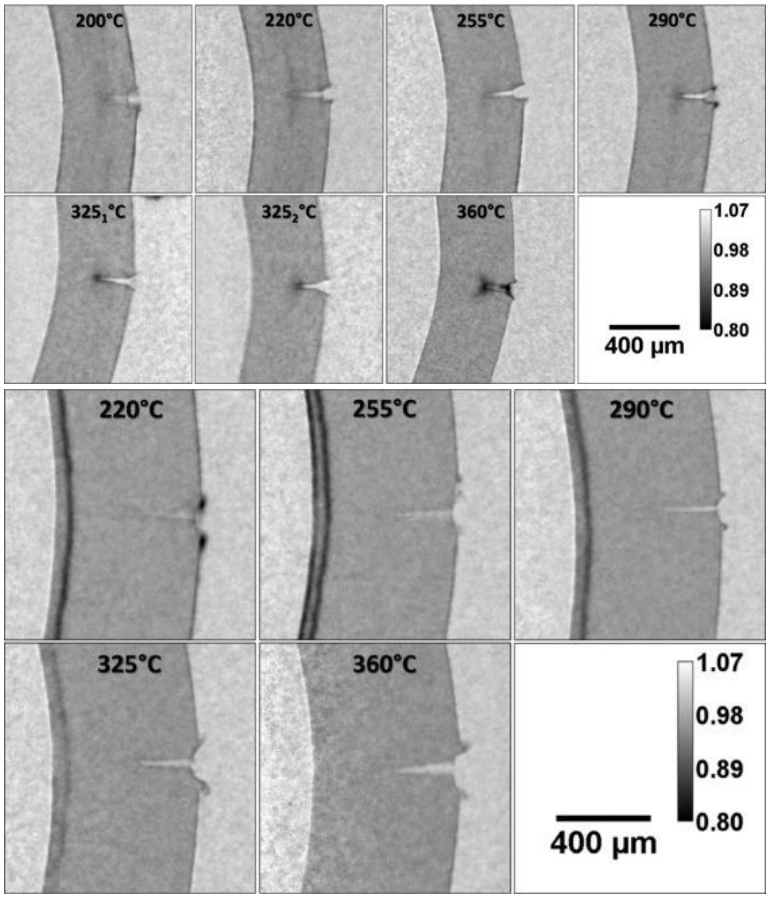

Figure 63 – Neutron radiographs of DHC samples at various test temperatures for Zircaloy-2 without liner and with an integral hydrogen concentration of 200 wppm (top) and for Zircaloy-2 with inner liner, and with an integral concentration of 247 wppm (bottom)

(Taken from Colldeweih et al. [59])

IV) Inner oxide

A feasibility study has been performed on characterisation of the inner cladding oxide using neutron radiography. The problematic of the inner oxide is that there are various implanted spallation products with different contributions to the neutron attenuation. These elements had been investigated by Swiss Federal Laboratories for Materials Science and Technology (EMPA) beforehand. Although the inner

oxide is visible with neutron radiography, the spatial resolution is too small to identify structures like undulations of the pellet-cladding interface, see Figure 64. Nonetheless, an advantage of neutron radiography is its non-destructive character and the possibility to detect stronger inhomogeneities like cracks or hydrides at the interface.

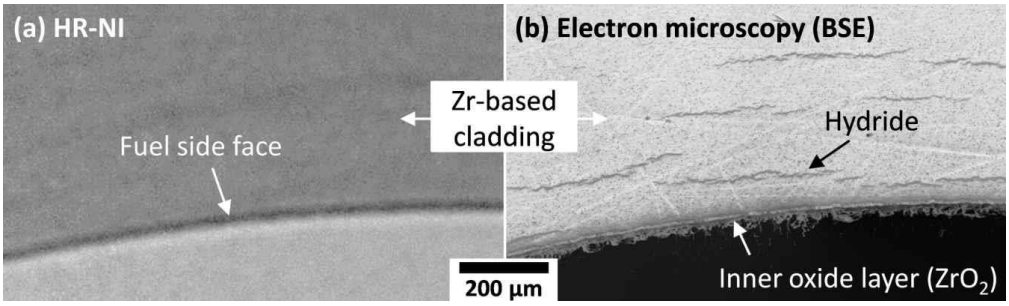

Figure 64 – Comparison of high-resolution neutron image (HR-NI) (a) and SEM image based on backscattered electrons (BSE) (b) with their apparent different spatial resolution

(Taken from Schneider et al. [60])

V) Influence of ring compression creep on hydrogen distribution

During interim dry storage, the fuel cladding can be subjected to creep loading, due to the decay heat and fission gas internal pressure. Different possibilities exist to test creep properties of claddings. Internal pressure tests come closest to reality, but there are also dog-bone type axial tensile tests, ring pin tests or bending tests. The goal of a master thesis at PSI [61] was to identify a simple test setup, which can also be applied in a hot cell. The ring compression test was chosen. The tested samples have been unirradiated Zircaloy-2 and Zircaloy-4 cladding rings without liner, whereas some of them were loaded with hydrogen between 100 and 200 wppm. Finite element modelling was employed to determine the stress distribution in the cladding wall. The ring compression tests exhibit different stages of deformation, comprising bulging, with a high non-linearity, and with varying stress gradients especially at the contact and equatorial points. Due to the applied temperatures and stresses, hydrogen relocation occurred that was investigated by neutron radiography. At least in the performed tests, the hydrogen relocation did not noticeably alter expected creep strain results.

VI) Concluding remarks

Hydrogen is relocated in nuclear fuel claddings by diffusion along temperature, stress, and concentration gradients, and towards the liner if existent. The precipitation of hydrides during cool-down is influenced by mechanical stress. A strong accumulation of hydrides and their disadvantageous orientation can affect the mechanical properties and put the fuel cladding integrity at risk. Neutron radiography is an excellent tool to determine spatially resolved hydrogen and hydrides concentration distributions in claddings, specifically after thermo-mechanical testing. This helps to obtain a better information basis for modelling. It has become clear that a liner plays an important role as it attracts hydrogen, which will then no more be available to form detrimental hydrides in the bulk part of the cladding.

4. Numerical Methods and Analysis

4.1 Overview

Cladding tubes made of zirconium alloys exhibit temperature-dependent and strain rate-dependent elastic-plastic material behaviour with hardening, which additionally changes under the influence of radioactive radiation. For example, under the loading conditions in the ring compression test, a continuous increase in the load on empty cladding tubes without radial hydrides leads to ductile failure, but with radial hydrides, brittle failure of the cladding tube may occur even at a low load level if the temperature is also low.

When modelling the material behaviour, the individual material effects are considered separately where possible for better handling, i.e., the strain (or strain rate) components caused by the effects are usually summarised. The elastic material behaviour is typically assumed to be linear, for small elastic strains according to Hooke's law. When a limit stress, the yield strength, is reached, the material begins to flow plastically and shows permanent deformation after the stress is relieved. For simplified considerations, isotropic plastic flow can be applied using the von Mises yield criterion (see Section 4.4.1). Due to the manufacturing history of cladding tubes, however, the material behaviour actually corresponds more to anisotropic flow with the Hill yield criterion [62]. The development of the yield surface with increasing plastic deformation is given in case of isotropic behaviour either by direct specification of the von Mises equivalent stress as a function of the equivalent plastic strain (and the temperature and strain rate, if required) or by constitutive laws that describe the dependencies in mathematical terms. Such material laws were developed for fuel rod claddings subjected to inelastic deformation up to ductile failure. Long-lasting mechanical stress already below the yield strength leads to irreversible creep strain usually at elevated temperatures.

If material failure occurs, softening and cracking appear, which can be described for ductile failure using damage-mechanics material models (see Section 4.2.1). Brittle failure can be modelled by the initiation and propagation of cracks along the (radial) hydrides and plastic collapse of the ligaments (the bridges between the hydrides in the matrix material). The failure of the cladding tubes is therefore a problem of non-linear fracture mechanics. In this fracture mechanics context, Nilsson et al. [63] investigated the influence of the geometric parameters of the hydrides (size, orientation), the locations of individual hydrides and the interaction of neighbouring hydrides on the cladding tube failure by calculating the so-called *J*-integral as a crack tip load parameter. Section 4.2.2 presents the treatment of the fracture mechanics problem using cohesive zone models.

All material models require material parameters that have been determined as independently of the structural component as possible. This works well for the elastic properties of a cladding tube material. Suitable experimental investigation methods were developed for the plastic behaviour including failure (see Section 3). A realistic description of the material behaviour is required for the further development of fuel performance codes for interim storage conditions (see Section 4.5). The exemplary implementation of a creep law is provided in Section 4.6.

4.2 Material Modelling

4.2.1 Damage Mechanics Models

Damage mechanics models have been successfully used for the simulation of ductile crack propagation in metals over the last three decades. In this context, the ductile material failure is attributed to micromechanical damage processes. Micro-voids are formed at the beginning of the load, which enlarge during subsequent plastic deformation and eventually grow together. Similar to the theory of plasticity, the formulation of continuum mechanics material laws is based on phenomenological approaches under consideration of the thermodynamic principles. In most cases, attempts are made to represent the specific micromechanical processes in a homogenised form. To quantify the material damage, a damage variable is introduced into the material laws. The change in damage as a result of local stress

is expressed by an evolution law that describes the progression of the damage variable. In addition to plastic deformation and hardening, ductile damage models also allow damage and softening to be modelled in constitutive laws. This enables the local deformation behaviour to be linked to the local failure behaviour, which leads to a failure criterion depending on the stress history. Local failure is postulated when the damage variable reaches a critical value.

Damage mechanics models are suitable for simulating ductile failure in the process zone at the tip of a crack because, among other things, the local stress can be taken into account. However, the material laws often have a complicated structure, a high number of parameters and are sensitive to numerical instabilities [64]. Well-known ductile damage models originate from Rousselier [65], based on a thermodynamic approach, and Gurson [66], further developed by Tvergaard and Needleman [67, 68] and originally based on a micromechanical approach. Cockeram and Chan [69] have proposed a micromechanical model based on an enhancement of the pore growth model by Rice and Tracey [70] to predict the ductile failure of Zircaloy-2 and Zircaloy-4 without hydrogen loading. A model to describe the mechanical behaviour, including damage, of Zircaloy-4 with hydrides of arbitrary orientation was developed by Chen et al. [71]. The Zircaloy-4 matrix material is modelled as an isotropic elastic-plastic material. The hydrides are considered as elastic brittle inclusions with damage and preferred directions (e.g., circumferential and radial hydrides). The mechanical reaction of the material is derived from a potential function for the strain energy. However, the model is only based on a very limited amount of experimental data and is not able to describe the crack formation on radial hydrides. Williams et al. [72] used a Gurson-Tvergaard-Needleman (GTN) model with isotropic plasticity to reproduce the mechanical deformation behaviour and ductile failure of a pressure pipe made of the alloy Zr-2.5Nb. As a result, however, it was assumed that better agreement with the experimental data would be achieved if more accurate modelling parameters would be used and strain hardening and the anisotropy of elasticity and plasticity would also be taken into account.

Based on the GTN model, Le Saux et al. [26] have proposed an advanced damage mechanics model for the anisotropic viscoplastic thermomechanical deformation behaviour and ductile failure in the temperature range from room temperature to 480 °C for cold-rolled stress-relieved cladding tubes made of Zircaloy-4 both without and with homogeneously distributed circumferential hydrides for hydrogen contents up to 1200 wppm. Some model parameters could be determined by measurement, others were adjusted to experimental data. The model predictions satisfactorily reproduce the combined effects of hydrogen content and temperature on the viscoplastic properties and failure of the material. Furthermore, the results indicate that the damage is influenced by the stress state, but also that the stress triaxiality may not be sufficient to describe all damage characteristics, such as significant softening in a shear-dominated stress state. These results impressively illustrate the possibilities of a damage mechanics description of the cladding tube material.

4.2.2 Cohesive Zone Models

In cohesive zone models, it is assumed that a narrow strip-shaped zone, the so-called cohesive zone, exists in front of a crack tip, in which the material damage takes place until material separation during the fracture process. The rest of the body is subject to the usual laws of deformation and remains damage-free. The boundaries of the cohesive zone are interfaces between which a force interaction is postulated. The core of a cohesive zone model is the cohesive law (or separation law)

$$\sigma_c = \sigma_{c0} f(\delta / \delta_c), \tag{2}$$

which relates the stress between the boundaries (or the cohesive stress) σ_c and the distance or separation $\delta = u^+ - u^-$ of the boundaries to the boundary displacements u^+ and u^- (here simplified only in the normal direction). There are many suggestions for the shape function $f(\delta/\delta_c)$ in the literature, which differ according to material and failure mechanism (see, for example, the overviews in Brocks and Cornec [73, 74]). In general, the stress initially increases with increasing distance up to a maximum value, the cohesive strength σ_{c0} of the material. When the distance has reached a critical value, the

decohesion length δ_c, the stress decreases to zero and material separation occurs, i.e., the crack propagates.

The approach for modelling the cohesive zone does not include stress singularities at the crack tip in the sense of classical fracture mechanics. The material failure is controlled by the usual variables in the theory of material strength such as stresses and displacements. The cohesive law is a local material law that is independent of the applied load. The integration of the cohesive law Eq. (2) up to the material failure at the decohesion length δ_c, i.e., the area under the curve, provides the separation energy (or specific fracture energy or the work dissipated per surface during material separation)

$$G_c = \int_0^{\delta_c} \sigma_c(\delta)\ \mathrm{d}\delta\ . \tag{3}$$

In the context of linear-elastic fracture mechanics, the connection with the fracture toughness K_{Ic} and energy release rate G_{Ic} is thus given by

$$G_c = G_{Ic} = K_{Ic}^2 / E' \tag{4}$$

with $E' = E / (1 - \nu^2)$ in the plane strain state and $E' = E$ in the plane stress state, where E is Young's modulus and ν is Poisson's ratio. In elastic-plastic fracture mechanics, the separation energy correlates with the physical initiation value $J_i \approx G_c$ if the J-integral is sufficiently path-independent. This means that there is a relationship between the cohesive zone model and classical fracture mechanics [64].

Cohesive zone models seem to be suitable for modelling sample failure in the ring compression test. Due to the high stresses occurring locally as a result of the test, there are predestined locations for cohesive zones. The experimentally found sample behaviour can be described by a fracture-mechanical failure process, which should facilitate the development of suitable cohesive laws. Under load, micro-cracks occur on the hydrides. The high stresses at the crack tip lead locally to damage in the ligament, i.e., the material between the hydrides. If the tension is sufficiently high, micro-voids are formed, which expand and grow together. The micro-crack is thus extended and reaches the next hydride, where the micro-crack formation is repeated. Finally, the individual micro-cracks form a macro-crack that can break through the cladding tube wall. This damage process depends on many influencing factors, e.g., the number of hydrides, their size and distribution and, above all, their orientation. Hydrides do not occur individually, but as a more or less dense network, so that the distances between the hydrides and in particular their alignment to the stress normal play a major role [75, 76]. Martin-Rengel et al. [77] have successfully modelled the ductile failure of ZIRLO® samples with embedded circumferential hydrides, but without radial hydrides, under the loading conditions of the ring compression test using a cohesive zone model.

4.3 Bending Behaviour of Spent Fuel Rods

4.3.1 Modelling of Experimental Setup

The development of a three-dimensional finite element model (FEM) representing a fuel rod segment is a challenging task, since it includes large deformations with non-linear behaviour and undefined geometry of the cladding, pellets and their interaction. Preliminary finite element models were developed based on the results from three-point bending tests on surrogate samples. In this case, the geometrical characteristics and mechanical properties of the pellets and cladding are known in comparison to irradiated samples. As a result, the number of modelling uncertainties could be significantly reduced.

Figure 65(a) shows an overview of a FEM of a fuel rod segment by Nagra simulating a surrogate rodlet in the three-point bending test. The pellets and cladding are modelled as solid elements with a flexible stiffness behaviour. The nominal mechanical and geometrical properties were used, as given in Vlassopoulos [37]. The model uses quarter symmetry to reduce its size (or number of elements) and minimise the computing time. The symmetry planes are along the loading axis and at the pellets' mid-section (or at *y*- and *x*-axes). The former (or deflector) and the support are modelled as shell elements

with rigid behaviour, which does not allow their deformation. A finer mesh was employed at the areas of interest, being the pellet and cladding at the loading point and at the former and support contact areas.

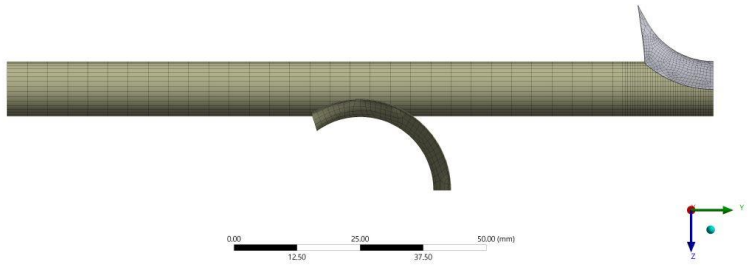

(a) Mesh elements of cladding and former/support.

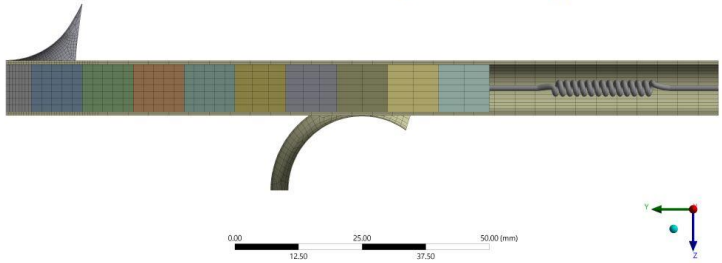

(b) Mesh elements of pellets and spring attachment.

Figure 65 – Three-dimensional implicit finite element analysis simulating a fuel rodlet under three-point bending

A series of boundary conditions was used to represent the experimental setup. The pellets were retained with the use of a spring attached to the end-pellet, as shown in Figure 65(b). Frictionless contact was applied between the cladding and the support to simulate its rotation. Frictional contacts were used for the pellet-pellet, pellet-cladding and former-cladding interactions. In addition, the sample's internal pressure was simulated with a uniform pressure acting on the internal surface of the cladding. Moreover, a fixed support was placed at the shell element representing the support. Finally, loads were applied by assigning a maximum displacement at the former as determined in the test results (fracture point).

The mechanical response of the cladding in plasticity was defined using the Voce material law. The commercial finite element code ANSYS® uses the expression of Voce law as described in the following equation:

$$\sigma = \sigma_0 + R_0 \varepsilon^p + R_{inf}\left(1 - e^{-b\varepsilon^p}\right) \quad (5)$$

where σ is the calculated stress, σ_0 is the initial yield strength, ε^p is the plastic strain, R_0 is the linear coefficient, R_{inf} is the exponential coefficient, and b is the exponential saturation coefficient.

Material properties of pellets were defined using the cast-iron plasticity model. This material law is widely used for modelling ceramic materials as it accounts for different plastic yield and hardening in tension and compression, while still assuming isotropic elastic behaviour. Pellet cracking is indirectly modelled by defining very low values for the compressive and tensile plastic modulus. Based on this approach and in combination with the low tangent modulus (gradient in plastic region) that was defined, the load-bearing capabilities of the pellet are significantly hindered when yielding under any type of load.

4.3.2 Main Results

Based on the model discussed in the previous section, an extensive sensitivity analysis was performed on numerous numerical and physical parameters to examine their relative importance on the results and the uncertainty that could be introduced based on different modelling approaches. A final version of the

finite element model was built upon the results of the sensitivity study, as the best compromise between computational time and solution quality.

In addition, a finite element model representing the irradiated samples was constructed based on a series of assumptions. Their validity was investigated, and the finite element model was used to simulate the mechanical response of the samples under three-point bending conditions. The optimisation code OptiSLang was used to calibrate the finite element models against the bending test results, to understand the most important parameters of the model and finally to derive the cladding mechanical properties. For this purpose, an optimisation problem was solved aiming at reducing the differences in terms of load-displacement curves between numerical and test results. An objective function was created by comparing the load-displacement curve as derived from the simulation to the test results. OptiSLang explored the solution space of this optimisation problem by intelligently generating a number of finite element analyses by varying the parameter values. As initial values and variable ranges for the model parameters linked to fuel and cladding, experimental data (e.g., Young's modulus) found in the open literature were used. The driving parameters of the model were further adjusted till finally the model calibration was achieved by minimizing the difference between predicted and test results. Figure 66(a) shows the comparison of the load-displacement curves for the generated finite element analyses with the test result. The "best fit" has been highlighted in red and shows an almost perfect match with the experimentally derived curve in black.

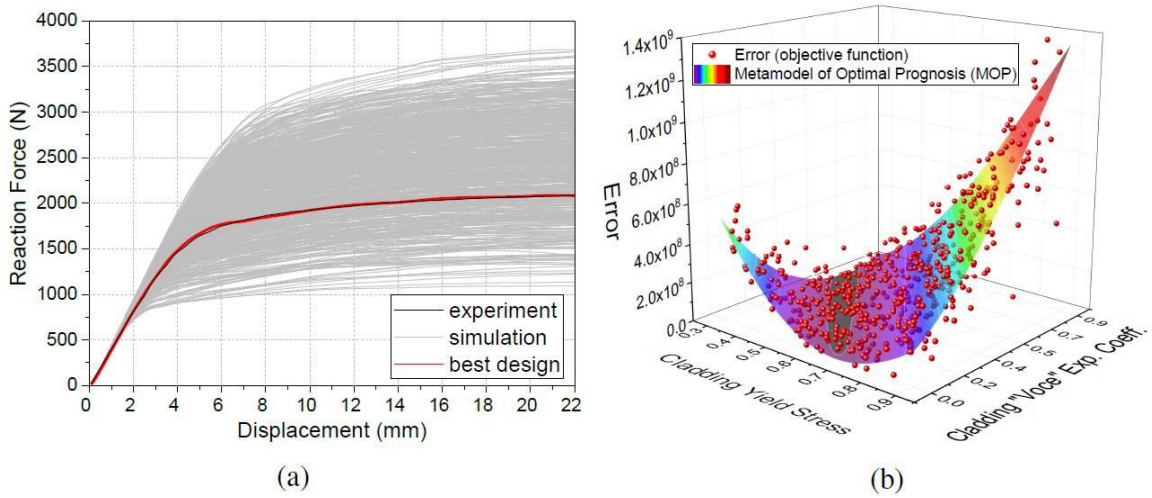

Figure 66 – Force-displacement curves of the generated design points obtained from sampling the variables' range with OptiSLang (a) and Metamodel of Optimal Prognosis (MOP) showing the result deviation or error of each simulation (red points) from the test results (b)

Each simulation can be described from the value of the objective function (or the error). These values can be plotted as a function of the input variables to provide a visual representation of different solution spaces describing the optimisation problem. OptiSLang produces a so-called Metamodel of Optimal Prognosis (MOP), which is a response surface as an explicit function based on the exploration of selected variables. In other words, the MOP is basically the fitted surface created by the response of the most decisive parameters (as estimated in OptiSLang) of the finite element analysis (FEA). Figure 66(b) shows an example of a MOP as derived after a sensitivity analysis on the material properties of the model. The data points in red represent how much the simulation deviates from test results. In this specific case, the effect of the cladding yield stress and Voce exponential coefficient (being the most important parameters in this model) are shown. The goal of the optimisation was to find the best possible solution that describes the cladding mechanical properties by providing the lowest possible difference against the three-point bending test results from of each test.

The cladding properties (as derived from the best design point after the optimisation) are given in Table 10. In addition, the COP (Coefficient of Prognoses) values for each parameter are given along with the total COP, which characterises the quality of the MOP. Although the COP values depend on many factors, it can be observed that the most decisive parameters of the COPs are the Young's modulus (E) and the yield strength (σ_0). This applies in particular to the two samples with high burnup, where only low plastic deformation occurred. Consequently, the parameters describing the development of the yield stress based on the Voce model are less important. These factors showed higher importance for the low burnup case, in particular the Voce exponential coefficient R_{inf}, as expected due to much higher plastic deformation.

Table 10 – Cladding properties and associated COP values as calculated with OptiSLang

Sample	Parameter	E (MPa)	σ_0 (MPa)	R_0 (MPa)	R_{inf} (MPa)	b (MPa)	Total COP
18.3 GWd/t_{HM}	Best-fit value COP	87050 -	699 51 %	545 23 %	112 39 %	186 0 %	 99 %
46.9 GWd/t_{HM}	Best-fit value COP	104762 3 %	776 93 %	717 0 %	364 7 %	407 5 %	 99 %
58.6 GWd/t_{HM}	Best-fit value COP	103500 41 %	800 82 %	138 0 %	350 31 %	660 5 %	 99 %

Finally, a comparison between experimentally and numerically derived effective cladding properties was performed. The results showed very good agreement on Young's modulus and a difference of 30 % to 50 % (depending on the burnup) on the yield strength. Such differences were to be expected, since the test results reflect the flexural beam properties derived using the simple beam theory, which is not suitable for accurately describing the relationship between flexural stress and strain during plastic deformation.

4.4 Brittle Failure under Conditions of the Ring Compression Test

4.4.1 Modelling of Experimental Setup

Spent fuel claddings made of zirconium-based alloys may fail, possibly even through brittle fracture, if mechanical load is applied during handling or transport of the fuel assemblies. High temperatures during vacuum drying and at the beginning of interim storage of the cask can cause existing zirconium hydrides to dissolve. During subsequent slow cooling under pressure-induced tensile hoop stresses in the cladding, radial hydrides can precipitate that may result in embrittlement of the cladding material, see Section 2.2. Whether failure occurs under mechanical load depends heavily on the actual stress state and the morphology of the hydrides. In particular, long continuous radial hydride structures can lead to severe embrittlement of the cladding, so that failure is possible even with minor deformation of the fuel rod, see Section 2.3.

A potentially hazardous load case for cladding tubes with radial hydrides is a fuel rod pinch-type loading. This scenario can be represented under laboratory conditions by the ring compression test (RCT) on a small cylindrical sample. Billone et al. [78] conducted RCT baseline studies on various high-burnup fuel cladding alloys to investigate their deformation behaviour. Later, Billone et al. [20] performed quasi-static RCTs on samples of the same alloys, but with radial hydrides to characterise brittle failure. RCTs on irradiated and unirradiated cladding materials were also carried out in this work package, see Section 3.3.

Since the stress state in the sample is not homogeneous during the RCT, finite element analyses can help to understand the failure behaviour. Stress-plastic strain curves can be obtained from baseline studies (without radial hydrides) to simulate the sample deformation. Martin-Rengel et al. [77] and

Gómez et al. [79] demonstrated the use of a cohesive zone in a finite element model to predict the ductile failure of pre-hydrided unirradiated RCT samples. Simbruner et al. [80] improved the method and applied it to irradiated M5® cladding samples with radial hydrides to simulate brittle fracture under RCT conditions by cohesive zone modelling. Zencker et al. [81] demonstrated the general material-independent applicability of the method to simulate brittle fracture of RCT samples from defueled fuel rods.

RCT modelling is demonstrated using samples of the cold-worked, stress-relieved annealed zirconium alloy ZIRLO®. The samples were cut from segments of about 80 mm in length, which were taken from a defueled fuel rod with burnup of 68 GWd/t_{HM}. Segment 105A was used for baseline tests to investigate the microstructure of the material and to determine stress-strain properties as documented by Billone et al. [78]. The average outer diameter of the corroded cladding was 9.53 ± 0.02 mm, and the outer diameter of the cladding metal was 9.44 ± 0.02 mm. The cladding metal wall thickness was 0.54 ± 0.01 mm. The corroded cladding had an average hydrogen content of 530 wppm. Metallographic studies of samples from this segment have shown that there were a few radial hydrides among predominantly circumferential hydrides.

Segment 105C was taken from the same high-burnup fuel rod from which the as-irradiated segment (105A) was sectioned. Both ends of the segment were closed with weld seams to create a rodlet. This rodlet was subjected to a radial hydride treatment (RHT) to simulate drying and storage of the fuel rod. The sealed and pressurised rodlet was heated to 400 °C to dissolve existing hydrides. The temperature was held for one hour. The rodlet was then cooled slowly at 5 °C/h to 200 °C, where essentially all the hydrogen re-precipitated as hydrides, and afterwards at a faster rate to room temperature. Metallographic studies have shown that this treatment created a network of circumferential and radial hydrides, but with pronounced radial hydride structures.

In the ring compression test, a small cylindrical sample of the cladding was subjected to a compressive load. Figure 67 depicts the experimental setup and the expected force-displacement curve. The continuous line represents the test result of a ring sample without radial hydrides. The dashed line illustrates a load drop due to brittle failure of the sample, which can occur in several steps. This type of failure is usually seen in the presence of pronounced, long radial hydrides. All tests considered here were carried out at room temperature (23 °C) in displacement-controlled mode at constant loading rate of 5 mm/s to the maximum displacement of 1.7 mm using an Instron 8511 servo-hydraulic material testing machine.

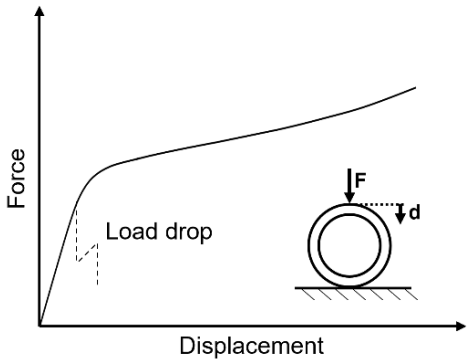

Figure 67 – Schematic force-displacement behaviour in ring compression testing

Based on the experimental data, a finite element analysis (FEA) was carried out to understand the complex interaction between the stress state, hydride structure, and initiation of cracks. The sudden load drops observed in the force-displacement diagram are the result of fast propagating cracks in the hydride structure, which should be reproduced by the FEA model. The model was simplified by

assuming plane strain conditions. The commercial finite element code ABAQUS® in quasi-static analysis mode was used for all calculations. The sample rests on a lower support plate that is assumed to be rigid. The deformation is caused by a movable upper loading plate, also assumed to be rigid, which is pressed onto the top of the sample. The solid section of the ring consists of plane strain elements with eight nodes, quadratic interpolation, and reduced integration (ABAQUS® element type CPE8R). At the 12 o'clock position of the ring, a 1 µm wide gap was modelled along the wall thickness. This gap was filled with a cohesive section of the same thickness. Tie constraints were used to connect the cohesive section and the surrounding mesh. The cohesive section was meshed using two-dimensional four-node cohesive elements (ABAQUS® element type COH2D4). It is important to set the length of the individual sample as the out-of-plane width of the finite elements, as this scales the calculation result.

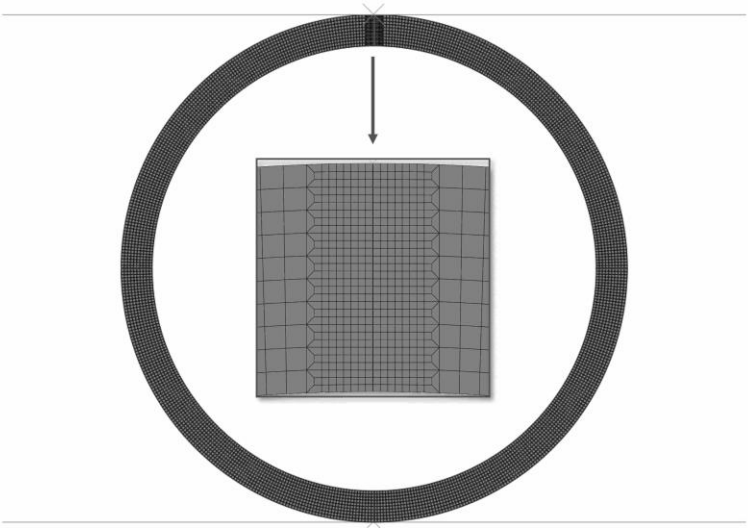

Figure 68 – Finite element mesh employed for cohesive zone modelling

The prescribed displacement of the upper plate applied the load, which was determined as the reaction force. All degrees of freedom of the lower plate were constrained. ABAQUS® surface-to-surface contact was used to model the contact between solid or rigid parts. The finite element model considered non-linear geometry because large deformations were expected. An elastic-plastic model with von Mises plasticity described the material behaviour. Coulomb friction with a friction coefficient of 0.125 based on Arsene and Bai [82] was used for all numerical contacts. Figure 68 shows the complete finite element mesh with a detail around the cohesive zone (CZ). In most of the ring, 10 finite elements were used across the wall thickness. The mesh was refined around the 12 o'clock position to better reflect the complex stress state in the sample. The cohesive zone itself was very finely discretised with 1000 cohesive elements to split the crack propagation into small steps and thus to obtain a smooth and stable calculation result.

The investigation described involves a two-stage FEA approach. In the first stage, a baseline RCT was analysed numerically using the sample 105A9 (from segment 105A before RHT) to get the relevant stress-plastic strain relation (flow curve) by an automated inverse analysis method. In the second stage, a RCT with pronounced radial hydride structures was simulated using sample 105C4 (from segment 105C after RHT) to examine the failure along radial hydrides. In this calculation, the deformation behaviour of the sample was based on the flow curve determined in the first stage.

An appropriate stress-plastic strain curve is required, so that the simulated deformation behaviour of the sample matches the observed experimental behaviour as closely as possible. For that purpose, an iteration algorithm was developed based on Gómez et al. [83]. The initial force-displacement curve is

calculated numerically with a stress-plastic strain curve (σ_i, $\varepsilon_i{}^p$) with von Mises Stress σ_i and equivalent plastic strain $\varepsilon_i{}^p$ assumed for an ideal plastic case (i = 0). The stress σ_i is then modified according to

$$\sigma_{i+1}(\varepsilon^p) = \sigma_i(\varepsilon^p)\frac{F_{exp}(d)}{F_i(d)} \tag{6}$$

with the measured (experimental) force F_{exp}, the calculated force F_i and displacement d, where index i = 0, 1, … denotes the iteration step to minimise the deviations between the numerical and experimental results. The difficulty with this approach is the implicit dependency of equivalent plastic strain and displacement. To establish a relationship between these two variables, the parameterised representation

$$d = d_{min} + (d_{max} - d_{min})\, t \tag{7}$$

is introduced, where the auxiliary parameter t varies from 0 to 1. The displacement at which the linearity of the force-displacement curve ends is referred to as d_{min} and depends on the individual test. The maximum displacement in the simulation is denoted by d_{max}. The relationship

$$\varepsilon^p = \varepsilon_{max}{}^p\, t^{\alpha} \tag{8}$$

is used to interpolate the equivalent plastic strain, whereby the value of the exponent α is typically between 0.5 and 3. Because each integration point of each finite element in the model has a different local equivalent plastic strain, the maximum value over all integration points is meant here. The equivalent plastic strain $\varepsilon_{max}{}^p$ at maximum force can be determined in the RCT calculation carried out for iteration step i. The exponent is derived using the course of the equivalent plastic strain $\varepsilon^p(t)$ from the simulation. In each iteration step i, a new exponent is adjusted using the least squares method. By inserting Eqs. (7) and (8) into the iteration rule Eq. (6), an explicit relation can be established depending on the parameter t. Thus, with the new stress-plastic strain curve (σ_{i+1}, $\varepsilon_{i+1}{}^p$), an iteration process can be carried out until the numerical force-displacement curve matches the experimental curve, see Figure 69.

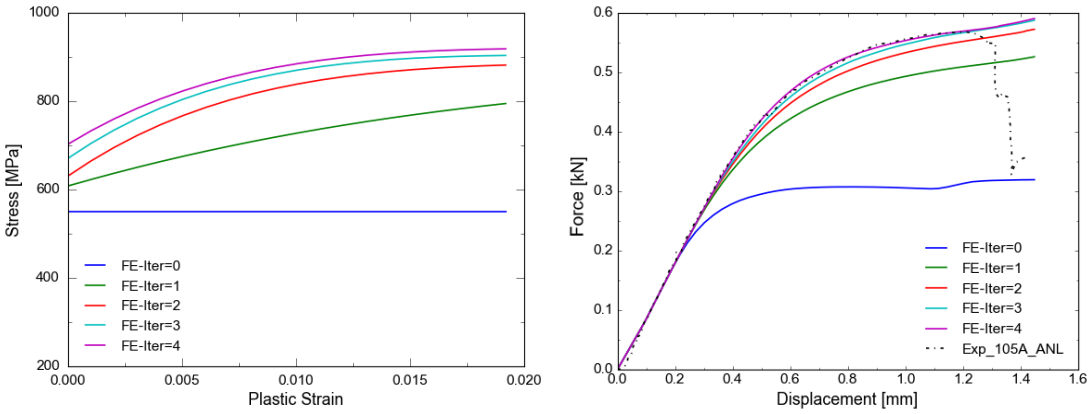

Figure 69 – Iterative procedure to fit the experimental force-displacement curve

The iterative algorithm was implemented as Python code using the ABAQUS®-Python interface for automatic data transfer. The linear elastic behaviour was modelled with a Young's modulus E of 88 GPa and Poisson's ratio ν of 0.37 from Weck et al. [32]. By comparing the deviation from a linear-elastic calculation and the test, the yield stress was determined to be 701.7 MPa. Due to the symmetry, only half of the ring was modelled for the calculations to adjust the flow curve in order to reduce the computing time.

A cohesive zone model (CZM) with a traction-separation law was adapted to describe the failure process along radial hydride structures in irradiated cladding samples. The traction-separation approach consists of three parts: linear-elastic behaviour, damage initiation, and damage evolution. Figure 70 shows a simple traction-separation curve with triangular shape. An elastic stiffness coefficient *k* describes the material response in the elastic part where the separation δ is smaller than a given value δ_1. Young's modulus of the surrounding bulk material is divided by the initial thickness of the cohesive interface, which yields the coefficient *k* of 88000 GPa/mm for the elastic stiffness of the cohesive interface. Once an applied tensile stress σ_c reaches the cohesive strength σ_{c0}, damage is initiated within the cohesive element. As the separation δ of the element increases beyond δ_1, the stiffness decreases monotonically, which is controlled by the scalar damage variable *D*:

$$\sigma_c = k\,\delta\,(1-D) \quad \text{with} \quad 0 \le D \le 1 \tag{9}$$

The separation energy dissipated in the damage process is represented by the area under the traction-separation curve as shown in Figure 70 and is denoted as G_C. The degradation behaviour of a cohesive element is therefore determined by the parameters σ_{c0} and G_C for the given triangular traction-separation curve.

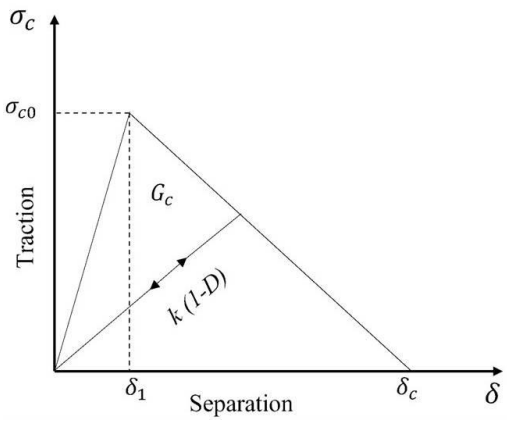

Figure 70 – Schematic traction-separation law

4.4.2 Main Results

The failure mechanism of zirconium-based cladding alloys with radial hydrides subjected to RCT loading conditions consists of two different failure modes and was described by Ruiz et al. [84] based on the analysis of fracture surfaces. Quasi-cleavage along hydride structures was the dominating appearance of the fracture surface and an indicator of brittle failure. Some areas of the fracture surface showed void growth and coalescence associated with ductile failure and crack propagation through the zirconium matrix. Simbruner et al. [80] mapped the structure of the fracture surface of a RCT sample onto a cohesive zone to allow modelling of brittle behaviour along the hydrides and ductile behaviour along the zirconium matrix within the same cohesive zone. A separate cohesive law was used for each of the two failure modes. Various matrix-hydride distributions were investigated with assumptions on the size and distance of the hydrides and on the ratio of brittle areas to ductile areas on the fracture surface.

In the present simulation, the alternating failure due to quasi-brittle fracture at the hydrides and ductile failure of the zirconium matrix segments is considered in a smeared manner, in that the failure mechanisms are not spatially resolved. This results in the approach of an effective cohesive law with only one set of cohesive zone parameters.

The quasi-static RCT on ZIRLO® sample 105C4 with radial hydrides, as described by Billone et al. [20], was selected for the investigation of the failure behaviour of irradiated ZIRLO® cladding. A crack was

assumed from the inside of the sample along a radial hydride structure at the 12 o'clock position, where a cohesive zone was inserted into the finite element model. The stress-plastic strain curve based on the RCT with sample 105A9 at room temperature was given as input to describe the overall deformation behaviour.

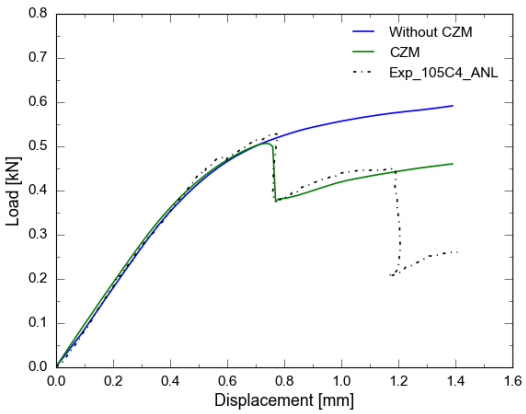

Figure 71 – FEA results with and without CZM compared to the test result

Figure 71 shows the test result together with calculation results with and without a cohesive zone. A series of simulations was carried out to determine the cohesive zone parameters for good agreement with the test results as σ_{c0} of 1010 MPa and G_C of 22.5 N/mm. The first major load drop occurred just after the yield point at around 0.75 mm of global displacement. The maximum load calculated in the FEA before crack initiation and the load drop agree well with the test results. The simulation result shows a load drop of around 25 %, while the RCT showed a value of around 28 %. The load drops are associated with the formation of cracks on radial hydrides at locations with the highest tensile hoop stress, either on the inside (12 and 6 o'clock positions) or on the outside (3 and 9 o'clock positions) of the ring-shaped sample. Crack initiation and brittle crack propagation occur at one of these locations if a suitable radial hydride is present at which a fracture-mechanically critical crack tip load occurs in conjunction with the local stress state. This behaviour corresponds to a phenomenon of the weakest link type.

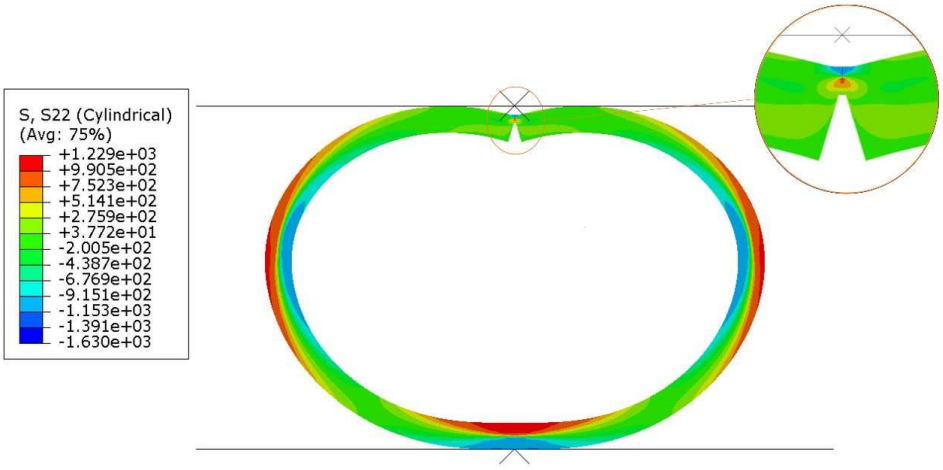

Figure 72 – Hoop stress in the finite element model after crack opening at 12 o'clock position for a ZIRLO® sample with cohesive zone modelling

The hoop stress in the finite element model at the end of the calculation with opened crack is shown in Figure 72. To consider further load drops, additional cohesive zones are necessary at the 6 o'clock position near the inside and at the 3 and 9 o'clock positions near the outside of the modelled sample. However, the determination if a unique set of cohesive zone parameters may be difficult because of complex interactions between zirconium hydrides and the surrounding zirconium matrix in the fracture zone. Simbruner et al. [80] have shown that even minor variations in the positioning of ductile patches in the fracture zone can change the result of the RCT quantitatively and qualitatively. The success of the simulation therefore depends not only on the knowledge of the cohesive parameters, but also on the hydride structure actually present in the sample.

The brittle fracture of cladding samples with radial hydrides can be described with a cohesive zone model if the cohesive parameters are selected appropriately and the hydride morphology is specified. The parameters of the cohesive zone model (i.e., the cohesive strength and the separation energy for a given traction-separation law) may be used as a local two-parameter failure criterion for the safety evaluation of zirconium-based cladding alloys with radial hydrides under RCT loading conditions or fuel rod pinch-type loading, respectively. The cohesive parameters can be determined by inverse analysis of test results of samples that fail by fracture in the RCT. The hydride morphology to be used for this depends on the individual hydrogen content and the thermo-mechanical load history of the cladding tube to be analysed. The interpretation of the separation energy as an energy release rate provides a link to classical fracture mechanics.

4.5 FRAPCON-xt Assessment and Enhancement for Spent Fuel Rod Characterisation

4.5.1 Validation and Improvement of FRAPCON-xt

There is increasing concern about how high burnup SNF can resist a potential accident scenario during dry storage and subsequent handling and transport [85, 86, 87]. The mechanical behaviour of the rod, in particular the cladding, is an important part of related studies. The thermo-mechanical characterisation of spent fuel rods at this stage of the fuel cycle is of essential relevance to be able to assess the behaviour of the cladding in these scenarios. A key aspect of this is the analytical capabilities offered by fuel performance codes.

Fuel performance codes are widely used to predict the behaviour of the fuel rods during the in-reactor stage. Over the last decade, several codes have been extended to cover dry storage conditions [88, 89, 90, 91, 92]. FRAPCON-xt is CIEMAT's in-house extension of the in-reactor code FRAPCON for dry storage conditions [93]. It includes a coupling with HYDCLAD [94], which is CIEMAT´s model to predict the hydrogen performance within the cladding (i.e., hydrogen diffusion, hydride precipitation and reorientation).

Within this work package, FRAPCON-xt (with HYDCLAD) has been assessed on the basis of experimental data and benchmarked against another thermo-mechanical code (namely BISON). The code has also been enhanced in terms of predicting the rod internal pressure (RIP) at high burnup, given that RIP is the driver (through the cladding stress) of the main cladding degradation mechanisms in dry storage (i.e., radial reorientation of the hydrides, creep).

To validate FRAPCON-xt, a database of eleven well-characterised fuel rods from power reactors with experimental measurements of the RIP, void volume and fission gas release (FGR) at end of life (EOL) was compiled from the open literature. Three basic requirements were defined to create a qualified database for this purpose:

- Irradiation in commercial reactors to burnups over 45 GWd/t_{HM}. This would make the database realistic, characteristic of fuel with high burnup structure, and not affected by any experimental protocol.
- Accurate description of irradiation histories, which is indispensable to properly simulate the fuel performance.

- Complete and thorough characterisation of the fuel rod design and the three main variables as the objective of this assessment (pressure, void volume, and fission gas release).

Most of the data were obtained from Calvert Cliffs-1 (14×14 PWR) destructive examination programme [95, 96]. This programme was conducted to extend the operating cycle from 12 to 18 months and to demonstrate an acceptable performance of the fuel rods up to a burnup of approximately 50 GWd/t_{HM}. Ten fuel rods were selected from this study, whereby those with annular pellets were discarded. The fuel rods are made of Zircaloy-4 with two types of UO_2 fuel pellets (11.4 mm standard and 7.6 mm reduced pellet length, respectively). Another fuel rod considered (TSQ002) was obtained from the IFPE database and was part of an experimental programme also made to extend the fuel burnups. RIP at EOL were measured for the fuel rods irradiated in the Arkansas Nuclear One - 2 (ANO-2) reactor (16×16 PWR) [97].

Table 11 summarises the main characteristics of the 11 fuel rods in this study. As can be seen, most of the rods (namely 8) are in a narrow burnup range between about 55 and 60 GWd/t_{HM}. The detailed power histories of the fuel rods can be found elsewhere [95, 96, 97]. Measurements of RIP and void volume were made with an accuracy of 0.08 % and 0.02 cm^3, respectively, in case of Calvert Cliffs fuel rods [96]. No measurement errors were reported for the ANO-2 data.

Table 11 – Main characteristics of fuel rods studied

Rod ID	Cladding material	Rod average burnup (GWd/t_{HM})	Initial void volume (cm^3)	Initial fill gas pressure at 294 K (MPa)	EOL void volume (cm^3)	EOL RIP at 294 K (MPa)	Gas released (10^3 mol)
BFG092	Zry-4	57.95	31.4	2.72	24.7	3.63	2.893
BEN013	Zry-4	59.84	31.6	2.72	24.7	3.81	4.040
BFJ027	Zry-4	58.73	31.9	2.72	25.0	3.69	3.420
UFE067	Zry-4	54.84	32.7	2.72	24.7	4.02	4.170
UFE019	Zry-4	46.79	32.5	2.72	26.2	3.54	1.223
BFM034	Zry-4	63.45	33.7	2.72	26.3	4.30	7.152
BFM043	Zry-4	60.51	34.0	2.72	27.4	4.06	5.438
BFM073	Zry-4	60.32	34.1	2.72	27.7	3.99	5.232
BFM070	Zry-4	60.76	34.3	2.72	27.1	4.09	5.589
BFM071	Zry-4	57.14	33.9	2.72	27.7	3.87	3.808
TSQ002	Zry-4	53.00	25.4	2.62	17.8	3.93	1.540

The experimental data from the database studied have been compared with the results given by the code FRAPCON with the MASSIH FGR model, extending the original validation by Pacific Northwest National Laboratory (PNNL) [98].

Figure 73 shows the predicted RIP compared to the measured RIP at room temperature (21.1 °C). Relative deviations lower than 12 % have been obtained. In addition, there is a tendency to underestimate the measured rod internal pressure at higher values (which also corresponds to higher burnups). Most estimations range from 3.7 to 3.85 MPa, while the measured values for the same

scenarios are between 3.56 and 4.3 MPa. This observation suggests that the MASSIH model is much less sensitive to irradiation in terms of internal pressure than expected in reality.

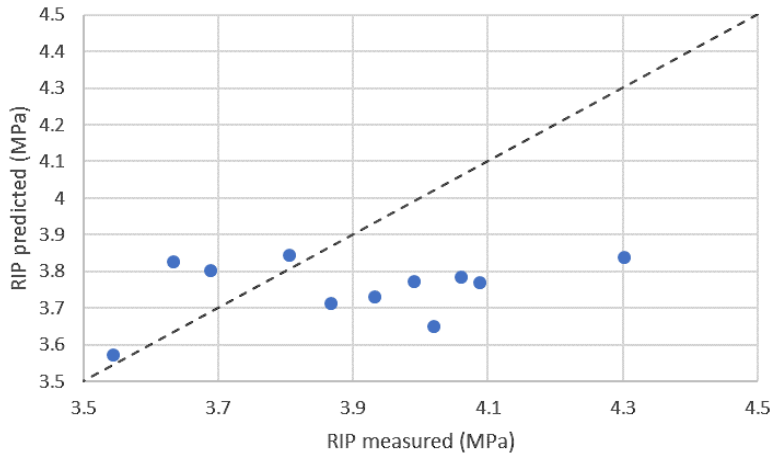

Figure 73 – RIP predicted (MASSIH) vs. measured

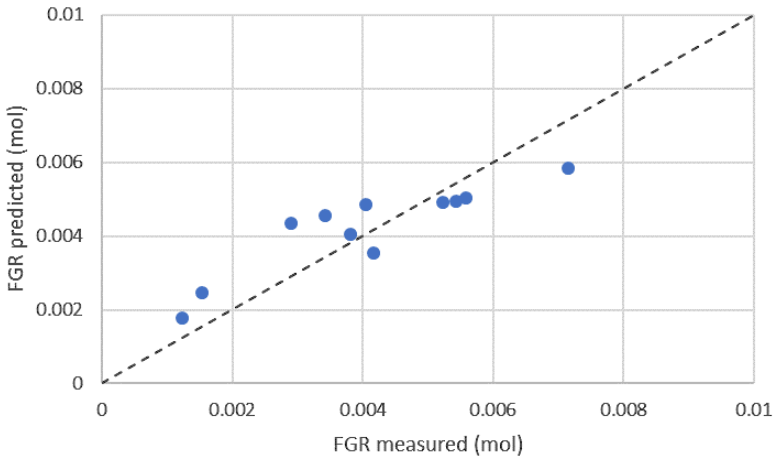

Figure 74 – FGR predicted (MASSIH) vs. measured

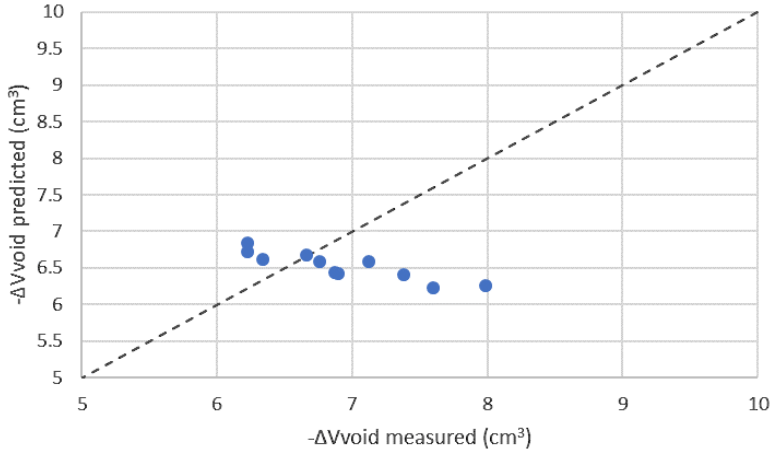

Figure 75 – Decrease in the void volume predicted vs. measured

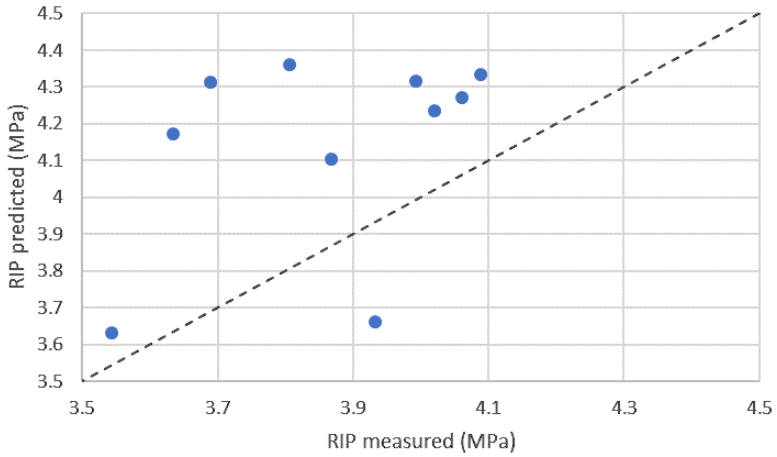

Figure 76 – RIP predicted (FRAPFGR) vs. measured

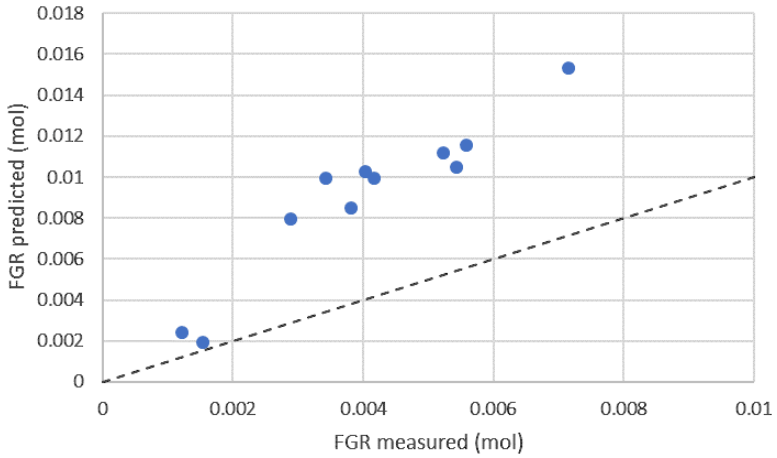

Figure 77 – FGR predicted (FRAPFGR) vs. measured

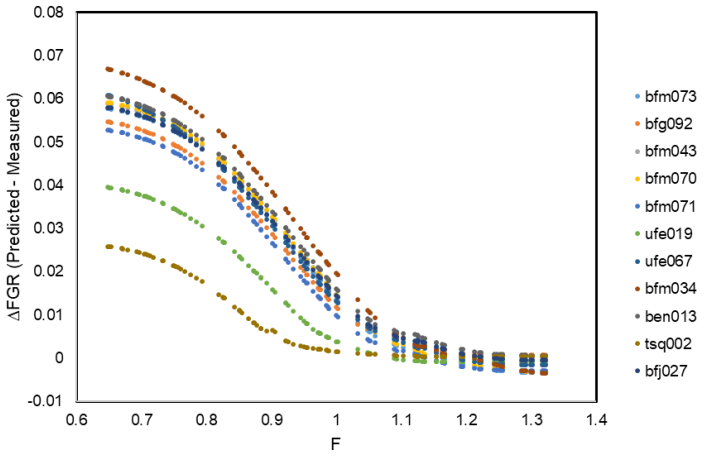

Figure 78 – Monte Carlo analysis to determine the best-fitting parameter F

For a better understanding of these deviations, predictions of FGR and void volume reduction at EOL have been compared with experimental measurements (shown in Figure 74 and Figure 75). In both cases there is a tendency to underestimate the values at high burnup, above around 45 GWd/t_{HM} in case of the void volume reduction and above around 60 GWd/t_{HM} for the FGR. The deviations in FGR are mainly related to the grain re-solution modelling in MASSIH, which is based on a factor fitted to a database mainly from non-commercial irradiated fuel. On the other hand, crack healing and dishing filling not modelled in FRAPCON, have been pointed out as possible sources of the discrepancies found in the void volume reduction [99]. Therefore, the underestimations observed for FGR and void volume reduction at high burnup explain the underestimation in the rod internal pressure.

To avoid the underestimation observed at high burnup in the FGR prediction of MASSIH, an alternative FRAPCON model called FRAPFGR has been checked, which is more phenomenological at high burnup. The results of RIP and FGR obtained with the FRAPFGR model are shown in Figure 76 and Figure 77. In the case of void volume predictions, the differences with MASSIH results are negligible. Important overestimations have been obtained for the release of fission gases with FRAPFGR and, consequently, the RIP estimations are higher than expected.

To reduce these deviations in the prediction of fission gas release, a calibration of the FRAPFGR model was performed in several phases:

- A sensitivity analysis was carried out in which the influence of the most important modelling characteristics (saturation limit, re-solution and release) was compared.
- The re-solution term was determined to be the most sensitive term and then selected as the one to be calibrated.
- A multiplication factor (*F*) was introduced in the activation energy of the re-solution term.
- A Monte Carlo analysis was used to determine the best fitting parameter for each rod (see Figure 78).
- An average best fitting factor of 1.22 was calculated to minimise the deviations.

Regarding the deviations in the void volume reduction, a calibration parameter in the dishes void volume calculations has been implemented above a burnup of 45 GWd/t_{HM} to minimise the errors found in respect of the experimental data.

In Figure 79, Figure 80 and Figure 81, the predictions of RIP, FGR and void volume reduction at EOL are compared with the measurements for the modified FRAPFGR and void volume reduction modelling. In these figures, the data of another fuel rod (A06) with available measurements of the parameters of interest after its irradiation are also included. This rod was irradiated in Vandellós II nuclear power plant to a high burnup of 68.5 GWd/t_{HM}; the A06 main characteristics can be found in Table 12. As can be seen from the figures, the modelling enhancements improve the prediction accuracy even in the alternative case included (A06).

Table 12 – Main characteristics of A06 fuel rod

Rod ID	Cladding material	Rod average burnup (GWd/t_{HM})	Initial void volume (cm^3)	Initial fill gas pressure at 294 K (MPa)	EOL void volume (cm^3)	EOL RIP at 294 K (MPa)	Gas released (%)
A06	ZIRLO®	68.5	19.52	2.35	12.26	6.28	7.4

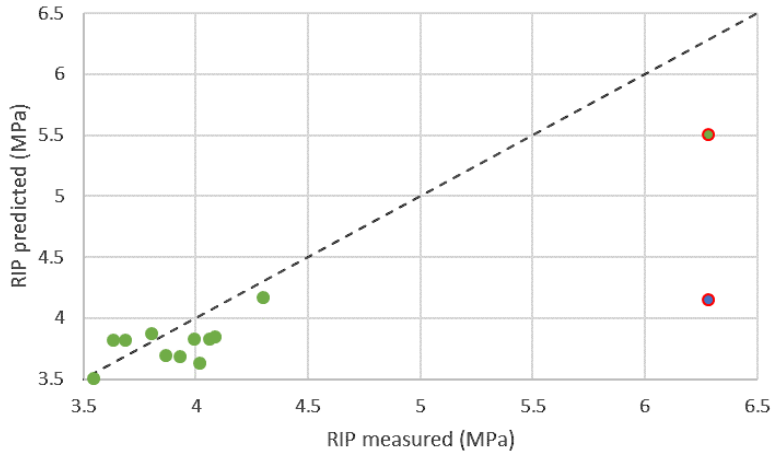

Figure 79 – RIP predicted vs. measured (red circles represent A06 rod, with green filling for calibrated FRAPFGR model and with blue filling for MASSIH model)

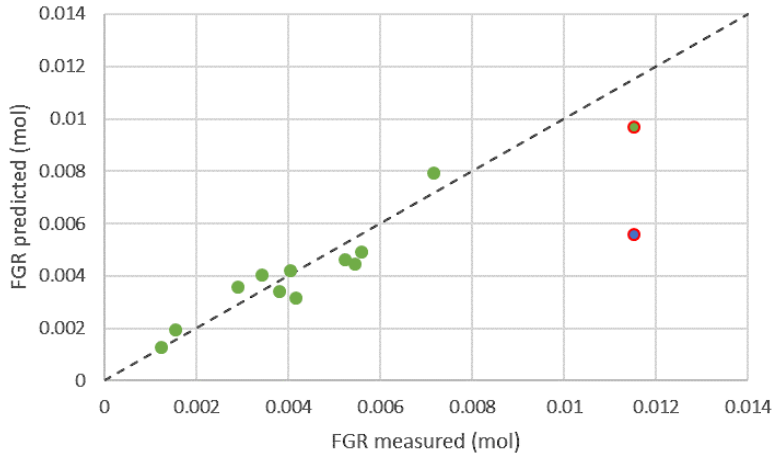

Figure 80 – FGR predicted vs. measured (red circles represent A06 rod, with green filling for calibrated FRAPFGR model and with blue filling for MASSIH model)

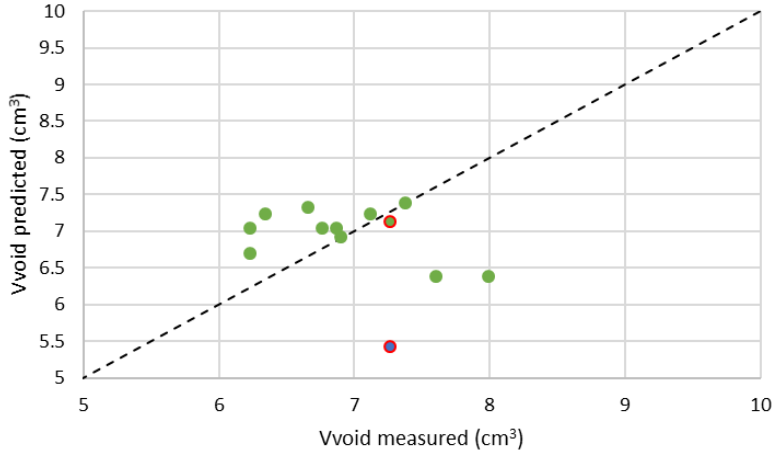

Figure 81 – Decrease in the void volume predicted vs. measured (red circles represent A06 rod, with green filling for calibrated FRAPFGR model and with blue filling for MASSIH model)

4.5.2 Comparison with BISON

In this section, FRAPCON-xt estimations for RIP (by default) and HYDCLAD (coupled with FRAPCON-xt) predictions for the hydrogen distribution at the beginning of the dry storage stage are compared with those provided by the fuel performance code BISON [100]. In addition, the modelling of the behaviour of spent nuclear fuel rods during the dry storage stage is compared in terms of the cladding creep.

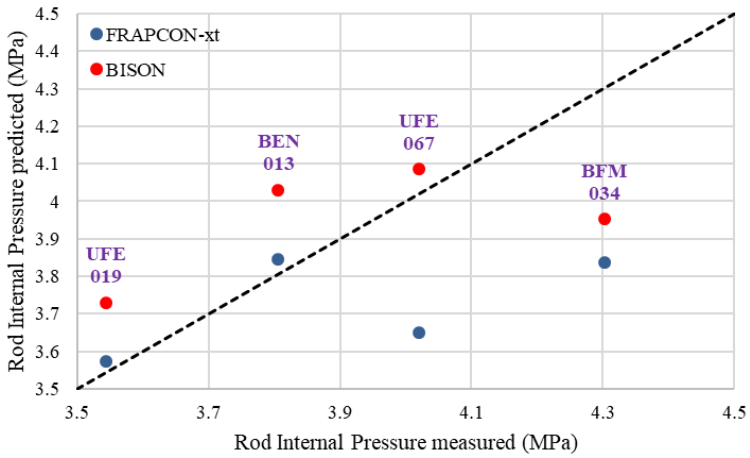

Figure 82 – RIP predicted vs. measured

For the comparison of the rod internal pressures at the beginning of dry storage, four of the rods of the database presented in the previous section (BEN013, UFE067, UFE019, and BFM034) were simulated with BISON. Figure 82 shows the RIP predictions of both codes compared to the measurement results at room temperature. Although both codes give similar average relative deviations (around 5 %), there are some observations that should be emphasised:

- Higher conservatism in BISON results for the four fuel rods studied,
- BISON's predictions for rod UFE067 are much more accurate than FRAPCON-xt's,
- Both codes underestimate the pressure for the highest burnup fuel rod.

To investigate the cause of these differences, the primary variables on which the RIP depends, i.e., fission gas release and void volume at EOL, were also compared.

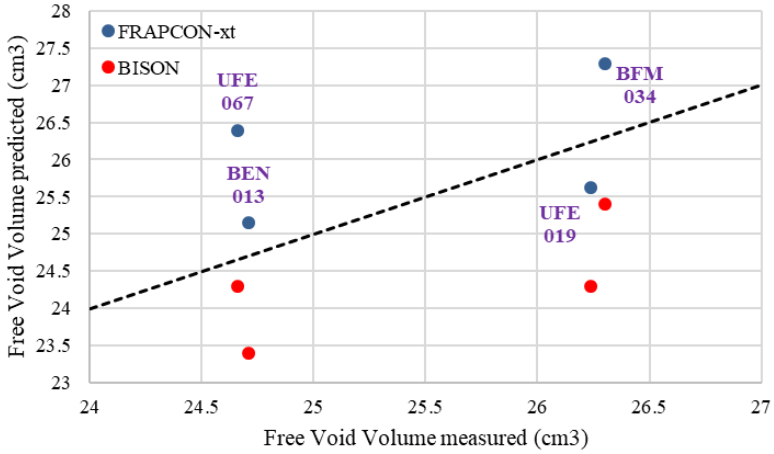

Figure 83 – Free void volumes predicted vs. measured

As can be seen in Figure 83, there are remarkable differences between FRAPCON-xt and BISON void volume predictions. In case of BISON, the calculated final void volumes are lower than the experimental results. Although neither FRAPCON-xt nor BISON provide accurate results for the void volume calculations, the evolution of this parameter with burnup in BISON shows a correct trend, in contrast to the observations made for FRAPCON-xt in the previous section.

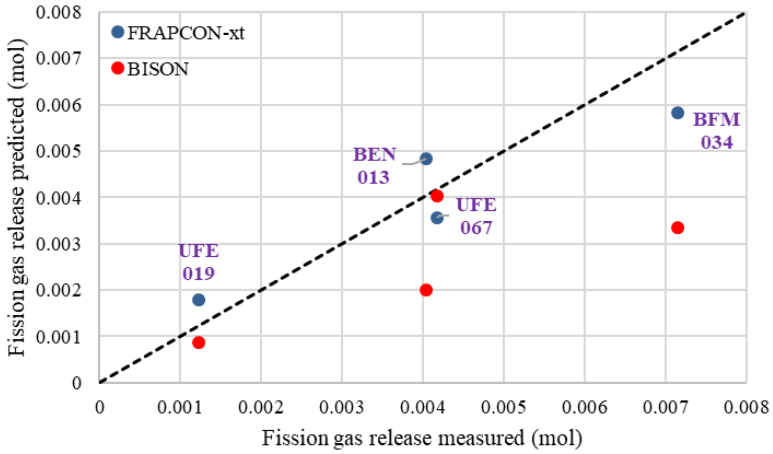

Figure 84 – FGR predicted vs. measured

Regarding FGR, Figure 84 shows accurate predictions of the code FRAPCON-xt, while BISON underestimates this parameter, especially at higher burnups. In these rods, relative deviations of 50 % were obtained with BISON, but less than 20 % with FRAPCON-xt. Although BISON gives better RIP predictions for the two rods with highest burnup, this is due to a compensation of the underestimations in the FGR with the void volume predictions.

To study the hydrogen distribution and hydride precipitation, the A06 fuel rod listed in Table 12 was used. In this rod at the in-reactor end-of-life, a detailed profile of the hydrogen content in radial direction of the cladding was measured at several axial positions [101]. In Table 13, the oxide thickness (δ_{ox}) and hydrogen pickup (H_{pk}) at the axial position selected for this benchmark are given. It should be noted that the cladding oxidation rate and hydrogen pickup fractions have been adjusted to obtain the same values of oxide thickness and average hydrogen concentration for the axial position studied that are listed in the table.

Table 13 – Characteristics at the axial position selected

Parameter	Value
Axial position (mm)	2924
Azimuth (°)	0
δ_{ox} (µm)	104
H_{pk} (wppm)	926

Figure 85 compares the radial hydrogen distribution across the cladding predicted with HYDCLAD and BISON (simulation performed by VTT Technical Research Centre of Finland Ltd); the figure also includes measurement data. The results show that the prediction from the BISON code is far away from the data measured, while HYDCLAD better captures the data trend, being especially accurate in the

prediction of the hydride rim at the outside of the cladding. This area is of special interest from a safety point of view due to the related embrittlement.

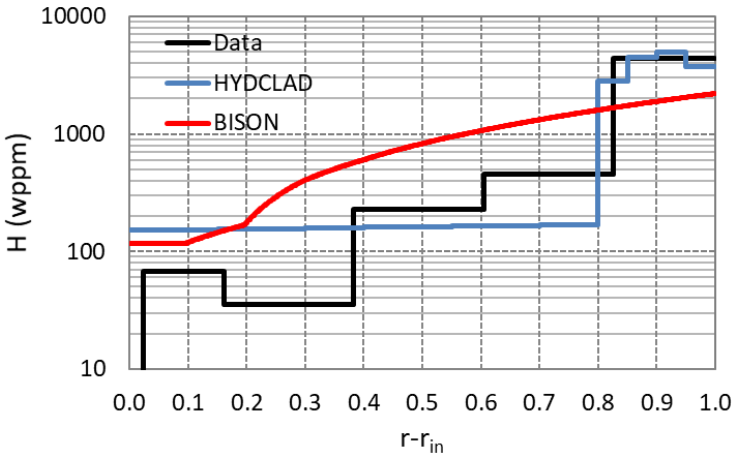

Figure 85 – In-cladding hydrogen radial profiles predicted and measured

Finally, a 20-years dry storage stage was simulated for A06 with FRAPCON-xt and compared with the predictions obtained from VTT with BISON in terms of cladding creep. Figure 86 shows important differences between FRAPCON-xt's and BISON's predictions; these differences were notably reduced by imposing BISON's initial boundary conditions (i.e., RIP and fast neutron fluence at the beginning of the storage) to FRAPCON-xt's simulation. In this way, the absolute deviation could be reduced from 0.5 % to less than 0.05 %. The remaining deviation is a consequence of differences in the stress evolution during the dry storage stage.

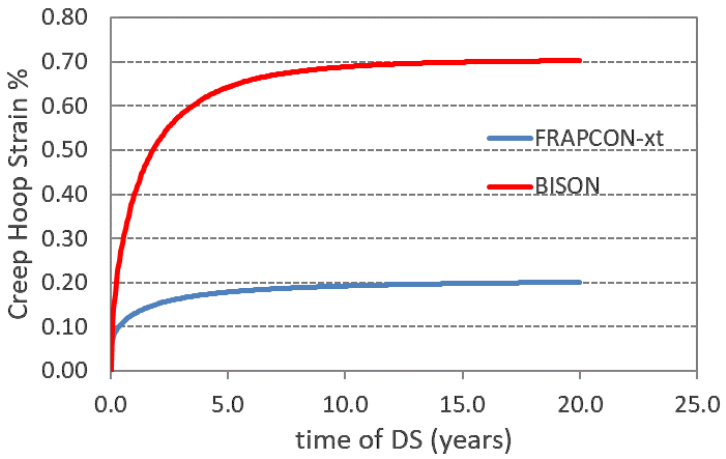

Figure 86 – Creep hoop strain predictions during Dry Storage (DS)

Summarising this section, BISON's FGR and in-clad behaviour modelling does not improve the results obtained with FRAPCON-xt (and HYDCLAD). In the case of void volumes at end of life, BISON's results are conservative in terms of RIP prediction and, contrary to FRAPCON-xt, the evolution of the void volume with the burnup follows the expected trend. The modelling of the dry storage stage shows considerable discrepancies between the two codes, which are mainly due to differences in the irradiation stage (boundary conditions during dry storage), but also to different stress evolution during storage.

4.6 Creep Investigations with BISON

4.6.1 Fuel Performance Code BISON

BISON is a fuel performance code developed by Idaho National Laboratory (INL) since 2009 [102]. BISON is built within the INL's MOOSE (Multi-physics Object-Oriented Simulation Environment) framework [103], which is a calculation platform hosting several applications. BISON utilizes MOOSE modules to solve solid mechanics, fluid dynamics, heat conduction, etc. MOOSE is a general solver that uses the finite element method (FEM) to solve partial differential equations (PDEs). BISON solves coupled systems of PDEs that represent engineering scale nuclear fuel behaviour. The fuel simulations consist of solving the energy, momentum, and mass conservation equations simultaneously using FEM. The theoretical foundation behind BISON is found online [104].

BISON solves the fully coupled thermo-mechanics and species diffusion in one-dimensional (spherical), two-dimensional (axisymmetric) and three-dimensional geometries. Fuel models describe temperature and burnup dependent thermal properties, swelling, densification, thermal and irradiation creep, relocation, fracture, and fission gas production and release. In order to model cladding mechanical behaviour, plasticity, irradiation growth, and thermal and irradiation creep models are included. Models are also able to simulate gap heat transfer, mechanical contact, and the evolution of free volume pressure. The BISON version applied is a development version based on version 1.5, fetched from INL's Git repository on 6 April 2022. The code is used within one of VTT's Linux clusters.

In this work package, CIEMAT's dry storage creep law [105] was implemented into BISON. A more detailed report is also available [106]. Previously, the model has been implemented into VTT's version of the ENIGMA fuel performance code [88]. The creep law was first tested with an example input delivered with BISON, and the results are qualitatively reasonable. Then the law was applied to the mother rod of a reactivity-initiated accident (RIA) test made in CABRI test reactor, the CIP0-1 test (17×17 PWR rod with ZIRLO® cladding, mother rod average burnup of 68 GWd/t_{HM}). Cladding hydrogen distribution during dry storage was also studied with that simulation case.

Although the CIEMAT creep law is applied to ZIRLO® cladding in this report, the law is based on an experimental database of stress-relieved annealed Zircaloy-4 cladding alloy. In BISON and FRAPCON, a factor of 0.8 is applied with ZIRLO® cladding during steady-state operation to decrease the creep given by the Zircaloy-4 creep law. This approach could also be used during dry storage. Test results of cladding out-of-reactor creep for other cladding types than Zircaloy-4 should be obtained to model the creep of those alloys (e.g., Zircaloy-2, M5®).

To limit the possibility of cladding rupture resulting from creep and embrittlement by hydrides in dry storage, cladding stress and temperature are constrained by the regulations. The regulations vary from country to country; in the USA, a maximum temperature limit of 400 °C under dry storage and the preceding drying and backfilling has been set [107]. If the burnup is less than 45 GWd/t_{HM}, the temperature limit may be exceeded if the hoop stress is less than 90 MPa [107]. The safety limit can also be defined in terms of hoop strain; in this case, a limit of 1 % is considered in some countries [108].

4.6.2 Modifications to the Source Code

The implemented CIEMAT creep correlation is given below. The implementation is carried out in such a way that the creep hoop strain is updated with the result of the correlation specified:

$$drysto\_creep\_local = drysto\_creep\_local\_old + 0.01 * (A * (hoop\_stress\_local / 1e6)^{B} * exp(-C / temperature\_local) * exp(-D * fast\_neutron\_fluence\_local) * ((t - end\_time) / 3600.0)^{-0.5}) / 3600) * timestep. \quad (10)$$

Here, the *end_time* is the start of the dry storage period and t is the current time. SI units are used in BISON whereas the CIEMAT correlation applies percent as a unit of creep rate and hour as unit of time; therefore, those are converted into SI units in the implemented correlation. Values of the coefficients

[105] are: $A = 3.0 \cdot 10^4$; $B = 1.84$; $C = 15000$; $D = 2.8 \cdot 10^{-22}$. If the temperature is equal or higher than 653 K and hoop stress equal or higher than 187 MPa, then $A = 150$ and $B = 2.95$.

Before using the dry storage correlation for the first time, the cumulated creep from the reactor operation is added to *drysto_creep_local* in Eq. (10). If the hoop stress during dry storage is locally negative, the creep strain rate is assumed to be zero at that location during that time step as correlation in Eq. (10) cannot handle negative stresses. The default creep model in BISON by Limbäck and Hoppe is used before entering the dry storage period [104].

The cladding oxidation model in BISON is modified to stop outer surface oxidation during pool and dry storage. Justifications for negligible oxidation during the storage period can be found in a paper by Rossiter [89]. Without this modification, the default EPRI/KWU/C-E oxidation model in BISON continues to produce significant oxidation during dry storage. Turning off the oxidation, however, did not affect the dry storage creep results. This is a surprising result, as oxidation should affect the cladding creep. It is not clear whether thinning of the cladding wall due to oxidation is taken into account in BISON. It was tested by simulating the steady-state operation time with a multiplication factor of 1.1 in the oxidation rate; the maximum oxidation increased but there is no difference in cladding creep during steady-state, suggesting that oxidation is not considered in BISON mechanical model by reducing the cladding thickness.

In case of the CIP0-1 mother rod, the implemented creep model was tested with an axisymmetric (2D-RZ) mesh with smeared solid fuel pellets (i.e., no dishes and chamfers), generated within the BISON input file without any external meshing software. Testing has been done with 8-node quadrilateral finite elements (another option being 4-node quadrilateral elements). The other input that was tested (delivered with BISON) uses a mesh created with an external meshing tool, and the pellets had dishes and chamfers in that mesh.

In order to activate the CIEMAT creep model, the following must be given in the BISON input file, under Materials section / creep model: “type=ZryCreepDryUpdate” and “end_time='${storage_start_time}'”. In order to deactivate the oxidation after reactor operation, “end_time = '${irradiation_end}'” must be added under Materials section / Zircaloy oxidation.

The following submodules are new or modified:

- ZryCreepDryStorageUpdate.C: Same as ZryCreepLimbackHoppeUpdate.C except that it contains a flag, which suppresses its use after reactor operation.
- ZryCreepDryUpdate.C: The CIEMAT correlation is implemented into this new submodule.
- ZryCreepUpdateBase.C: Modified original submodule to update the creep hoop strain with the creep strain coming from ZryCreepDryUpdate.C.
- ZryOxidation.C: Modified original submodule to stop oxidation after reactor operation.

The corresponding header files have also been created.

4.6.3 Main Results

Spent fuel example input delivered with BISON

The implemented creep model was first tested with a spent fuel example input delivered with BISON. The results are qualitatively reasonable, see Figure 87, Figure 88, and Figure 89. In this simple case, a constant linear heat rate of 25 kW/m and an axially flat power profile are used throughout the irradiation. The results show high creep at the beginning of dry storage; after a few years, the creep rate slows down. This is consistent with the earlier results with the CIEMAT correlation in FRAPCON-xt [105], which is a version of FRAPCON extended by CIEMAT.

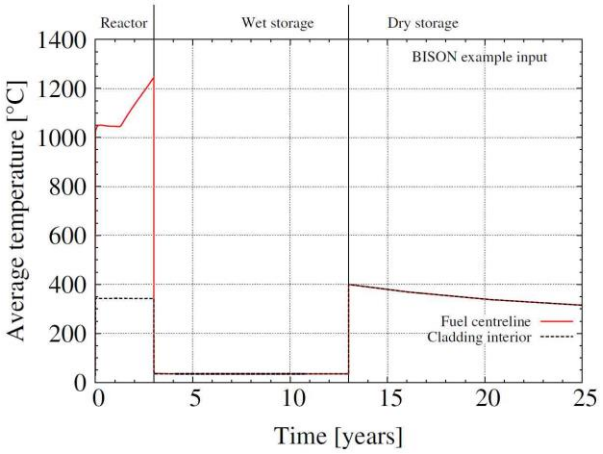

Figure 87 – Applied temperature history (example delivered with BISON)

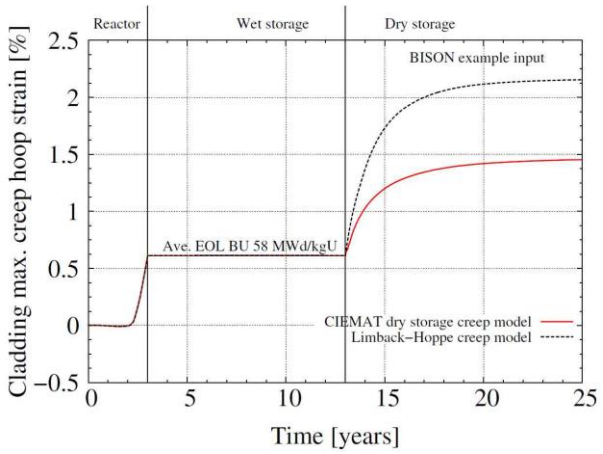

Figure 88 – Axially maximum cladding creep hoop strain calculated with the CIEMAT model and compared with the default Limbäck-Hoppe creep model

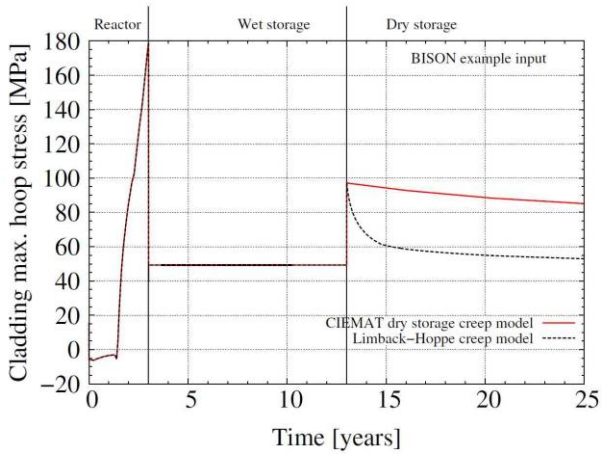

Figure 89 – Axially maximum cladding hoop stress calculated with the CIEMAT model and compared with the default Limbäck-Hoppe creep model

CIP0-1 mother rod

For the sake of simplicity, with the CIP0-1 mother rod, the wet storage period was not modelled except that there is a period of one week with 50 °C in between the irradiation and dry storage. With the creep simulations, the number of pellet and cladding elements in axial direction was 200 and in radial direction 12 and 4, respectively. In hydride modelling, the number of axial elements was 900 and cladding radial elements was 10.

The coolant channel thermal hydraulics model in BISON was applied during the steady state operation. It should be noted that the temperature history during the wet and dry storage period has been imposed and a flat axial temperature profile is used, see Figure 90. The initial temperature at the beginning of dry storage has a high impact on the cladding creep, as dictated by Eq. (10); for these simulations, the temperature limit of 400 °C from the U.S. NRC regulations is applied.

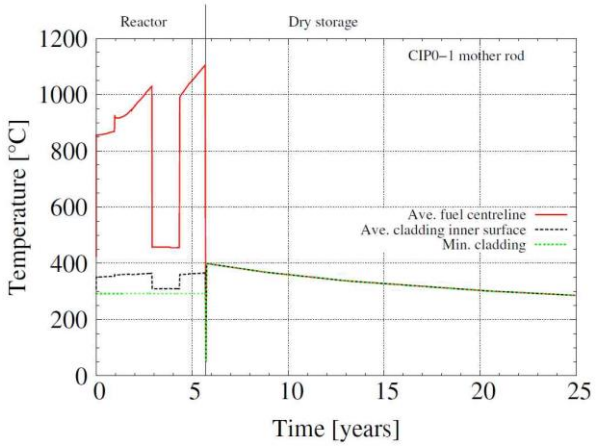

Figure 90 – Applied temperature history (CIP0-1 mother rod)

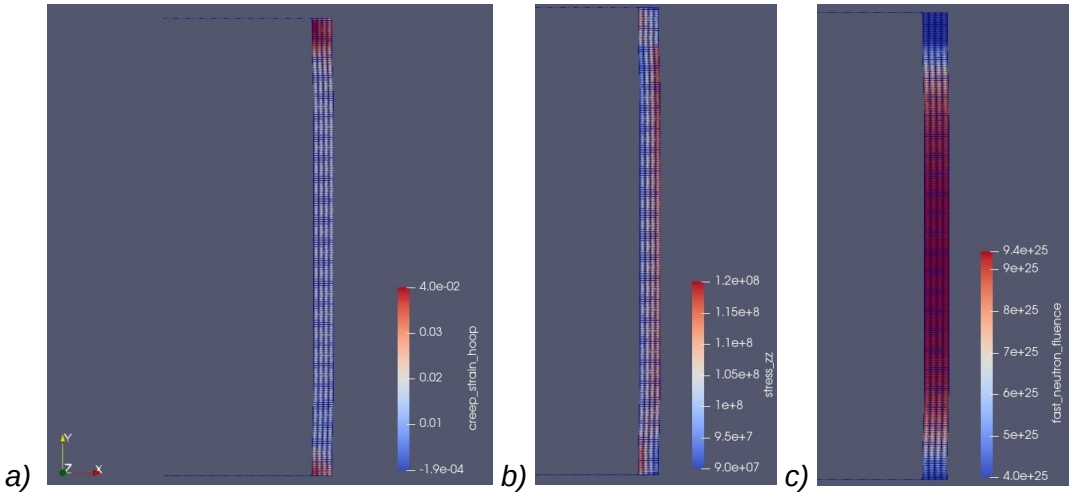

Figure 91 – Cladding creep hoop strain distribution (a), hoop stress distribution (b), and fast neutron fluence (c) at the end of dry storage (axial direction shrunk)

Creep is highest at both ends of the rod. The maximum creep strain after 19.2 years of dry storage is 3.0 % (at the ends of the rods) and 0.9 % in the axial middle part of the rod (see Figure 91(a); the negative creep values are located at the top and bottom plugs of the cladding). The hoop stress axial distribution is quite uniform (see Figure 91(b)), but the fast neutron fluence distribution is non-uniform (see Figure 91(c)). The fast fluence (i.e., burnup) is lower in the end parts of the rod and according to Eq. (10), this results in higher creep.

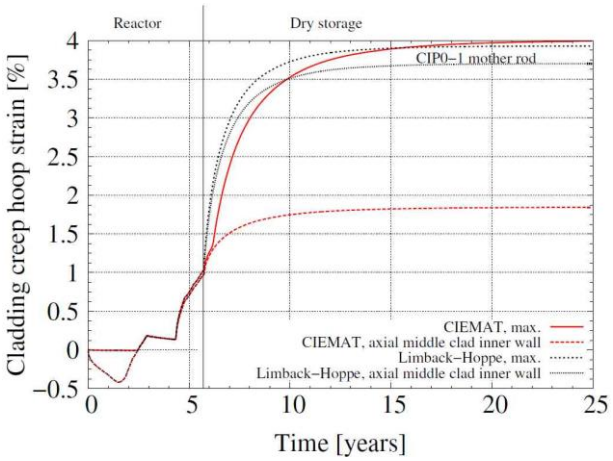

Figure 92 – Cladding creep hoop strain for CIEMAT model and default Limbäck-Hoppe model

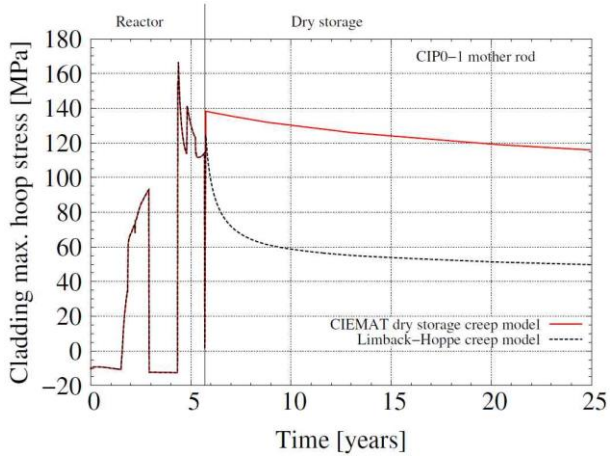

Figure 93 – Cladding maximum hoop stress for CIEMAT model and Limbäck-Hoppe model

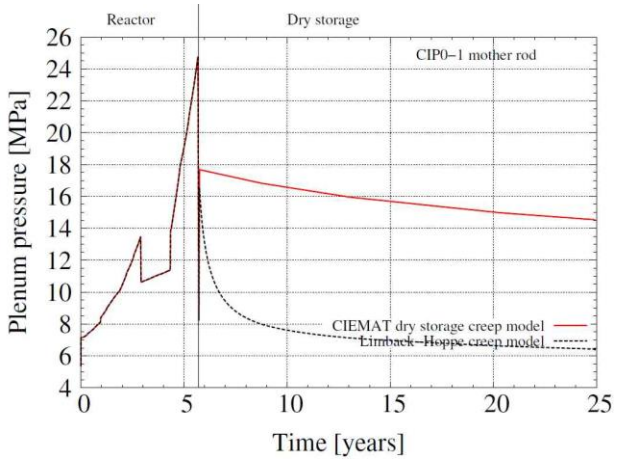

Figure 94 – Plenum pressure for CIEMAT model and default Limbäck-Hoppe model

Compared to the Limbäck-Hoppe creep model, the creep strain is lower with the CIEMAT model, and consequently it leads to higher hoop stress values (see Figure 92 and Figure 93). Due to lower creep strain, the rod internal pressure remains at a higher level with the CIEMAT model compared to the Limbäck-Hoppe model (see Figure 94). In both cases in the figures, the default Limbäck-Hoppe creep model is used before entering the dry storage period.

With BISON, the fission gas release (FGR) is 8.2 % (see Figure 95). As comparison, according to a VTT-ENIGMA calculation, the FGR in the CIP0-1 mother rod is 10.2 %. The experimental post-irradiation examination values for the CIP0-1 mother rod are [109]: FGR of 7.4 %, free volume of 12.26 cm^3, and plenum pressure of 5.85 MPa at 0 °C. The end-of-life plenum volume calculated with BISON is 10.13 cm^3 at 50 °C (or 10.50 cm^3 at 20 °C). This volume does not account for a remaining pellet-cladding gap, but the gap is mostly closed (there is a small gap at both ends of the rod).

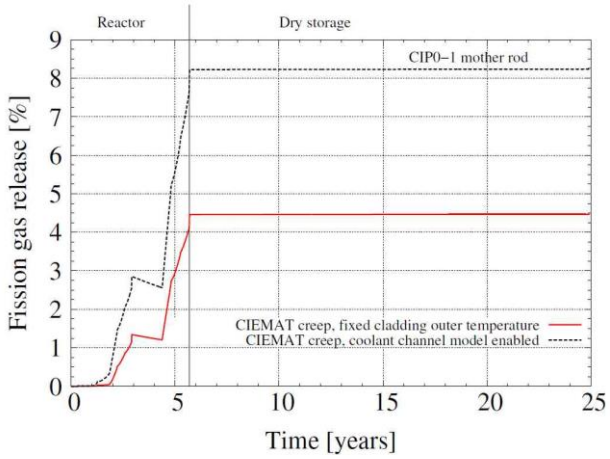

Figure 95 – Fission gas release

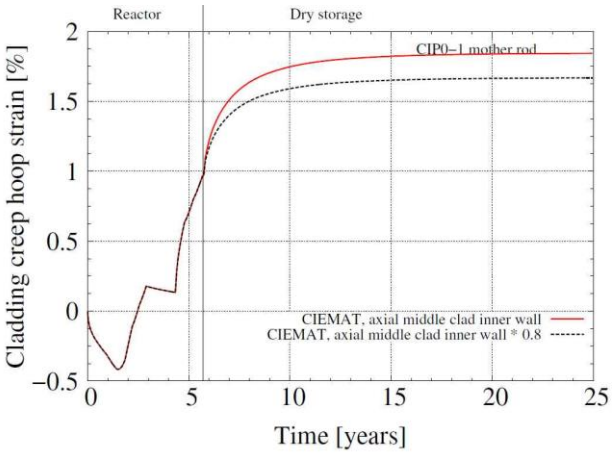

Figure 96 – Effect of factor of 0.8 in the CIEMAT creep model as used in the Limbäck-Hoppe steady state creep model for ZIRLO®

The Limbäck-Hoppe steady state creep model for ZIRLO® applies a factor of 0.8 to decrease the creep given by the creep law of Zircaloy-4. During dry storage, however, this model is bypassed and replaced by the CIEMAT model in which this reduction was not applied. If the 0.8 multiplication factor is applied, the inner wall axial mid-plane hoop creep strain at the end of the dry storage simulation is reduced from 0.9 % to 0.7 %, see Figure 96. The other results presented here are calculated without this factor.

Compared to FRAPCON-xt results of the CIP0-1 mother rod, creep calculated with BISON is considerable higher. The FGR is higher in BISON and that contributes to higher cladding hoop stresses at the beginning of storage. Also the stress evolution during the storage is different. The minimum fluence is lower in BISON, which also contributes to the higher value of creep.

Cladding hydrides

Regarding the hydride radial profile in the CIP0-1 mother rod, the results are presented in Figure 97 for one axial location and compared to experimental values. In this simulation, BISON could not predict accurately the radial profile and the hydride rim in the outer part of the cladding, even though the overall trend of increasing amount of hydrides when moving outwards is correct. The new default model of modified Hydride Nucleation-Growth-Dissolution (mHNGD) by Passelaigue et al. [110] for improved hydride rim modelling was applied in the simulation. The coolant channel model was active with this simulation. However, it should be noted that this simulation was done by using a single mesh for the cladding, while Lacroix and Motta [111] had used a coarse mesh for calculating the hydrogen ingress and thermo-mechanical solution, and then used a fine mesh to calculate the hydrogen distribution (64 radial elements vs. 10 in the simulation reported here) in another simulation that uses the output of the first simulation as boundary condition. This kind of approach could improve the results but it was not attempted here. A lot of time was spent on just to get the basic input working without convergence problems, so the allocated resources were not enough for testing the two-input approach in hydride modelling.

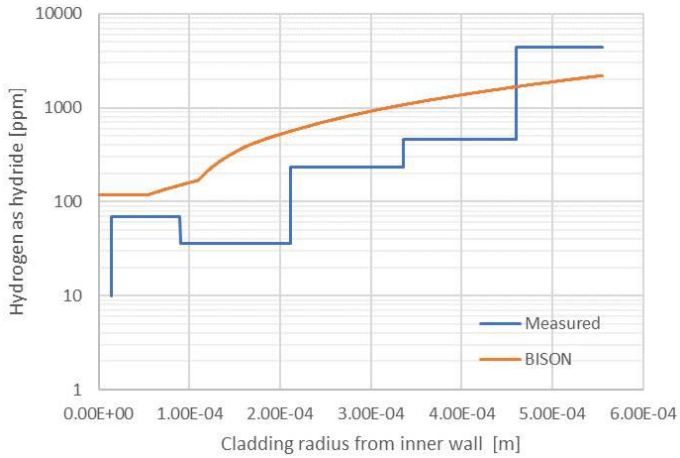

Figure 97 – Cladding end-of-life hydride radial distribution at 20 °C calculated with BISON and compared to PIE data of CIP0-1 mother rod

(PIE results digitised from a paper by Feria and Herranz [94]. Axial position is 2924 mm from the bottom of the fuel stack (fuel stack total height: 3657.6 mm) as in the paper by Feria and Herranz [94].)

5. Inventory Specification related to SNF Management

5.1 Review and Analysis of Documents for SNF Management

The Technical University of Sofia (TUS) has carried out a study on the specifications and requirements for the interim storage of spent nuclear fuel using the inventory from the units of the Kozloduy nuclear power plant (Kozloduy NPP) in the Republic of Bulgaria. It is based on a review and generalisation of the Bulgarian legal framework regarding the safe use of nuclear energy and the safe management of radioactive waste and spent nuclear fuel [112, 113] as well as selected national reports on the strategy and safety of spent fuel management and related documents from Kozloduy NPP.

The focus was on the requirements and their implementation for interim storage in the wet and dry storage facilities for spent fuel assemblies at Kozloduy NPP site. The main sources were the following documents:

- Strategy for the management of spent fuel and radioactive waste until 2030 [114],
- Regulations on ensuring the safety in spent fuel management [115],
- Regulations on the conditions and procedure for transport of radioactive material [116],
- Updated national action plan of Bulgaria – European stress test at the Kozloduy nuclear power plant as of 2018 [117] and 2021 [118],
- Final report on the implementation of the updated national action plan of the Republic of Bulgaria [119],
- Sixth national report on fulfilment of the obligations of the joint convention on the safety of spent fuel management and on safety of radioactive waste management [120],
- Bulgarian Nuclear Regulatory Agency – Annual report, 2020 [121],
- Bulgarian Nuclear Regulatory Agency – Annual report, 2022 [122].

Based on the review, lists of references and key requirements for SNF management were established, mainly related to the spent fuel storage facility with underwater storage technology and the dry storage facility for spent fuel.

5.2 Storage Facilities at Kozloduy Nuclear Power Plant

The spent nuclear fuel from operation of the VVER-type reactors at the Kozloduy NPP is stored in two storage facilities, namely the Spent Fuel Storage Facility (SFSF) with underwater storage technology and the Dry Spent Fuel Storage Facility (DSFSF). The spent fuel storage facility SFSF stores fuel assemblies from VVER-440 as well as from VVER-1000 reactors, which have been disposed for at least 5 years in the reactor pools of the units 5 and 6. In the dry storage facility DSFSF, fuel assemblies from the VVER-440 reactors of units 1 to 4 are stored in containers of type CONSTOR 440/84. The dry storage facility has a capacity of 72 containers. Each container can hold 84 fuel assemblies.

At the end of 2020 (data taken from the BNRA Annual report 2020 [121]), the status of the SNF storage facilities was:

- In the wet spent fuel storage facility, a total of 114 baskets containing 744 fuel assemblies from VVER-1000 reactors and 1436 fuel assemblies from VVER-440 reactors were stored under water.
- In the dry spent fuel storage facility, 17 CONSTOR 440/84 containers holding a total of 1428 assemblies from VVER-440 reactors were stored.

In 2020, 96 spent fuel assemblies from VVER-1000 reactors were transported to Russia for reprocessing.

At the end of 2022 (data taken from the BNRA Annual report 2022 [122]), the status of the SNF storage facilities was:

- In the wet spent fuel storage facility, a total of 112 baskets containing 804 fuel assemblies from VVER-1000 reactors and 1268 fuel assemblies from VVER-440 reactors were stored under water.

- In the dry spent fuel storage facility, 19 CONSTOR 440/84 containers holding a total of 1596 assemblies from VVER-440 reactors were stored.

In 2022, 144 spent fuel assemblies from the VVER-1000 reactors in units 5 and 6 were transported to be stored in the dry storage facility for spent fuel. No SNF was shipped for storage and reprocessing outside of the country.

5.3 Characteristics of SNF rods from Kozloduy Nuclear Power Plant

As a result of the study, a series of data on the fuel assemblies stored was compiled. The inventory was taken from the ARTEMIS Review in 2018 [123]. The total amount of spent nuclear fuel stored at the Kozloduy NPP site as of 31 December 2017 is given in Table 14.

Table 14 – Total amount of spent nuclear fuel stored at Kozloduy NPP as of 31 December 2017

Reactor type	Number of fuel assembles	Mass of heavy metal (kg)	Approximate activity (Bq)
VVER-440	2864	330910	$3.1 \cdot 10^{+18}$
VVER-1000	1371	553037	$2.1 \cdot 10^{+19}$
Total	4235	883947	$2.41 \cdot 10^{+19}$

The spent nuclear fuel in the spent fuel pools of the units 5 and 6 by number of assemblies and mass of heavy metal as of 12 December 2017 is given in Table 15.

Table 15 – Inventory of spent fuel pools of units 5 and 6 at Kozloduy NPP as of 12 December 2017

Reactor type	Initial enrichment in ^{235}U of fuel assemblies (%)	Spent fuel pool 5		Spent fuel pool 6		Total	
		Number of fuel assemblies	Mass of heavy metal (kg)	Number of fuel assemblies	Mass of heavy metal (kg)	Number of fuel assemblies	Mass of heavy metal (kg)
VVER-1000	3.53 to 4.4	338	138514	313	128710	651	267224

The results of the classification of the most important data for the characteristics of the SNF in the spent fuel pools are:

- The main quantity in the spent fuel pools are so-called TVSA assemblies, which were used in a four-year cycle and showed an initial enrichment of 3 to 4 % in ^{235}U.
- Each assembly has a steel frame and is a dismountable structure, with a top nozzle and a spring block, a central tube, guide tubes, and spacer grids. The assembly has a total length of 4570 mm. As fresh fuel, it contained about 430 kg of heavy metal spread over 312 fuel rods with UO_2 pellets with a central orifice.
- Small quantities of TVSA-12 assemblies used in a four-year cycle, TVS-M assemblies for a 3-year cycle, and TVS assemblies for a 2-year cycle with different characteristics are also stored.

The spent nuclear fuel in the wet storage facility SFSF by number of assemblies and mass of heavy metal as of 12 December 2017 is given in Table 16.

Table 16 – Inventory of wet SNF storage facility SFSF at Kozloduy NPP as of 12 December 2017

Reactor type	Initial enrichment in ^{235}U of fuel assemblies (%)	Number of fuel assembles	Mass of heavy metal (kg)
VVER-440	1.6 to 3.6	1856	214524
VVER-1000	2.0 to 4.4	720	285813
Total		2576	500337

The spent nuclear fuel in the dry storage facility DSFSF by number of assemblies and mass of heavy metal as of 31 December 2017 is given in Table 17.

Table 17 – Inventory of dry SNF storage facility DSFSF at Kozloduy NPP as of 31 December 2017

Reactor type	Initial enrichment in ^{235}U of fuel assemblies (%)	Number of fuel assembles	Mass of heavy metal (kg)
VVER-440	1.6 to 3.6	1008	116386

There are also studies on the thermo-mechanical-chemical conditions in the SNF storage facilities and discussions with experts and operational personal on possible thermo-mechanical loading and chemical interaction of fuel or cladding and potential influences on the integrity of the SNF rods. As result of the surveillance and control of the physicochemical and mechanical properties of claddings and fuel pellets, the most important influencing factors are known and necessary measures to ensure safety during predisposal activities are established. The above issues will continue to be researched and discussed with experts and operational personnel to clarify them to the greatest extent possible.

6. Summary and Conclusions

This report addresses the experimental characterisation, thermo-mechanical modelling and performance of unirradiated and irradiated samples of spent nuclear fuel rod segments and cladding. The experimental characterisation includes three-point bending tests, ring compression tests, and thermo-mechanical creep tests as well as examination methods such as neutron radiography, optical or scanning electron microscopy. Advances in modelling enable the description of the fuel rod behaviour in the aforementioned thermo-mechanical load scenarios and more generalised in spent fuel performance codes.

Hydrogen is relocated in nuclear fuel claddings by diffusion along temperature, stress, and concentration gradients, and towards a liner if existent (i.e., in case of duplex cladding). The precipitation of hydrides during cool-down at the beginning of the storage is influenced by mechanical stress. A strong accumulation of hydrides and a disadvantageous hydride alignment in relation to the stress state can affect the mechanical properties and compromise the fuel cladding integrity. Neutron radiography is an excellent tool to determine spatially resolved hydrogen and hydrides concentration distributions in claddings, specifically after thermo-mechanical testing. This helps to obtain a better information basis for modelling. It has become clear that a liner plays an important role as it attracts hydrogen, which will then no longer be available to form detrimental hydrides in the bulk part of the cladding.

Three-point bending and gravitational impact tests on filled pressurised SNF rod segments were conducted in hot-cell facilities. The material behaviour in the presence of hydrides and at different temperatures was systematically investigated in quasi-static laboratory tests on unirradiated rod segments with surrogate pellets until rupture. Load-deflection curves were generated and metallographic examinations in the direct vicinity of the failure location were carried out to investigate the hydride morphology, population and orientation. Without pellets, a significant deformation occurs under three-point bending. For samples with surrogate pellets, the load increases linearly with the displacement, whereby the slope is very steep. No load drops were observed under three-point bending in case of existing radial hydrides. In this case, the behaviour is completely dominated by the pellet. Post examination of the samples showed no cracks in the cladding. In the tests on irradiated samples with real pellets, the release of radioactive material in the event of a rupture could be determined; the fuel mass release per rupture corresponds to a fraction of a pellet.

No radial hydrides were present in the ring compression tests on irradiated samples because of the low hydrogen content due to missing fuel at the plenum of the rod or a pellet-cladding gap at low burnup, where the samples were taken. Without radial hydrides, there is generally a large deformation and then ductile failure of the sample. Nevertheless, sudden load decreases occurred on a sample with very high burnup of about 100 GWd/t_{HM}, which is attributed to extended radiation damages. Systematic ring compression tests were carried out on unirradiated samples at different temperatures and both with and without radial hydrides. With radial hydrides, brittle failure is possible even at low deformation and simultaneously low temperature. Crack initiation will occur on the radial hydride with the highest fracture mechanics load, which depends on the hydride size in the regions with the highest hoop stresses. When filled with surrogate pellets, the sample behaviour is dominated by the mechanical properties of the pellets, such that much higher forces have to be applied during the test.

Due to the high hydrogen content used in the creep tests conducted, precipitation hardening of the hydrides in the zirconium alloy significantly reduces the creep rate, as it strengthens the material and inhibits the dislocation sliding. The heat treatment under inert gas also had a significant effect, as it may have partially recrystallized the stress-relieved annealed cladding samples, which also has an effect on the creep rates.

Numerical simulation methods such as the finite element method are essential to study failure modes and derive mechanical properties of spent fuel rods. The development of a three-dimensional finite element model representing a spent fuel rod segment is a challenging task, since it includes large deformations with non-linear behaviour and undefined geometry of the cladding, pellets and their interaction. An approach is the numerical analysis of mechanical tests for parameter determination, for

instance the three-point bending test on surrogate samples. In such case, the geometrical characteristics and mechanical properties of the pellets and cladding are known, in comparison to the irradiated samples; therefore, the number of modelling uncertainties can be significantly reduced. It could be shown that cladding properties can be determined, using a numerical optimisation method based on a large number of automatically generated sensitivity calculations.

The brittle fracture of cladding samples with radial hydrides in the ring compression test (RCT) can be described with a cohesive zone model if the cohesive parameters are selected appropriately and the hydride morphology is specified. The parameters of the cohesive zone model (i.e., the cohesive strength and the separation energy for a given traction-separation law) may be used as a local two-parameter failure criterion for the safety evaluation of zirconium-based cladding alloys with radial hydrides under RCT loading conditions or fuel rod pinch-type loading, respectively. The cohesive parameters can be determined by inverse analysis of test results of samples that fail by fracture in the RCT. The hydride morphology to be used for this depends on the individual hydrogen content and the thermo-mechanical load history of the cladding tube to be analysed. The interpretation of the separation energy as an energy release rate provides a link to classical fracture mechanics.

Progress was made in the verification, validation and enhancement of spent fuel performance codes by i) the compilation of a representative validation database (related to rod internal pressure, fission gas release, rod void volume, in-clad hydrogen distribution), ii) the enhancement of CIEMAT's FRAPCON-xt for rod internal pressure prediction at high burnup greater than 60 GWd/t_{HM}, iii) the enhancement of HYDCLAD (CIEMAT's in-clad hydrogen performance subroutine) with more phenomenological modelling, iv) the extension of the BISON code with a cladding creep law for dry storage (CIEMAT's creep law), and v) the benchmark with FRAPCON-xt and BISON simulating in-reactor and dry storage scenarios.

Concerning further research, more tests on samples with pellets complementary to the tests without pellets are recommended to explore the pellet contribution to the structural behaviour of SNF rods. Further post-irradiation examination data are required to validate and extend various models in spent fuel performance codes. Experimental investigations should be accompanied by numerical modelling to better understand the processes in the test setups from a mechanical point of view. Furthermore, there is a need for comparative studies using model materials and irradiated fuel under the same conditions.

7. Acknowledgements

The present scientific-technical results support the Member States in implementing the Council Directive 2011/70/EURATOM on responsible and safe management of spent fuel and radioactive waste. It is directly coupled to the Article 12.1(f) stating the need to perform “the research, development and demonstration activities that are needed in order to implement solutions for the management of spent fuel and radioactive waste”.

The support by the Gösgen nuclear power plant (KKG) and Framatome GmbH (former AREVA GmbH) in providing and authorising the use of SNF rods for the mechanical tests is greatly appreciated.

The research in this report made use of the following Idaho National Laboratory (INL) software: Multidimensional Fuel Performance Code (BISON). This software is licensed by Battelle Energy Alliance, LLC (BEA), Managing & Operating Contractor of INL. A software license may be available by contacting INL at agradmin@inl.gov. This software is experimental in nature. BEA and the U.S. Government make no representations; extend no warranties; and disclaim any liability for the use of this software or software outputs in this publication. Use of this software is not an endorsement by BEA or the U.S. Government.

References

[1] ASTM C1562-10(2018), Standard guide for evaluation of materials used in extended service of interim spent nuclear fuel dry storage systems, ASTM International, West Conshohocken, PA, USA, 2018.

[2] Motta, A. T., Couet, A., Comstock, R. J.: Corrosion of zirconium alloys used for nuclear fuel cladding, Annu. Rev. Mater. Res. 45 (2015) 311-343.

[3] Motta, A. T. et al.: Hydrogen in zirconium alloys: A review, J. Nucl. Mater. 518 (2019) 440-460.

[4] Couet, A., Motta, A. T., Comstock, R. J.: Hydrogen pickup measurements in zirconium alloys: Relation to oxidation kinetics, J. Nucl. Mater. 451 (2014) 1-13.

[5] McMinn, A., Darby, E. C., Schofield, J. S.: The terminal solid solubility of hydrogen in zirconium alloys, Zirconium in the Nuclear Industry: 12th International Symposium, Toronto, ASTM STP 1354, ASTM International, West Conshohocken, PA, USA, 2000, pp. 173-195.

[6] Ells, C. E.: Hydride precipitates in zirconium alloys, J. Nucl. Mater. 28 (1968) 129-151.

[7] Puls, M. P.: The effect of hydrogen and hydrides on the integrity of zirconium alloy components: Delayed hydride cracking, Springer, London, 2012.

[8] Blat, M., Legras, L., Noel, D., Amanrich, H.: Contribution to a better understanding of the detrimental role of hydrogen on the corrosion rate of Zircaloy-4 cladding materials, Zirconium in the Nuclear Industry: 12th International Symposium, Toronto, ASTM STP 1354, ASTM International, West Conshohocken, PA, USA, 2000, pp. 563-591.

[9] Pierron, O. N., Koss, D. A., Motta, A. T., Chan, K. S.: The influence of hydride blisters on the fracture of Zircaloy-4, J. Nucl. Mater. 322 (2003) 21-35.

[10] Hellouin de Menibus, A. et al.: Formation and characterization of hydride blisters in Zircaloy-4 cladding tubes, J. Nucl. Mater. 449 (2014) 132-147.

[11] Daum, R. S., Chu, Y. S., Motta, A. T.: Identification and quantification of hydride phases in Zircaloy-4 cladding using synchrotron radiation diffraction, J. Nucl. Mater. 392 (2009) 453-463.

[12] Kawanishi, H., Ishino, S., Mishima, Y.: Directionality of the grain boundary hydride in Zircaloy-2, Zirconium in Nuclear Applications, ASTM STP 551, ASTM International, West Conshohocken, PA, USA, 1974, pp. 201-211.

[13] United States Nuclear Regulatory Commission: Cladding considerations for the transportation and storage of spent fuel, Interim Staff Guidance No. 11, Revision 3, 2003.

[14] Louthan, M. R., Marshall, R. P.: Control of hydride orientation in Zircaloy, J. Nucl. Mater. 9 (1963) 170-184.

[15] Marshall, R. P., Louthan, M. R.: Tensile properties of Zircaloy with oriented hydrides, Trans. ASM 56 (1963) 693-700.

[16] Colas, K. B., Motta, A. T., Almer, J. D., Daymond, M. R., Kerr, M., Banchik, A. D., Vizcaino, P., Santisteban, J. R.: In situ study of hydride precipitation kinetics and re-orientation in Zircaloy using synchrotron radiation, Acta Mater. 58 (2010) 6575-6583.

[17] Billone, M. C., Burtseva, T. A., Einziger, R. E.: Ductile-to-brittle transition temperature for high-burnup cladding alloys exposed to simulated drying-storage conditions, J. Nucl. Mater. 433 (2013) 431-448.

[18] Kim, J.-S., Kim, T.-H., Kook, D.-H., Kim, Y.-S.: Effects of hydride morphology on the embrittlement of Zircaloy-4 cladding, J. Nucl. Mater. 456 (2015) 235-245.

[19] Billone, M. C., Burtseva, T. A., Dobrzynski, J. P., McGann, D. P., Byrne, K., Han, Z., Liu, Y. Y.: Used fuel disposition campaign phase I ring compression testing of high-burnup cladding, Report FCRD-USED-2012-000039, ANL-13/05, Argonne National Laboratory, Lemont, IL, USA, 2011.

[20] Billone, M. C., Burtseva, T. A., Han, Z., Liu, Y. Y.: Embrittlement and DBTT of high-burnup PWR fuel cladding alloys, Report FCRD-UFD-2013-000401, ANL-13/16, Argonne National Laboratory, Lemont, IL, USA, 2013.

[21] Billone, M. C., Burtseva, T. A., Han, Z., Liu, Y. Y.: Effects of multiple drying cycles on high-burnup PWR cladding alloys, Report FCRD-UFD-2014-000052, ANL-14/11, Argonne National Laboratory, Lemont, IL, USA, 2014.

[22] Desquines, J., Drouan, D., Billone, M., Puls, M. P., March, P., Fourgeaud, S. et al.: Influence of temperature and hydrogen content on stress-induced radial hydride precipitation in Zircaloy-4 cladding, J. Nucl. Mater. 453 (2014) 131-150.

[23] Cinbiz, M. N., Motta, A. T., Koss, D., Billone, M.: Hydride reorientation in Zircaloy-4 under different states of stress as studied with in situ X-ray diffraction, Zirconium in the Nuclear Industry: 18th International Symposium, ASTM STP 1597, ASTM International, West Conshohocken, PA, USA, 2018, pp. 1252-1285.

[24] Lacroix, E., Motta, A. T., Almer, J. D.: Experimental determination of zirconium hydride precipitation and dissolution in zirconium alloy, J. Nucl. Mater. 509 (2018) 162-167.

[25] Hong, J.-D., Park, M., Alvarez Holston, A.-M., Stjärnsäter, J., Kook, D.: Threshold stress intensity factor of delayed hydride cracking in irradiated and unirradiated Zircaloy-4 cladding, J. Nucl. Mater. 543 (2021) 152596.

[26] Le Saux, M., Besson, J., Carassou, S.: A model to describe the mechanical behavior and the ductile failure of hydrided Zircaloy-4 fuel claddings between 25 °C and 480 °C, J. Nucl. Mater. 466 (2015) 43-55.

[27] Daum, R. S, Majumdar, S., Tsai, H. C., Billone, M. C., Bates, D. W., Koss, D. A. et al.: Embrittlement of hydrided Zircaloy-4 under RIA-like conditions, Zirconium in the Nuclear Industry: 13th International Symposium, ASTM STP 1423, ASTM International, West Conshohocken, PA, USA, 2001, pp. 702-719.

[28] Raynaud, P. A., Koss, D. A., Motta, A. T.: Crack growth in the through-thickness direction of hydrided thin-wall Zircaloy sheet, J. Nucl. Mater. 420 (2011) 69-82.

[29] Ziaei, S., Wu, Q., Zikry, M. A.: Orientation relationships between coherent interfaces in hcp-fcc systems subjected to high strain-rate deformation and fracture modes, J. Mater. Res. 30 (2015) 2348-2359.

[30] Einziger, R. E. et al.: Data needs for long-term dry storage of LWR fuel, EPRI Report TR-108757, Electric Power Research Institute, Palo Alto, CA, USA, 1998.

[31] Goll, W., Spilker, H., Toscano, E.: Short-time creep and rupture tests on high burnup fuel rod cladding, J. Nucl. Mater. 289 (2001) 247-253.

[32] Weck, P. F., Kim, E., Tikare, V., Mitchell, J. A.: Mechanical properties of zirconium alloys and zirconium hydrides predicted from density functional perturbation theory, Dalton Trans. 44 (2015) 18769.

[33] Rondinella, V. V., Nasyrow, R., Papaioannou, D., Vlassopoulos, E., Cappia, F., Dieste-Blanco, O., Wiss, T.: Mechanical integrity studies on spent nuclear fuel rods, Proc. 16th International High-Level Radioactive Waste Management Conference (IHLRWM 2017), Charlotte, NC, USA, 9-13 April 2017.

[34] Vlassopoulos, E., Caruso, S., Nasyrow, R., Papaioannou, D., Gretter, R., Rondinella, V. V.: Investigation of the properties and behaviour of spent nuclear fuel under conditions relevant for

interim dry storage, handling and transportation: Experimental setup optimisation and cold test campaign, Nagra Working Rep. NAB 16-067, Wettingen, Switzerland, 2017.

[35] Vlassopoulos, E., Nasyrow, R., Papaioannou, D., Rondinella, V. V., Caruso, S., Pautz, A.: Destructive tests for determining mechanical integrity of spent nuclear fuel rods, Proc. 16th International High-Level Radioactive Waste Management Conference (IHLRWM 2017, 9-13 April 2017, Charlotte, NC, USA), Paper 19902 (2017), pp. 726-733.

[36] Vlassopoulos, E., Nasyrow, R., Papaioannou, D., Gretter, R., Fongaro, L., Somers, J., Rondinella, V. V., Caruso, S., Grünberg, P., Helfenstein, J., Schwizer, P., Pautz, A.: Response of irradiated nuclear fuel rods to quasi-static and dynamic loads, Kerntechnik 83 (2018) 507-512.

[37] Vlassopoulos, E.: Structural performance and mechanical properties investigation of spent nuclear fuel rods under static and dynamic bending loads, Swiss Federal Institute of Technology in Lausanne, Ecole Polytechnique Fédérale de Lausanne (EPFL), PhD Thesis no. 7619, 2021.

[38] ISO 7438:2016, Metallic materials – Bend test.

[39] Papaioannou, D., Nasyrow, R., Rondinella, V. V., Goll, W., Winkler, H.-P., Liedtke, R., Hoffmann, D.: Proc. KTG Conference 2009, Dresden, Germany.

[40] Papaioannou, D., Vlassopoulos, E., Nasyrow, R., Gretter, R., Fongaro, L., Somers, J., Rondinella, V., Caruso, S.: Mechanical loading lests on irradiated LWR fuel rods, Proc. IAEA International Conference on the Management of Spent Fuel, Paper IAEA CN-272/51, Vienna, Austria, 2019.

[41] Vlassopoulos, E., Papaioannou, D., Nasyrow, R., Rondinella, V., Caruso, S., Schweizer, E.: Experimental study on the mechanical stability of a 59 GWd/t_{HM} nuclear fuel rod", Proc. TopFuel 2021, Santander, Spain, 24-28 October 2021.

[42] Arborelius, J., Dahlbach, M., Hallstadius, L., Jourdaian, P., Andersson, T., Lisdat, R., Hahn, M., Toscano, E. H.: The effect of duplex cladding outer component tin content on corrosion, hydrogen pick-up, and hydride distribution at very high burnup, Zirconium in the Nuclear Industry: 14th International Symposium, ASTM STP 1467, ASTM International, West Conshohocken, PA, USA, 2005, pp. 526-546.

[43] IAEA Hungarian National Report, Seventh Report prepared within the Framework of the Joint Convention on the Safety of Spent Fuel Management and on the Safety of Radioactive Waste Management, Vienna, 2020.

[44] Király, M., Hózer, Z., Horváth, M., Novotny, T., Perez-Feró, E., Vér, N.: Impact of thermal and chemical treatment on the mechanical properties of E110 and E110G cladding tubes, Nuclear Engineering and Technology 51 (2019) 518-525.

[45] Nikulina, A. V., Markelov, V. A., Peregud, M. M., Bibilashvili, Y. K., Kotrekhov, V. A., Lositsky, A. F., Kuzmenko, N. V., Shevnin, Y. P., Shamardin, V. K., Kobylyansky, G. P., Novoselov, A. E.: Zirconium alloy E635 as a material for fuel rod cladding and other components of VVER and RBMK cores, Zirconium in the Nuclear Industry: 11th International Symposium, Garmisch-Partenkirchen, ASTM STP 1295, ASTM International, West Conshohocken, PA, USA, 1996, pp. 785-804.

[46] Suman, S., Khan, M. K., Pathak, M., Singh, R. N.: Effects of hydrogen on thermal creep behaviour of Zircaloy fuel cladding, J. Nucl. Mater. 498 (2018) 20-32.

[47] PSI Applied Materials Group, Neutron Imaging and Engineering Diffraction; Retrieved on 31 May 2024: https://www.psi.ch/en/niag/comparison-to-x-ray

[48] Trtik, P., Zubler, R., Gong, W., Grabherr, R., Bertsch, J., Duarte, L. I.: Sample container for high-resolution neutron imaging of spent nuclear fuel cladding sections, Rev. Sci. Instrum. 91 (2020) 056103.

[49] Valance, S., Zemek, M., Bertsch, J., Hellwig, Ch.: Hydrogen relocation kinetics within Zircaloy cladding tubes, Proc. TopFuel 2015, Paper A0168, Zurich, Switzerland, 13-17 September 2015.

[50] Gong, W., Trtik, P., Bertsch, J.: Hydrogen redistribution in Zircaloy measured with high resolution neutron imaging, Proc. Water Reactor Fuel Performance Meeting (WRFPM 2017), Jeju, Korea, 10-14 September 2017.

[51] Duarte, L. I., Fagnoni, F., Zubler, R., Gong, W., Trtik, P., Bertsch, J.: Effect of the inner liner on the hydrogen distribution of Zircaloy-2 nuclear fuel claddings, J. Nucl. Mater. 557 (2021) 153284.

[52] Valance, S., Bertsch, J., Alam, A. M.: Statistical Analysis of hydrides reorientation properties in irradiated Zircaloy-2, Journal of ASTM International 8 (2011) 1-14.

[53] Duarte, L. I., Fagnoni, F., Zubler, R., Gong, W., Trtik, P., Bertsch, J.: Hydrides characterization in Zircaloy-2 liner cladding after C-shaped ring compression tests, Proc. TopFuel 2019, Paper 29934, Seattle, WA, USA, 22-26 September 2019.

[54] Gong, W., Trtik, P., Valance, S., Bertsch, J.: Hydrogen diffusion under stress in Zircaloy: High-resolution neutron radiography and finite element modeling, J. Nucl. Mater. 508 (2018) 459-464.

[55] Gong, W., Trtik, P., Zubler, R., Bertsch, J.: Hydrides reorientation and redistribution under non-uniform stress, Proc. TopFuel 2019, Paper 30064, Seattle, WA, USA, 22-26 September 2019.

[56] Gong, W., Trtik, P., Ma, F., Jia, Y., Li, J., Bertsch, J.: Hydrogen diffusion and precipitation under non-uniform stress in duplex zirconium nuclear fuel cladding investigated by high-resolution neutron imaging, J. Nucl. Mater. 570 (2022) 153971.

[57] Yetik, O., Duarte, L. I., Trtik, P., Makowska, M. G., Schneider, C., Sanchez, D., Zubler, R., Grabherr, R., Pouchon, M. A., Bertsch, J.: Impact of irradiation damage and thermomechanical treatments on the hydride diffusion to the substrate liner interface in zirconium-based nuclear fuel claddings, Proc. MiNES 2023, New Orleans, LA, USA, 10-14 December 2023.

[58] Colldeweih, A. W.: Delayed hydride cracking in irradiated and unirradiated Zircaloy-2 cladding, Doctoral thesis, Ecole Polytechnique Fédérale de Lausanne (EPFL), PhD Thesis no. 9881, 2022.

[59] Colldeweih, A. W., Fagnoni, F., Trtik, P., Zubler, R., Pouchon, M. A., Bertsch, J.: Delayed hydride cracking in Zircaloy-2 with and without liner at various temperatures investigated by high-resolution neutron radiography, J. Nucl. Mater. 561 (2022) 153549.

[60] Schneider, C., Yetik, O., Duarte, L., Trtik, P., Grabherr, R., Bertsch, J.: Neutron imaging of irradiated fuel rod: contribution of the inner oxide to the contrast, Proc. NuMat22, Ghent, Belgium, 24-28 October 2022.

[61] Sanchez, D., Ring compression creep testing for Zircaloy claddings, Ecole Polytechnique Fédérale de Lausanne (EPFL), Master Thesis (MSc. Nuclear Engineering), 2023.

[62] Han, Z., Billone, M. C., Liu, Y. Y.: Finite element analysis of ring compression testing for used nuclear fuel cladding, Proc. ASME 2022 Pressure Vessels and Piping Conference (PVP2022), Paper PVP2022-83911, Las Vegas, NV, USA, 17-22 July 2022.

[63] Nilsson, K.-F., Jaksic, N., Vokal, V.: An elasto-plastic fracture mechanics based model for assessment of hydride embrittlement in zircaloy cladding tubes, J. Nucl. Mater. 396 (2010) 71-85.

[64] Kuna, M.: Finite Elements in Fracture Mechanics, Springer Netherlands, Dordrecht, 2013.

[65] Rousselier, G.: Ductile fracture models and their potential in local approach of fracture, Nucl. Eng. Des. 105 (1987) 97-111.

[66] Gurson, A.: Continuum theory of ductile rupture by void nucleation and growth: Part I – Yield criteria and flow rules for porous ductile media, J. Eng. Mater. Technol. 99 (1977) 2-15.

[67] Tvergaard, V., Needleman, A.: Analysis of cup-cone fracture in a round tensile bar, Acta Metall. 32 (1984) 157-169.

[68] Tvergaard, V.: Material failure by void growth to coalescence, Adv. Appl. Mech. 27 (1990) 83-151.

[69] Cockeram, B., Chan, K.: In situ studies and modeling of the deformation and fracture mechanism for wrought Zircaloy-4 and Zircaloy-2 as a function of stress-state, J. Nucl. Mater. 434 (2013) 97-123.

[70] Rice, J., Tracey, D.: On the ductile enlargement of voids in triaxial stress, J. Mech. Phys. Solids 17 (1969) 201-217.

[71] Chen, Q., Ostien, J., Hansen, G.: Development of a used fuel cladding damage model incorporating circumferential and radial hydride responses, J. Nucl. Mater. 447 (2014) 292-303.

[72] Williams, B., St Lawrence, S., Leitch, B.: Comparison of the measured and predicted crack propagation behaviour of Zr-2.5Nb pressure tube material, Eng. Fract. Mech. 78 (2011) 3135-3152.

[73] Brocks, W., Cornec, A.: Cohesive models – Special issue, Engineering Fracture Mechanics 70 (2003) 1741-1987.

[74] Brocks, W., Cornec, A., Scheider, I.: Computational aspects of nonlinear fracture mechanics. In: Milne, I., Ritchie, R. O., Karihaloo, B. (Eds.): Comprehensive Structural Integrity – Numerical and Computational Methods, Vol. 3, pp. 127-209, Elsevier, Oxford, UK, 2003.

[75] Chan, K. S.: A fracture model for hydride-induced embrittlement, Acta Metall. Mater. 43 (1995) 4325-4335.

[76] Qin, W., Szpunar, J. A., Kozinski, J.: Hydride-induced degradation of zirconium alloys: A criterion for complete ductile-to-brittle transition and its dependence on microstructure, Proc. R. Soc. A Math. Phys. Eng. Sci. 471 (2015) 20150192.

[77] Martin-Rengel, M. A., Gómez Sánchez, F. J., Ruiz-Hervías, J., Caballero, L.: Determination of the hoop fracture properties of unirradiated hydrogen-charged nuclear fuel cladding from ring compression tests, J. Nucl. Mater. 436 (2013) 123-129.

[78] Billone, M. C., Burtseva, T. A., Liu, Y. Y.: Baseline studies for ring compression testing of high-burnup fuel cladding, Report FCRD-USED-2013-000040, ANL 12/58, Argonne National Laboratory, Lemont, IL, USA, 2012.

[79] Gómez-Sánchez, F. J., Martin-Rengel, M. A., Ruiz-Hervías, J., Puerta, M. A.: Study of the hoop fracture behaviour of nuclear fuel cladding from ring compression tests by means of non-linear optimization techniques, J. Nucl. Mater. 489 (2017) 150-157.

[80] Simbruner, K., Billone, M. C., Zencker, U., Liu, Y. Y., Völzke, H.: Brittle failure analysis of high-burnup PWR fuel cladding alloys, Trans. 26th International Conference on Structural Mechanics in Reactor Technology (SMiRT), Paper Tu.4.I.1, Berlin, Germany, 10-15 July 2022.

[81] Zencker, U., Gaddampally, M. R., Völzke, H.: Failure analysis on irradiated claddings subjected to long-term dry interim storage, Trans. 27th International Conference on Structural Mechanics in Reactor Technology (SMiRT), Paper We.2.H.1, Yokohama, Japan, 3-8 March 2024.

[82] Arsene, S., Bai, J.: A new approach to measuring transverse properties of structural tubing by a ring test, Journal of Testing and Evaluation 24 (1996) 386-391.

[83] Gómez-Sánchez, F. J., Martin-Rengel, M. A., Ruiz-Hervías, J.: A new procedure to calculate the constitutive equation of nuclear fuel cladding from ring compression tests, Progress in Nuclear Energy 97 (2017) 245-251.

[84] Ruiz-Hervías, J, Simbruner, K., Cristobal-Beneyto, M., Perez-Gallego, D., Zencker, U.: Failure mechanisms in unirradiated ZIRLO® cladding with radial hydrides, J. Nucl. Mater. 544 (2021) 152668.

[85] Machiels, A. J., Rashid, J. Y. R.: Spent fuel transportation applications − Assessment of cladding performance under normal and hypothetical accident conditions, Report 1015048, Electric Power Research Institute (EPRI), 2007.

[86] U.S. NRC: Dry storage and transportation of high burnup fuel, Report NUREG-2224, Washington, DC, USA, 2020.

[87] Garcia, M., Beattie, T., Schumacher, S.: EURAD − the European Joint Programme for research on radioactive waste management between EU members states national programmes, EPJ Nucl. Sci. Technol. 6 (2020) 21.

[88] Arkoma, A., Huhtanen, R., Leppänen, J., Peltola, J., Pättikangas, T.: Calculation chain for the analysis of spent nuclear fuel in long-term interim dry storage, Ann. Nucl. Energy 119 (2018) 129-138.

[89] Rossiter, G.: Development of the ENIGMA fuel performance code for whole core analysis and dry storage assessments, Nucl. Eng. Technol. 43 (2011) 489-498.

[90] Williamson R. L., Hales, J. D., Novascone, S. R., Tonks, S. R., Gaston, D. R., Permann, C. J., Andrs, D., Martineau, R.C.: Multidimensional multiphysics simulation of nuclear fuel behaviour, J. Nucl. Mater. 423 (2012) 149-163.

[91] Feria, F., Aguado, C., Herranz, L. E.: Extension of FRAPCON-xt to hydride radial reorientation in dry storage, Ann. Nucl. Energy 145 (2020) 107559.

[92] Raynaud, P. A. C., Einziger, R. E.: Cladding stress during extended storage of high burnup spent nuclear fuel, J. Nucl. Mater. 464 (2015) 304-312.

[93] Herranz, L. E., Feria, F.: Extension of the FRAPCON-3.3 creep model to dry storage conditions, Prog. Nucl. Energy 52 (2010) 634-639.

[94] Feria, F., Herranz, L. E.: Effect of the oxidation front penetration on in-clad hydrogen migration, J. Nucl. Mater. 500 (2018) 349-360.

[95] Smith Jr., G. P., Pirek, R. C., Griffiths, M.: Hot cell examination of extended burnup fuel from Calvert Cliffs-1 (Vol. 2), Report TR-103302-V2, Electric Power Research Institute (EPRI), 1994.

[96] Smith Jr., G. P., Ruzauskas, E. J., Pirek, R. C., Griffiths, M.: Hot cell examination of extended burnup fuel from Calvert Cliffs-1 (Vol. 1), Report TR-103302-V1, Electric Power Research Institute (EPRI), 1993.

[97] Lyon, W. F.: IFPE/US-PWR 16x16 LTA Extended burnup demonstration program, Summary File, Rev. 1, 2005.

[98] Geelhood, K. J., Luscher, W. G.: FRAPCON-4.0 Integral assessment, Vol. 2, Pacific Northwest National Laboratory (PNNL), Richland, WA, USA, 2015.

[99] Geelhood, K. J., Goodson, C.: Sibling rod thermomechanical modeling with FAST and comparison to post-irradiation examination data, Proc. TopFuel 2019, Seattle, WA, USA, 22-26 September 2019.

[100] INL: BISON - A finite element-based nuclear fuel performance code; Retrieved on 30 June 2022: https://mooseframework.inl.gov/bison

[101] Sahle, W.: PIE of CIP0-1 father rod: Cladding oxide and hydride measurement in SEM, Report N(H)-02/027, Studsvik, Nyköping, Sweden, 2002.

[102] Newman, C., Hansen, G., Gaston, D.: Three dimensional coupled simulation of thermo-mechanics, heat, and oxygen diffusion in UO_2 nuclear fuel rods, J. Nucl. Mater. 392 (2009) 6-15.

[103] Gaston, D., Newman, C., Hansen, G., Lebrun-Grandié, D.: MOOSE: A parallel computational framework for coupled systems of nonlinear equations, Nucl. Eng. Des. 239 (2009) 1768-1778.

[104] INL: Complete BISON input syntax and reference manual; Retrieved on 02 August 2023: https://mooseframework.inl.gov/bison/syntax/index.html

[105] Feria, F., Herranz, L.E., Penalva, J.: On the way to enabling FRAPCON-3 to model spent fuel under dry storage conditions: the thermal evolution, Ann. Nucl. Energy 85 (2015) 995-1002.

[106] Arkoma, A.: Fuel dry storage modelling with INL's BISON code in EU EURAD project, VTT Research Report VTT-R-00633-23, Espoo, 2023.

[107] U.S. NRC: Standard Review Plan for Spent Fuel Dry Storage Systems and Facilities, Report NUREG-2215, Washington, DC, USA, 2020.

[108] Kim, H.-G., Jeong, Y.-H., Kim, K.-T.: The effects of creep and hydride on spent fuel integrity during interim dry storage. Nucl. Eng. Technol. 42 (2010) 249-258.

[109] NEA: Reactivity initiated accident benchmark Phase III, Report NEA/CSNI/R(2020)10, OECD, 2022.

[110] Passelaigue, F., Simon, P.-C., Motta, A.: Predicting the hydride rim by improving the solubility limits in the Hydride Nucleation-Growth-Dissolution (HNGD) model, Journal of Nuclear Materials 558 (2022) 153363.

[111] Lacroix, E., Motta, A.: Validation of BISON calculation of hydrogen distribution by comparison to experiment, TMS 2016, 145th Annual Meeting & Exhibition; Retrieved on 02 August 2023: https://www.nuce.psu.edu/motta/Publications/132_Lacroix_TMS_2016.pdf

[112] Act on the safe use of nuclear energy (ASUNE), promulgated in State Gazette (SG) no. 63/28.06.2002, supplemented in SG no.86/13.10.2023.

[113] Regulations on safe management of radioactive waste, adopted with CM Decree no. 185/23.08.2013, promulgated in State Gazette (SG) no. 76/30.08.2013, amended in SG no. 4/09.01.2018, 37/04.05.2018 (in Bulgarian).

[114] Strategy for the management of spent fuel and radioactive waste until 2030, ME, Sofia 2015 (in Bulgarian).

[115] Regulations on ensuring the safety in spent fuel management, adopted with CM Decree no. 196/02.08.2004, promulgated in State Gazette (SG) no. 71/13.08.2004, amended in SG no. 76/30.08.2013, 4/09.01.2018, 37/4.05.2018 (in Bulgarian).

[116] Regulations on the conditions and procedure for transport of radioactive material, adopted with CM Decree no. 156/13.07.2005, promulgated in State Gazette (SG) No. 60/22.07.2005, amended in SG No. 13/14.02.2014.

[117] BNRA: Updated national action plan – EU Stress tests at the Kozloduy nuclear power plant, Bulgarian Nuclear Regulatory Agency, Sofia, 2018 (in Bulgarian).

[118] BNRA: Updated national action plan – EU Stress tests at the Kozloduy nuclear power plant, Bulgarian Nuclear Regulatory Agency, Sofia, 2021 (in Bulgarian).

[119] BNRA: Final Report on the Implementation of the Updated National Action Plan of Republic of Bulgaria, Bulgarian Nuclear Regulatory Agency, Sofia, October 2023.

[120] BNRA: Sixth national report on fulfilment of the obligations of the joint convention on the safety of spent fuel management and on safety of radioactive waste management, Bulgarian Nuclear Regulatory Agency, Sofia, September 2017.

[121] BNRA: Annual report, Bulgarian Nuclear Regulatory Agency, Sofia, 2020.

[122] BNRA: Annual report, Bulgarian Nuclear Regulatory Agency, Sofia, 2022.

[123] Self-Assessment on the safety of spent fuel management and on the safety of radioactive waste management, Reference material for the ARTEMIS reviews, Sofia, 2018.